2-P

NASA CR-130184

OSO-7

ORBITING SOLAR OBSERVATORY

ONE-YEAR ORBIT PERFORMANCE EVALUATION

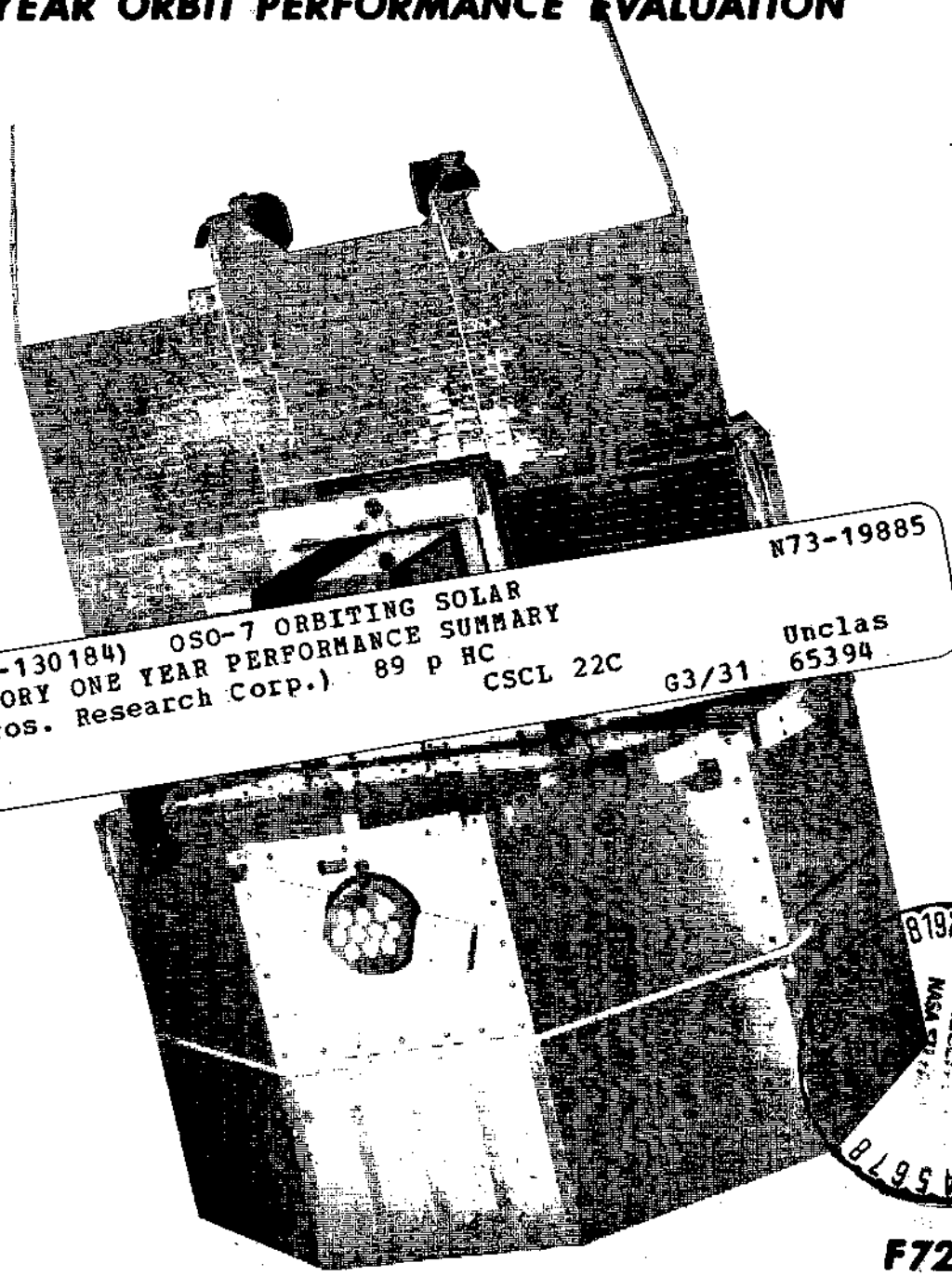

F72-10

BALL BROTHERS RESEARCH CORPORATION

SUBSIDIARY OF BALL CORPORATION

BOULDER, COLORADO

89

OSO-7

ORBITING SOLAR OBSERVATORY
ONE-YEAR PERFORMANCE SUMMARY

F72-10

December 31, 1972

Prepared By

OSO Program Staff

BALL BROTHERS RESEARCH CORPORATION
SUBSIDIARY OF BALL CORPORATION
BOULDER, COLORADO

PREFACE

During the 1950's rapid progress was made in solar physics and in instrument and space hardware technology, using rocket and balloon flights that, although of brief duration, provided a view of the sun free from the obscuring atmosphere. The significance of data from these flights confirmed the often-asserted value of long-term observations from a spacecraft in advancing our knowledge of the sun's behavior.

Thus, the first of NASA's space platforms designed for long-term observations of the universe from above the atmosphere was planned, and the Orbiting Solar Observatory program started in 1959. Solar physics data return began with the launch of OSO-1 in March of 1962. OSO-2 and OSO-3 were launched in 1965, OSO-4 and OSO-5 in 1967, OSO-6 in 1969, and the most recent, OSO-7, was launched on September 29, 1971.

All seven OSO's have been highly successful both in scientific data return and in performance of the engineering systems. The gain to date in scientific knowledge amply justifies the foresight of the early planners.

This report describes the performance of the OSO-7 spacecraft during the first 12 months after launch. A summary description of the spacecraft and experiments is also given. Additional descriptive detail may be found in the Final Program Report for the OSO-7, F72-01, December 31, 1972.

CONTENTS

ILLUSTRATIONS

ILLUSTRATIONS (Cont.)

TABLES

Section 1
INTRODUCTION

The seventh in the continuing series of orbiting solar observatories was launched September 29, 1971. OSO-7 has performed well to date and has yielded data of notably high scientific value.

The objectives of the OSO program are generally to make observations and measurements of the sun and celestial sphere that cannot be made from earth's surface and that will contribute to:

- Determination of the sun's atmospheric structure, composition and physical state and the process of energy transport radially outward and inward.
- Determination of origin, energy supply and solar/terrestrial consequences of transient solar phenomena such as sun spots, flares, radio bursts, and particle bursts.
- Prediction of transient solar events and their consequences, by combining OSO data with those from other spacecraft, rockets, balloons, and ground observatories.
- Secondary objectives, including study of the earth and celestial objects.

The OSO-7 instruments monitor X-rays, gamma rays, ultraviolet radiation, outer corona-white light, and other emanations from the sun along with X-rays and high energy charged particles from the entire celestial sphere. The specific mission objectives for OSO-7 are to:

- Obtain extreme ultraviolet spectroheliograms between 170 Å and 400 Å and spectroheliograms in the 1.7 Å to 2.5 Å and 8 Å to 15 Å regions; and to determine the polarization of flare X-rays from 20 to 40 keV.
- Study, sequentially, the solar disc and inner corona in the extreme ultraviolet (170 Å to 550 Å), and the outer corona in white light (3900 Å to 6500 Å).
- Survey the entire celestial sphere for sources of cosmic X-rays in the energy range from 1 to 60 keV with an angular resolution of about 0.1° and to perform spectral analysis in five broad energy bands.
- Perform a celestial sphere scan to determine the intensity, position, and spectrum of cosmic X-ray sources in the 10 to 550 keV range, with an angular resolution of 0.2°.

- Study solar X-ray bursts in the energy range of about 1.4 to 300 keV.
- Monitor intensity and line structure of solar gamma ray flux in the energy range of 0.3 to 9.1 MeV.

This report is an evaluation of the first year of in-orbit performance of the OSO-7 engineering systems. The performance of the scientific instruments has been excellent, and all experiment expectations have been more than realized. However, the instrument performance evaluation and scientific results are left to the science teams; this report is limited to the spacecraft engineering systems and their support of the scientific instruments so that the mission objectives could be met.

Section 2

BRIEF SUMMARY OF OBSERVATORY PERFORMANCE THROUGH ONE YEAR IN ORBIT

When OSO-7 arrived at Cape Kennedy in September 1972 it was the most thoroughly analyzed and tested and most capable observatory in the continuing Orbiting Solar Observatory Program. Its subsystem and instrument payload capability was increased by a factor of three over previous observatories, with nearly similar increases in solar array power available and control system gas storage. This extensive redesign, along with numerous new and/or improved subsystems required a complete qualification program on a separate qualification model spacecraft; complete structural, thermal, and dynamics analyses; and comprehensive acceptance testing at the component and flight observatory levels. The first OSO to be launched in the "new-generation" of the program, OSO-7 had fulfilled all GSFC S-320-G-1 Environmental Test Requirements, and it was launched with a great deal of confidence.

Final prelaunch observatory preparation proceeded smoothly and the launch sequence on September 29, 1971 was flawless until a booster malfunction occurred during orbit injection. The following paragraphs briefly summarize the problem, the recovery of the observatory, and the subsequent performance of OSO-7 throughout the first year in orbit.

During the orbit-stabilizing second-stage restart burn, the booster lost pitch steering control. The resulting final orbit was adequate, but the spacecraft was required to recover from the severe tumbling motion imparted by the booster. After stabilizing, the observatory spin axis was nearly along the sun line, rather than perpendicular to the sun line as planned.

Fortunately, this possibility had been considered in the design which allowed for acquisition from any attitude. In addition, a comprehensive contingency plan had been prepared and practice dynamic simulation runs had been made to prepare for possible launch anomalies. After eight hours of data analysis and command control reactions, the observatory spin axis was precessed toward the proper solar orientation so the automatic control systems could take over. The observatory batteries were nearly discharged during this recovery operation, and it was feared that they would not last long enough for recovery. Also, due to the unusual orientation of the sun on the observatory, some subsystems temporarily got colder than anticipated (e.g., gyro) and others got warmer than anticipated (e.g., antenna). However, after recovery all spacecraft systems were operating normally except one tape recorder. It is probable that the loop of tape passing over the recording head (the only part of the tape not contained in the reel) was thrown from its guides.

After the observatory was operating properly in its automatic control mode, the experiment turn-on sequence was initiated. Experiment operations were verified with all performing as anticipated. The only effects of the launch anomaly were the loss of one tape recorder and the depletion of control gas used in orienting the observatory. About one-third of the pitch control gas was used, as well as one-half of the spin control gas. The spacecraft has magnetic torquing coils for pitch, roll, and indirectly spin control as well as a conservatively sized gas storage supply so no serious reduction in orbit lifetime is anticipated. The 319 by 571 Km final orbit inclined 33.1 degrees to the equator is predicted to last through 1974.

Experiment data acquisition, begun according to turn-on plan, showed immediate scientific results, practically from the first operational orbit. The data acquisition program has continued with good results to date. Scientific data returned has given new and important insight into flare development detail, coronal temperature variations, and streamer dynamics of plasma flow. The observatory is expected to have sufficient lifetime to permit comparisons of data from the Skylab A mission during 1973.

Section 3
OBSERVATORY DESCRIPTION

3.1 SPACECRAFT STRUCTURE AND SUBSYSTEMS

The OSO-7 spacecraft provides a spin-stabilized platform for solar-oriented scientific instruments. Solar and celestial instruments not requiring fixed solar orientation are housed in the spinning wheel section of the spacecraft.

The spinning section of the spacecraft is a nine-sided wheel, divided into nine wedge-shaped compartments. Five of these compartments contain the instrument hardware, and the remaining compartments house the spacecraft electronic controls, batteries, telemetry equipment, and radio command equipment. A high-pressure (3000 psi) storage vessel is mounted in the center hub section of the wheel to supply nitrogen gas to jets mounted on the wheel rim for spin-rate control.

A rectangular-shaped sail, mounted on the wheel by means of an azimuth drive assembly, carries the solar cell array and pointed instruments. Figure 3-1 illustrates the OSO-7 overall configuration. Two 3000-psi nitrogen gas vessels are mounted at the base of the sail to supply gas to precession jets located on the sail structure. An array of solar cells is mounted on the solar-oriented sail section to supply electrical power to the spacecraft.

The structures are connected by an azimuth drive assembly (ADA) attached to the base of the sail and mounted in the center of the wheel by a support ring structure on the top side of the wheel hub. This drive assembly contains a shaft which is held in position by precision bearings at the top and bottom of the assembly. Mounted on the shaft between the bearings is a torque motor which actively controls the azimuth position of the sail. On the base of the shaft is a slip ring assembly that carries power, telemetry, and control signals between the solar-oriented sail section and the spinning wheel section. Also on the ADA bottom is a magnetic "blipper" that produces a relative sail/wheel azimuth pulse once per wheel revolution.

Dimensions of the spacecraft are shown in Figure 3-2. Total observatory weight is 1415.5 pounds. Space is provided on the sail for two scientific instruments: one is approximately four inches wide by twelve inches high by 49 inches long, and the other seven inches wide by twelve inches high by 52 inches long. The two sail instruments weigh approximately 185 pounds total. The four wheel instruments weigh approximately 275 pounds total. See Table 3-1 for the OSO-7 breakdown of instrument and spacecraft subsystem weights and Table 3-2 for the overall OSO-7 mass property summary.

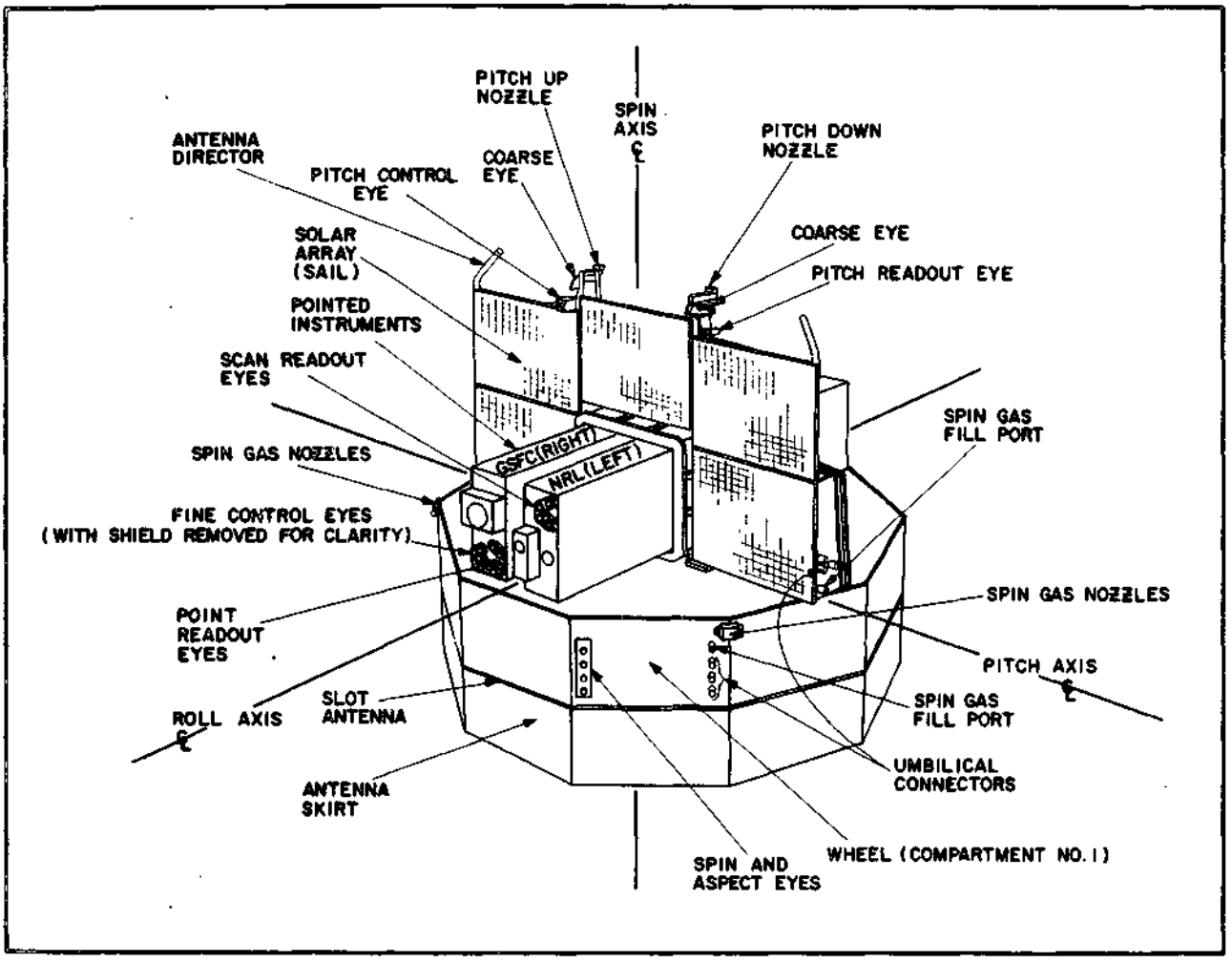

Figure 3-1 OSO-7 Configuration

3.1.1 Power Subsystem

Solar energy is converted into 97 watts of electrical power by the 10 square-foot solar cell array mounted on the sun-oriented sail section. This power charges the batteries and supplies the observatory when the spacecraft is in sunlight. The observatory uses 65 watts in orbit day and 40 watts in orbit night.

The nominal 19-volt battery is made up of 56 nickel-cadmium cells distributed in 8 packs of 7 cells each. The battery pack voltage range is from 16.2 volts (undervoltage shut-down level) to 21 volts (fully-charged level). Dummy loads can be connected or a portion of the solar array cut-out, by ground command, to prevent overcharging the battery in case of low power demand.

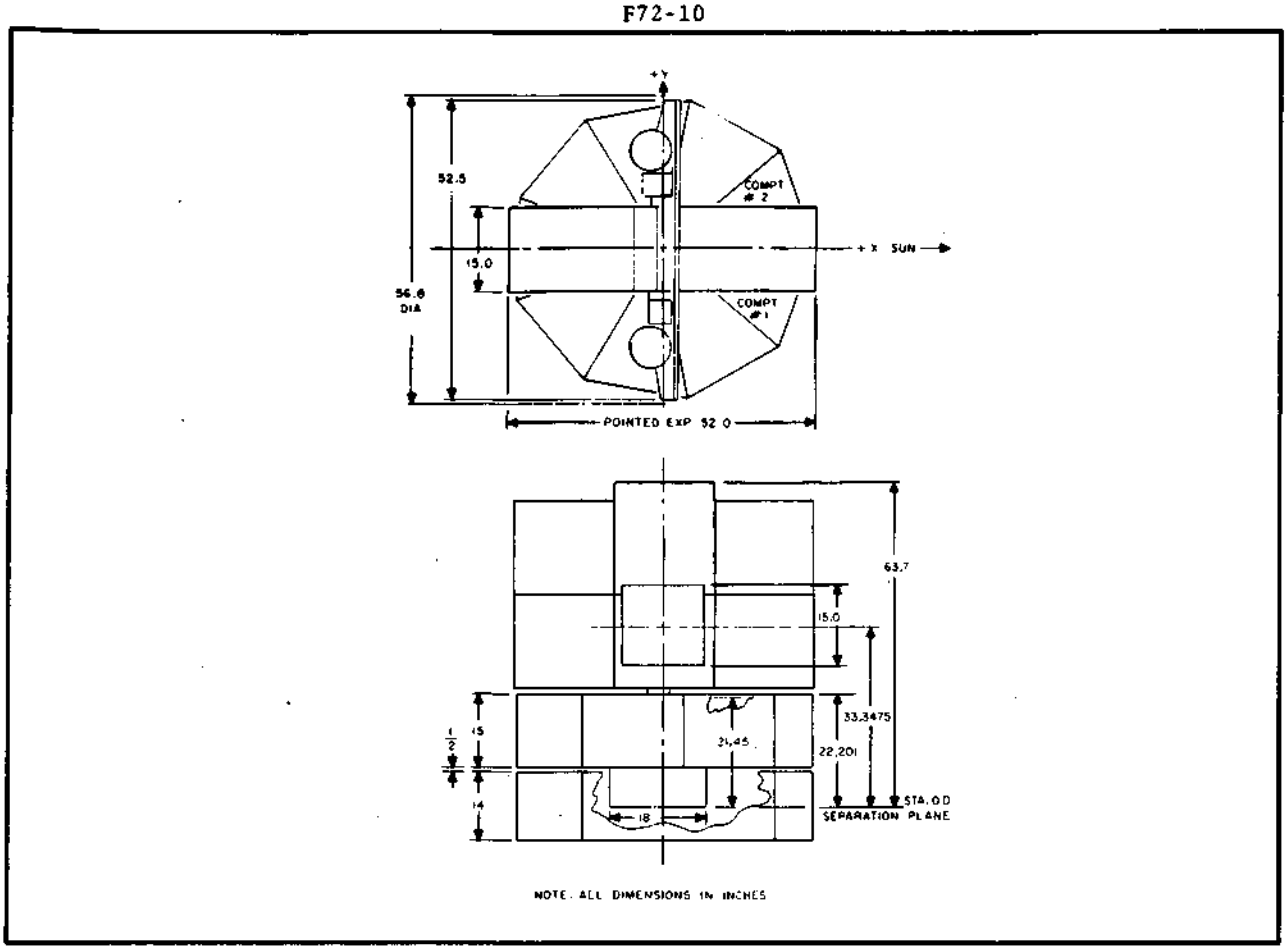

Figure 3-2 OSO-7 Structural Dimensions

3.1.2 Telemetry Subsystem

Figure 3-3 is a block diagram of the OSO-7 telemetry subsystem. OSO-7 has a PCM/PM system which uses a split-phase binary code. Data are time-multiplexed into a 32-word main frame with 8 bits-per-word (256 bits-per-frame). Supercommutation and subcommutation techniques are used to format experiment and housekeeping data. The data are transmitted at 800 bits per second over a 136.29 MHz downlink, and are simultaneously tape recorded for once per orbit playback by ground command. 48-channel analog subcommutators in the sail and wheel sample spacecraft and experiment housekeeping data at a rate of one sample per main frame (every 0.32 second).

Subcommutator data are multiplexed into main frame words and data are also sub-submultiplexed using three sub-subcommutators producing one word each 15.36 seconds. A 48-channel digital submultiplexer handles spacecraft aspect data and main frame count information.

Table 3-1
OSO-7 WEIGHT BREAKDOWN BY INSTRUMENT PAYLOAD AND SUBSYSTEM

	WHEEL-MOUNTED		SAIL-MOUNTED		OBSERVATORY	
	Weight, Lb	% of Wheel Weight	Weight, Lb	% of Sail Weight	Weight lb	% of Total Observatory Weight
Instrument Payload	MIT: 60 UCSD-S: 39 UNH: 74 UCSD-C: 102 (Incl. Elect.) } 275.0	28.9	GSFC Pointed: 75 NRL Pointed: 107.5 Thermal Monitor: 2.5 } 185.0	40.1	460.0	32.5
Control Subsystem	105.5	11.0	90.7	19.7	196.2	13.9
Data Handling Subsystem	39.0	4.1	0.6	0.1	39.6	2.8
Command Subsystem	11.2	1.2	11.6	2.5	22.8	1.6
RF Subsystem	52.7	5.5	0.2	0.0	52.9	3.7
Power Subsystem	50.2	5.3	19.2	4.2	69.4	4.9
Electrical Distribution	35.7	3.7	32.3	7.0	68.0	4.8
Structure	174.0	18.2	100.8	21.9	274.8	19.4
Ballast (Includes Weight for Dynamic Balance and Inherent Dynamic Stability)	211.2	22.1	20.6	4.5	231.8	16.4
Totals	954.5		461.0		1415.5	

3.1.3 Command Subsystem

OSO-7 has a PDM/AM/AM tone-digital command subsystem (Figure 3-4) with a maximum capacity of 476 discrete commands. Many of these commands are combined for redundancy, so that 282 commands are actually used. The rf signal (149.52 MHz) is 80 percent amplitude-modulated by an audio tone (7.7 kHz) which is pulse-duration-modulated by the coded digital command.

Two command receivers, whose inputs come from a hybrid circulator in the antenna subsystem, operate continuously for protection against a single receiver failure. The outputs of the receivers are pulse-duration-modulated audio tones and are fed into the seven decoders. Two decoders are hard-wired to individual receivers, and five decoders may be addressed through either receiver by appropriate switching of the receiver's output. The decoder outputs actuate relays or transistor switches for command execution.

Table 3-2
OSO-7 LAUNCH MASS PROPERTIES[1]

Property	Launch Value
Observatory Weight	1415.5 lbs
Observatory CG Above Separation Plane	21.9 in.
Observatory Total Spin MOI	112.20 slug-ft^2
Observatory Transverse MOI About X-Axis	89.65 slug-ft^2
Observatory Transverse MOI About Y-Axis	87.55 slug-ft^2
Wheel Weight	954.5 lbs
Wheel CG Above Separation Plane	16.0 in.
Wheel Spin MOI	92.8 slug-ft^2
Wheel Lateral CG Offset From Observatory Centerline[2]	<0.050[3] in.
Wheel Principal Axis of Inertia With Respect to Observatory Centerline	<0.002[4] radians
Wheel Transverse MOI About Line Parallel to X-Axis Through Wheel CG	53.65[5] slug-ft^2
Wheel Transverse MOI About Line Parallel to Y-Axis Through Wheel CG	53.55[5] slug-ft^2
Sail Weight	461.0 lbs
Sail CG Above Separation Plane	32.7 in.
Sail Spin MOI	19.6 slug-ft^2
Sail Lateral CG Offset From Observatory Centerline	<0.320[6,8] in.
Sail Principal Axis of Inertia With Respect to Observatory Centerline	<0.005[7,8] radians
Sail Transverse MOI About Line Parallel to X-Axis Through Sail CG	17.0[5] slug-ft^2
Sail Transverse MOI About Line Parallel to Y-Axis Through Sail CG	15.0[5] slug-ft^2

[1] These are actual measured properties just prior to shipment of OSO-7 to Cape Kennedy.

[2] Observatory centerline is defined as line perpendicular to observatory/vehicle separation plane and passing through the center of the spacecraft/attach fitting interface diameter.

[3] Wheel CG with respect to bearing axis is aligned during dynamic balance within 0.001" for in-orbit observatory balance about bearing axis. However, due to tolerance build-up between bearing axis and attach fitting, wheel lateral CG shift cannot be guaranteed better than <0.050" from observatory centerline.

[4] Wheel PAI with respect to bearing axis is aligned during dynamic balance within 0.0003 radian, but again cannot be guaranteed better than 0.002 radian from observatory centerline due to bearing axis/observatory centerline misalignment possible.

[5] Transverse MOI's of sail and wheel are not measured, just calculated with an accuracy of 1.0 slug-ft^2.

[6] Sail CG with respect to bearing axis is aligned during dynamic within 0.004" for in-orbit observatory balance about bearing axis. However, due to bearing axis/observatory mialignment possible plus sail launch unbalance due to NRL pointed instrument being 1.16" behind in-orbit position, sail lateral CG shift cannot be guaranteed better than 0.320" from observatory centerline.

[7] Sail PAI with respect to bearing axis is aligned during dynamic balance within 0.0012 radian for in-orbit condition. But due to bearing axis/observatory centerline misalignment possible, and due to 0.002 radian effect of NRL instrument, sail PAI with respect to observatory centerline cannot be guaranteed better than <0.005 radian.

[8] The static and dynamic values discussed in notes 6 and 7 are given because at launch vehicle time 227.450 plus the sail will be spun to 40 ± 10 RPM.

B

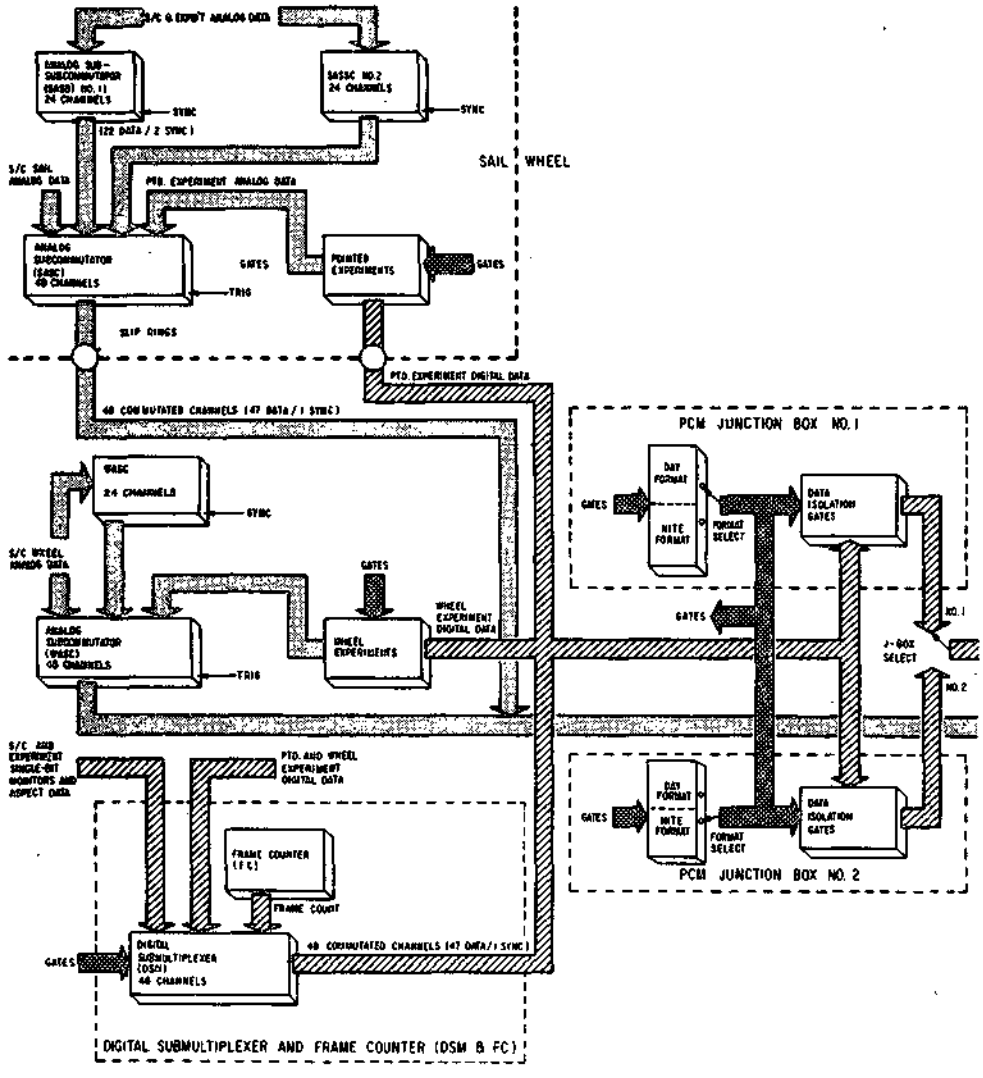

Figure 3-3 OSO-7 Telemetry Subsystem Block Diagram (1 of 2)

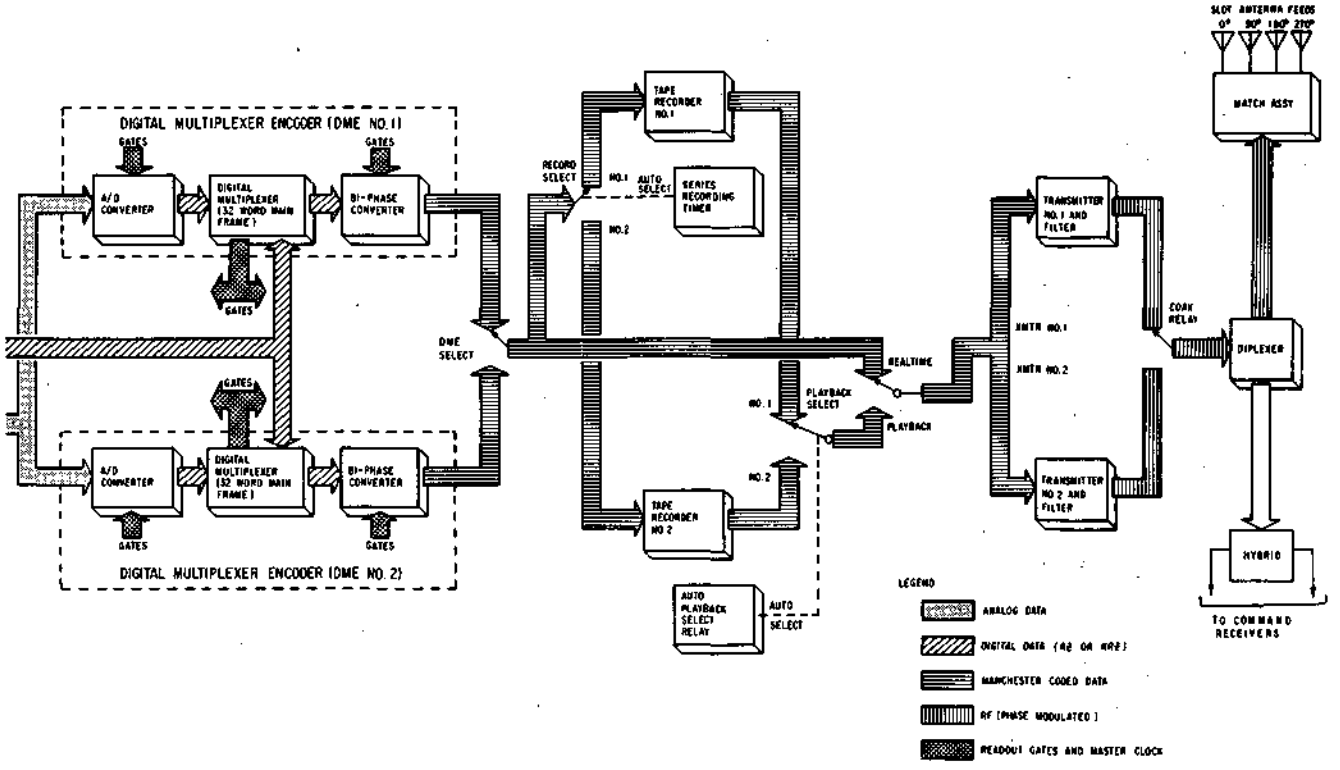

Figure 3-3 OSO-7 Telemetry Subsystem Block Diagram (2 of 2)

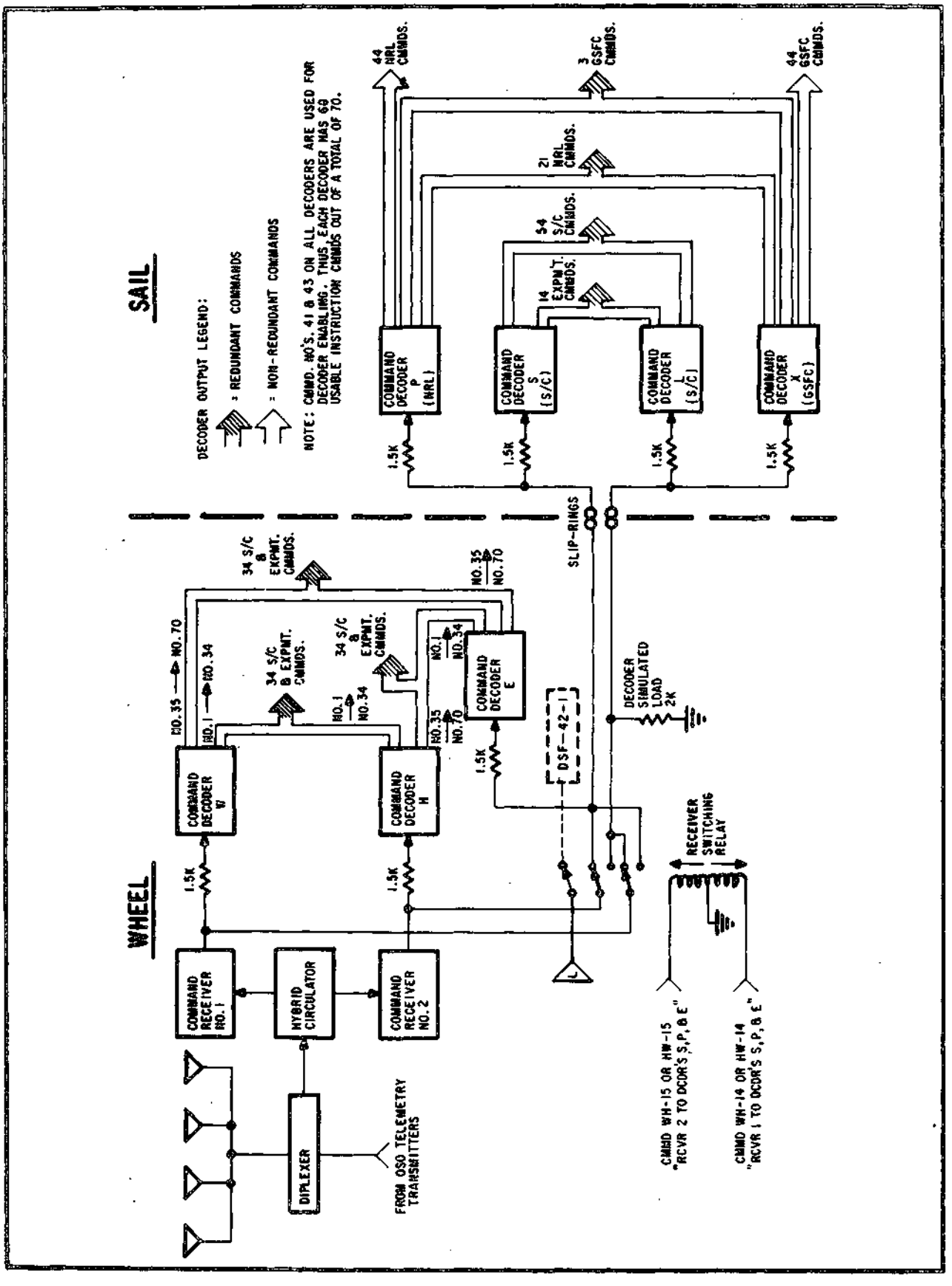

Figure 3-4. OSO-7 Command Subsystem Block Diagram

3.1.4 RF Subsystem

The rf subsystem consists of an antenna array, coaxial relay, a diplexer, a hybrid circulator, a coaxial relay, and redundant transmitters and premodulation filters.

The antenna is a progressively-fed turnstile slot consisting of a circumferential slot backed by an approximate quarter-wave cavity which is excited at four equally spaced feed points on a constant radius near the slot end. Each feed point is fed from an antenna matching assembly that provides the proper phase and power splitting. A coaxial relay controlled by the transmitter selection commands connects the selected transmitter to the diplexer. The diplexer, consisting of a lumped constant network isolates the transmitting and receiving systems when they are connected to a common antenna.

A hybrid circulator (lumped-constant bridge circuit) permits the simultaneous operation of two receivers at the same frequency from a single antenna subsystem. The transmitters are phase-modulated operating at a center frequency of 136.29 MHz. Premodulated filters are used to limit the spectrum to a 90 kHz bandwidth at the -10 dB points. The output power is about +27 dBm.

3.1.5 Orientation Control Subsystem

The spin control subsystem provides automatic wheel spin-up and spin-down between the limits of 26 and 40 rpm. Spin control is switched from automatic to manual control by the spin backup circuit, should the spin rate decrease to less than 25 rpm or exceed 42 rpm. The spacecraft spin axis is maintained normal to the sun line within ±3 degrees by an automatic pitch control system using gas jets and a manual control system using a magnetic pitch coil. Pitch attitude can also be controlled manually by ground commands.

Scientific instruments which do not require fixed solar orientation are located in the wheel section of the observatory. The sun lies near the wheel's plane of rotation and is observed about once every two seconds. Thus, solar investigations by these instruments repeatedly monitor the flux of the entire sun. Also, the wheel plane can be maintained nearly perpendicular to the ecliptic plane so that the observatory will pitch about one degree per day in following the apparent motion of the sun. An adjustable magnetic pitch coil generates a controlled magnetic field that interacts with the earth's field to cause the necessary slow precession of the spacecraft. Thus, radial-looking instruments on the wheel will observe the entire celestial sphere in about six months.

A passive nutation damper keeps the wheel plane excursions to near zero and a star scanner accurately determines the instantaneous celestial look angle of the wheel experiments.

Azimuth control of the sail is accomplished by a servo system that uses a torque motor to drive the sail in a direction opposite to the spinning wheel to keep the sail facing the sun continually. When the spacecraft is in darkness, the sail is maintained in the day attitude by a position gyro system. At night, the sail can also be moved to any desired azimuth position, using this gyro system.

Fine pointing of the pointed instruments is accomplished in azimuth by the servo system described before and in elevation by a servo system using a torque motor mounted on the elevation frame to which the pointed instruments are mounted. Two scientific instruments, concerned solely with solar activity, are oriented in any of five pointing modes as selected by ground command. Figure 3-5 illustrates these pointing modes.

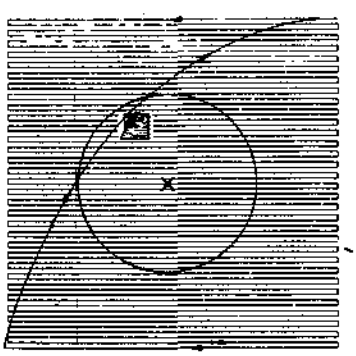

SUN-CENTERED POINT MODE— PIA IS ORIENTED TO CENTER OF SOLAR DISK.

LARGE RASTER MODE— PIA SCANS SOLAR DISK WITH RASTER PATTERN HAVING THE FOLLOWING CHARACTERISTICS:

- *NORMAL RASTER*—60 x 60 ARC MINUTE SIZE WITH 64 LINES 0.937 ARC MINUTES APART; LINE SWEEP RATE IS 60 ARC MINUTES PER 7.68 SECONDS; TOTAL RASTER TIME IS 8 MINUTES, 11.52 SECONDS.
- *INTERLACED RASTER*—IDENTICAL TO NORMAL RASTER EXCEPT IS DISPLACED DOWNWARD BY ONE-HALF RASTER INTERVAL AND IS ALTERNATED WITH NORMAL LARGE RASTER.

OFFSET POINT MODE— PIA CAN BE ORIENTED TO ANY OF 16384 POINTS WITHIN A 128 x 128 POINT GRID (60 x 60 ARC MINUTES).

SMALL RASTER MODE— PIA SCANS PORTION OF SOLAR DISK WITH 5 x 5 ARC MINUTE PATTERN CENTERED ON ANY OFFSET POINT; CONSISTS OF 16 LINES 0.313 ARC MINUTES APART; THE LINE SWEEP RATE IS 5 ARC MINUTES PER 3.84 SECONDS; THE TOTAL RASTER TIME IS 61.44 SECONDS.

GYRO POINTING MODE (USED NORMALLY DURING NIGHT)— THIS MODE CAN BE USED TO ORIENT THE SAIL (IN AZIMUTH ONLY) TO WITHIN 24 ARC MINUTES OF A DESIRED TARGET, AZIMUTH SCAN AT UP TO 0.33 DEGREES PER SECOND, OR MOVE THE SAIL IN 0.05 DEGREE INCREMENTS.

NOTES:
1. POINTING MODES ARE ACTUATED BY GROUND COMMANDS.
2. SERVO POINTING MODES HAVE LONG TERM ABSOLUTE ACCURACY OF BETTER THAN 1 ARC MINUTE AND RELATIVE ACCURACY OF ~0.25 ARC MINUTES; SHORT TERM JITTER IS LESS THAN 5 ARC SECONDS.
3. PIA = POINTED INSTRUMENT ASSEMBLY.

Figure 3-5 Pointing Modes

3.1.6 Spacecraft Subsystem Configuration Drawings

Figures 3-6 through 3-12 show the general locations and shapes of the spacecraft subsystem components.

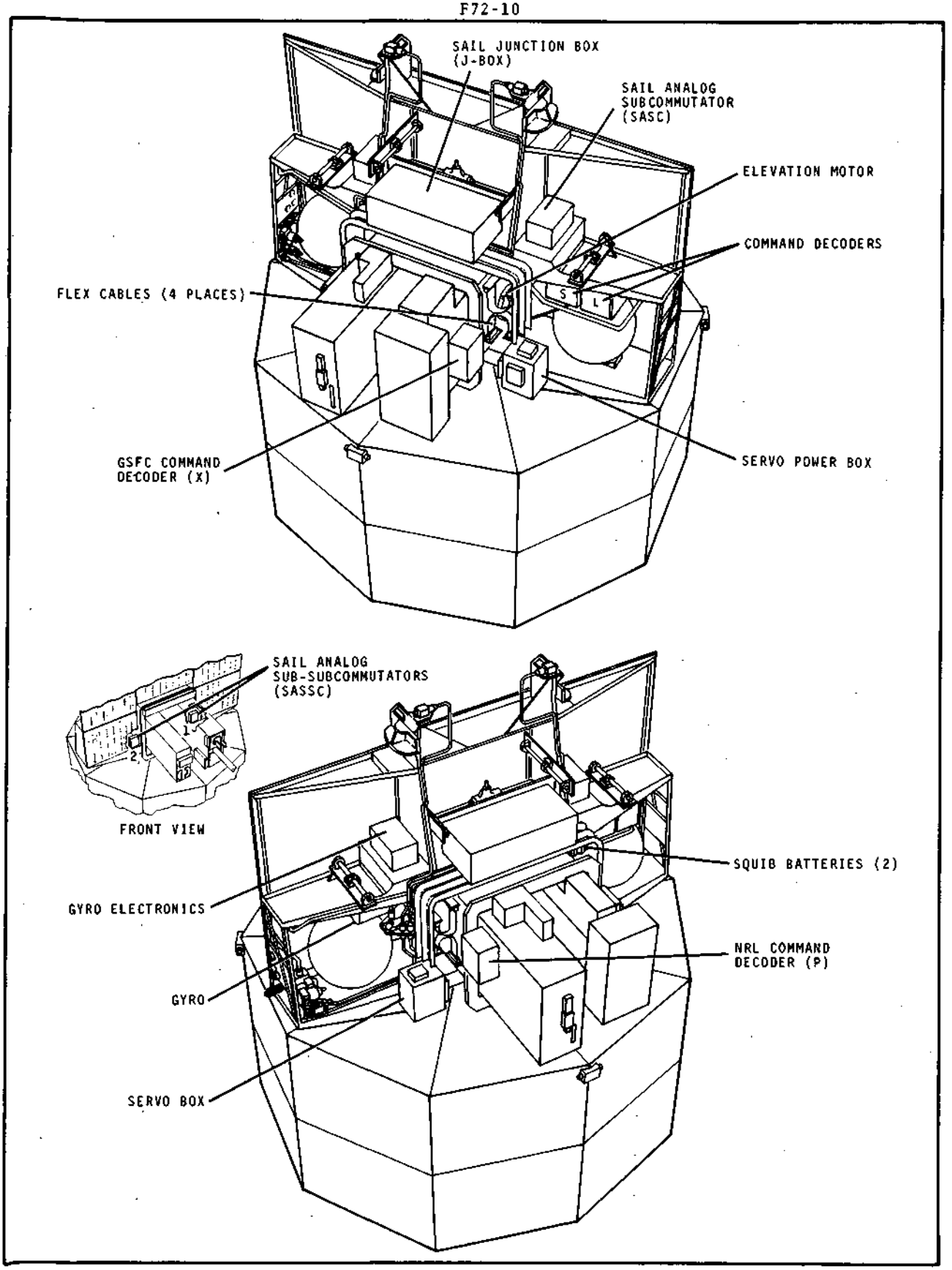

Figure 3-6 Sail Electronics Configuration

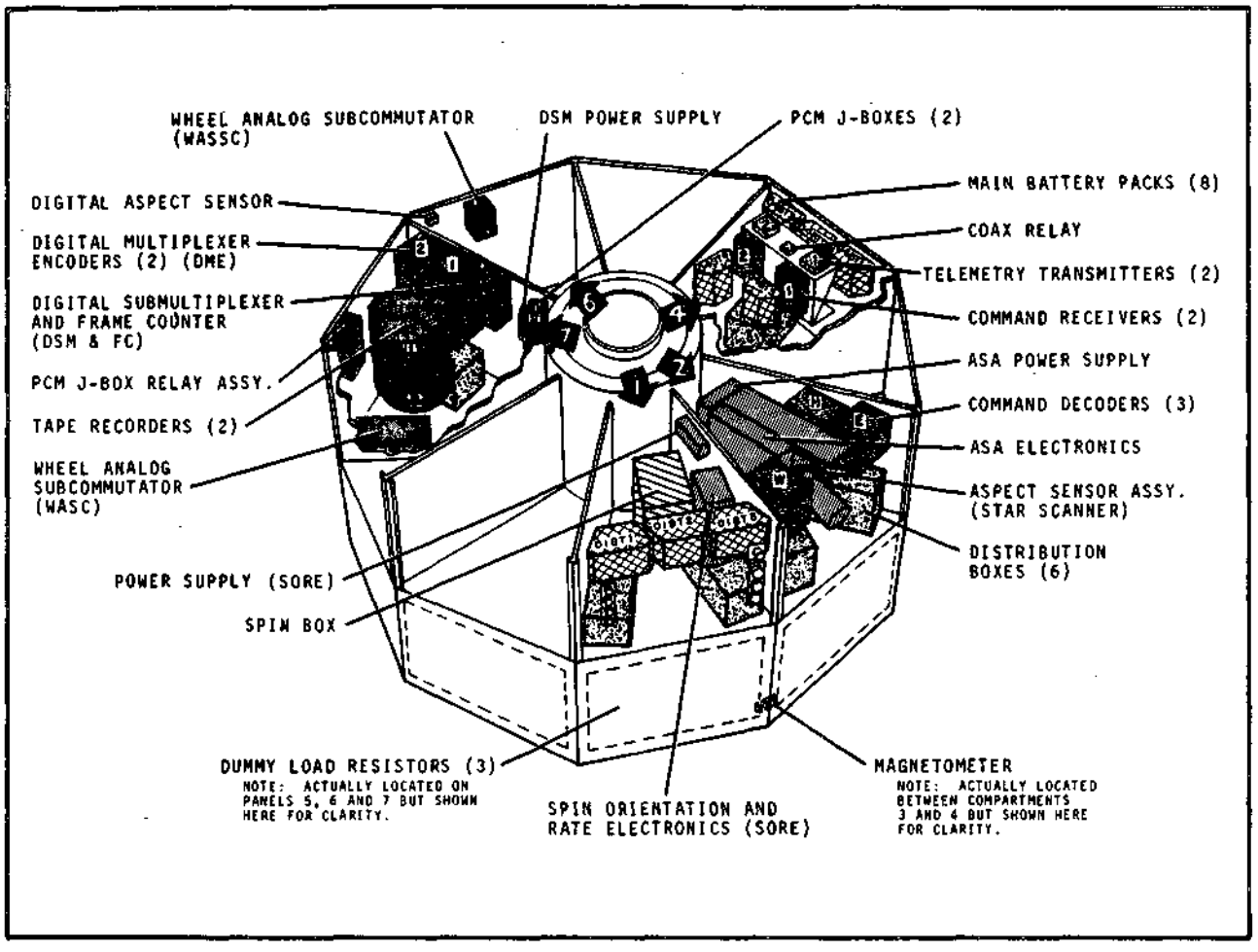

Figure 3-7 Wheel Electronics Configuration

3.2 OSO-7 SAIL INSTRUMENT PAYLOAD

The objectives, operational modes, and design of the numerous scientific experiments to be conducted by the Goddard Space Flight Center Spectroheliometer, the Naval Research Laboratories Coronagraph, and the Goddard Space Flight Center Thermal Control Coating instrument, all of which are integrated into the OSO-7 sail, are summarized below. The instruments are mounted as shown in Figure 3-13.

3.2.1 GSFC EUV/X-Ray Spectroheliometer

The GSFC spectroheliometer (Figure 3-14) is one of the two primary sail-mounted, solar-oriented instruments. It monitors portions of the EUV and X-ray spectra to enable analysis of the structure and temperatures of the sun's chromosphere and corona, particularly during

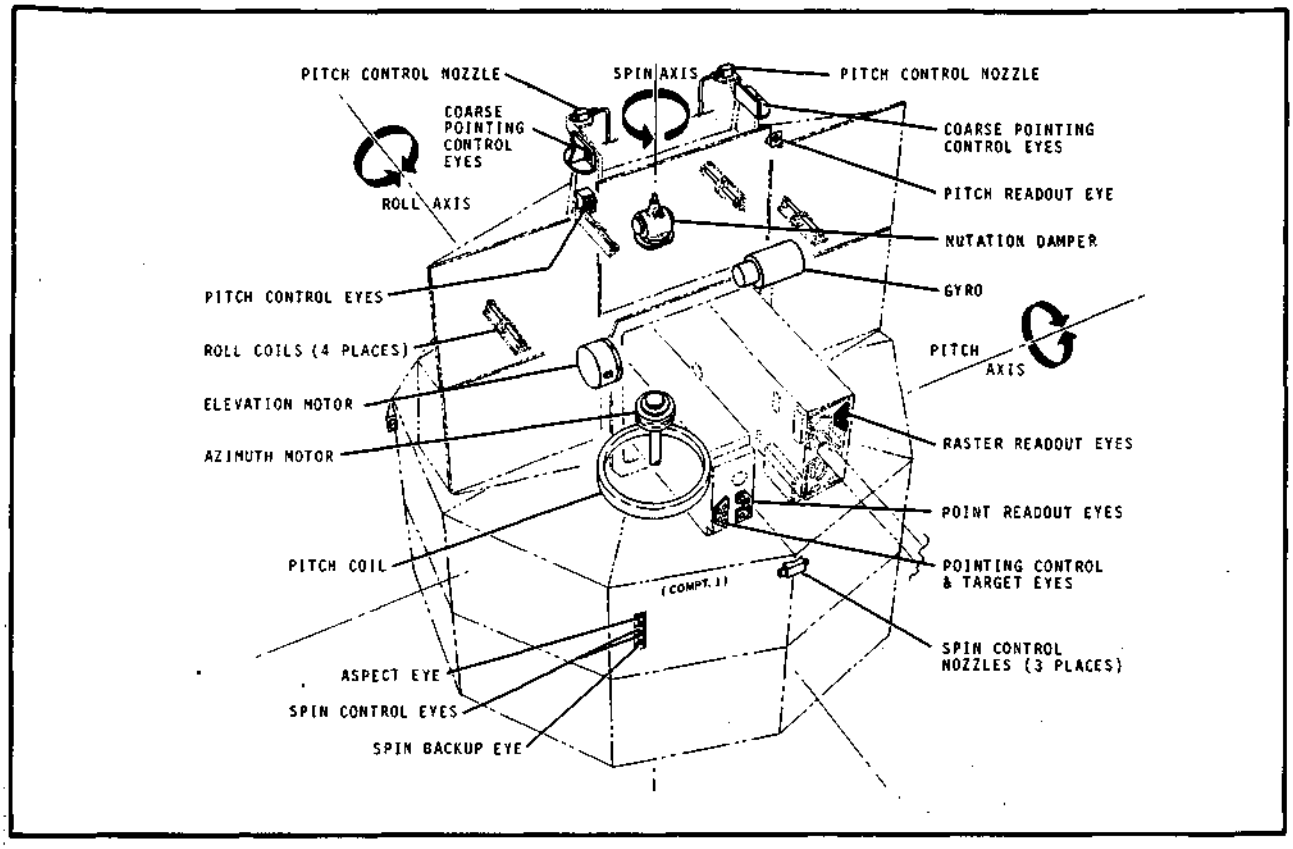

Figure 3-8 Control Subsystems Configuration

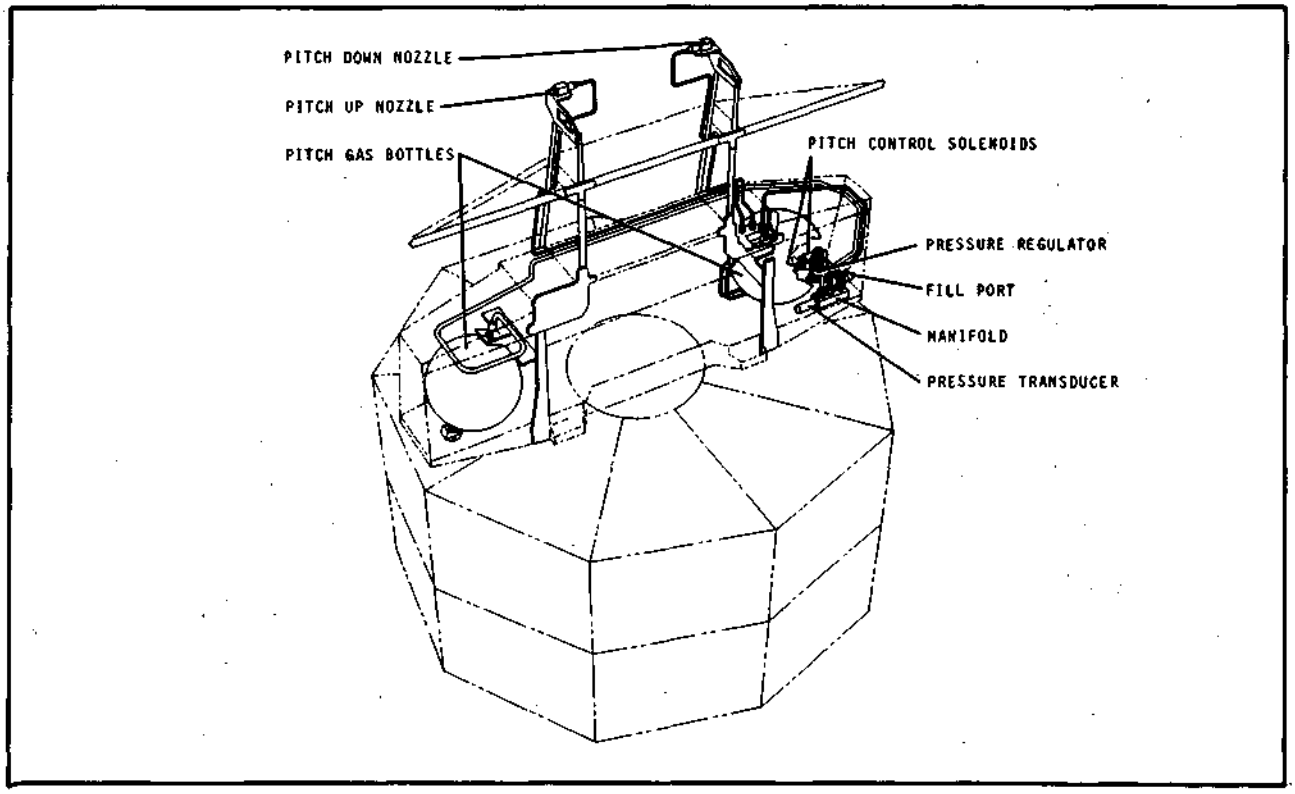

Figure 3-9 Pitch Pneumatics Configuration

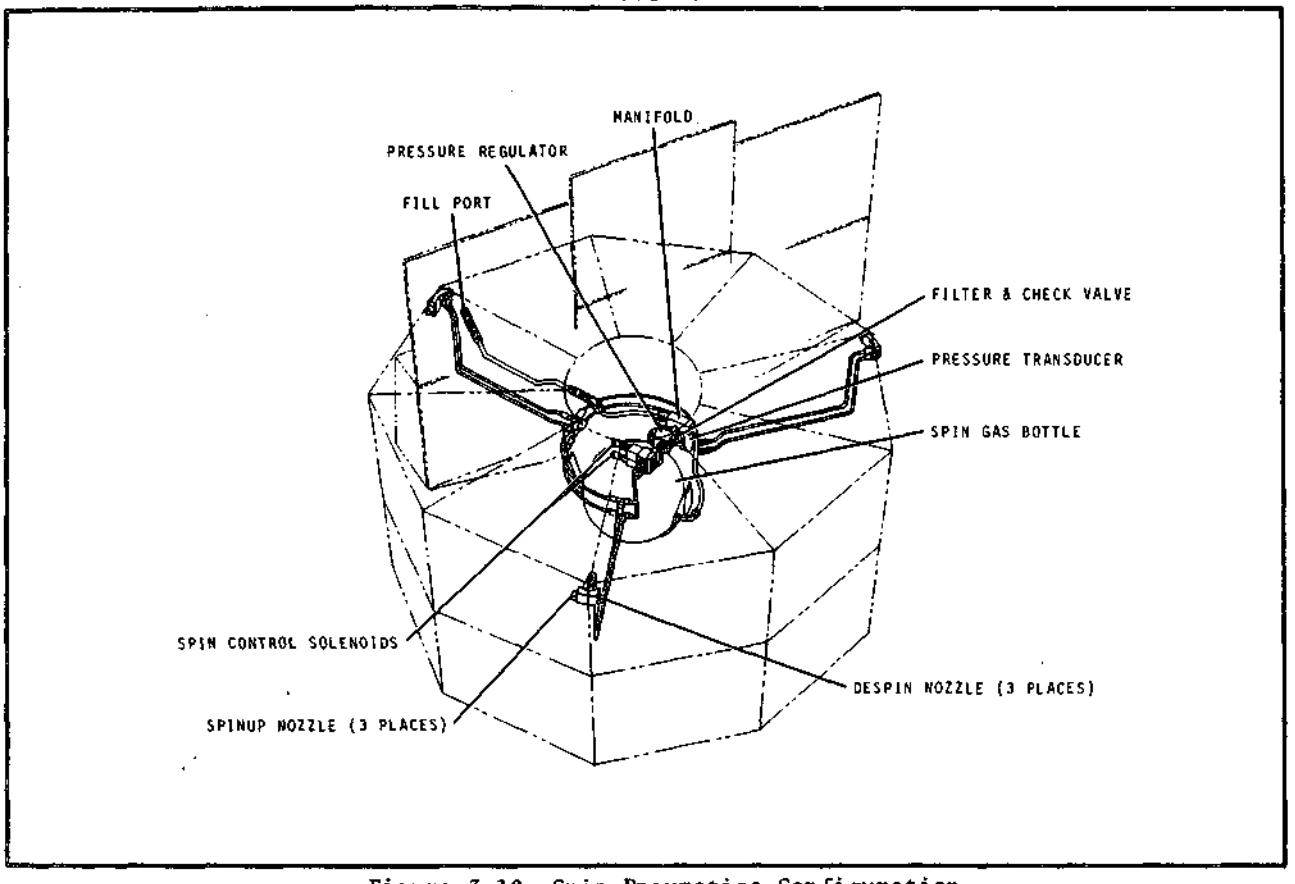

Figure 3-10 Spin Pneumatics Configuration

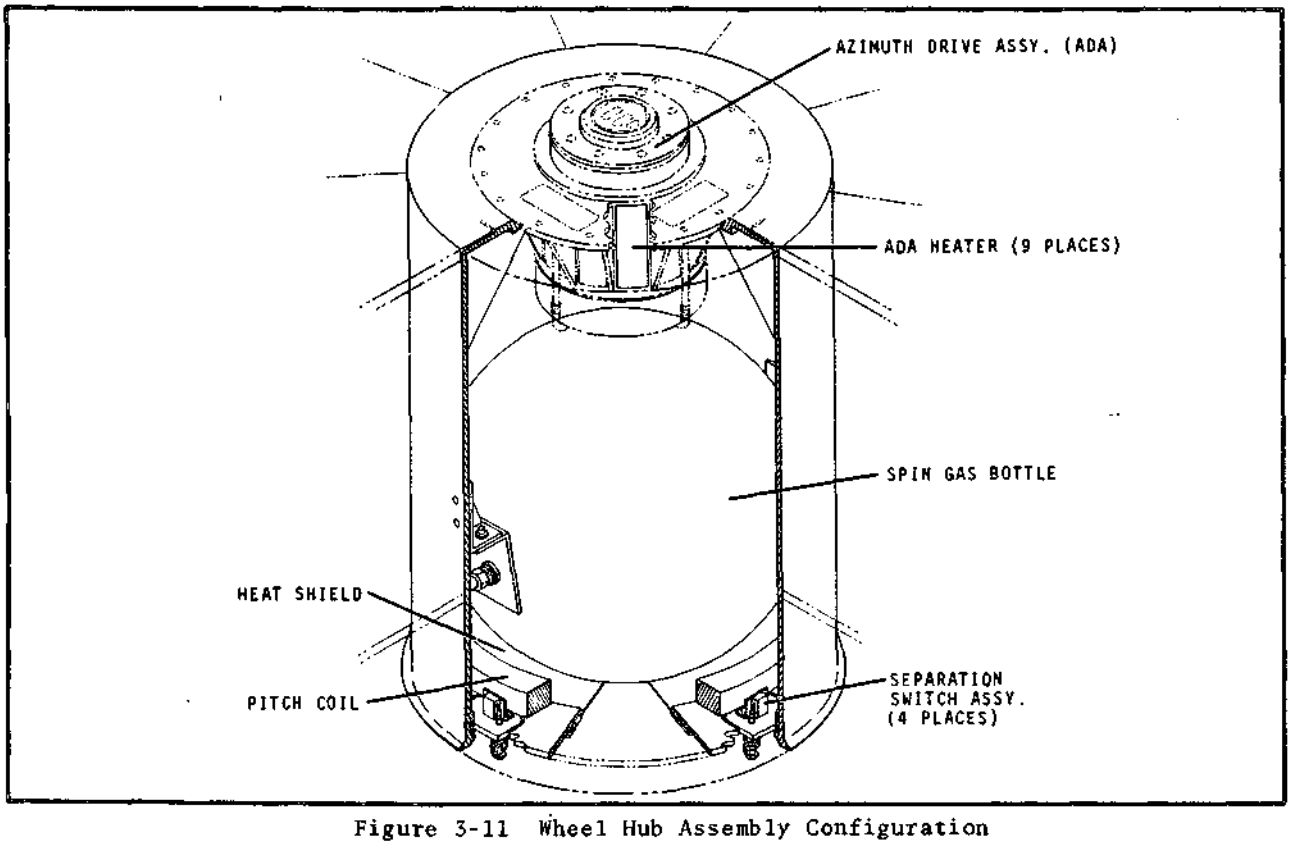

Figure 3-11 Wheel Hub Assembly Configuration

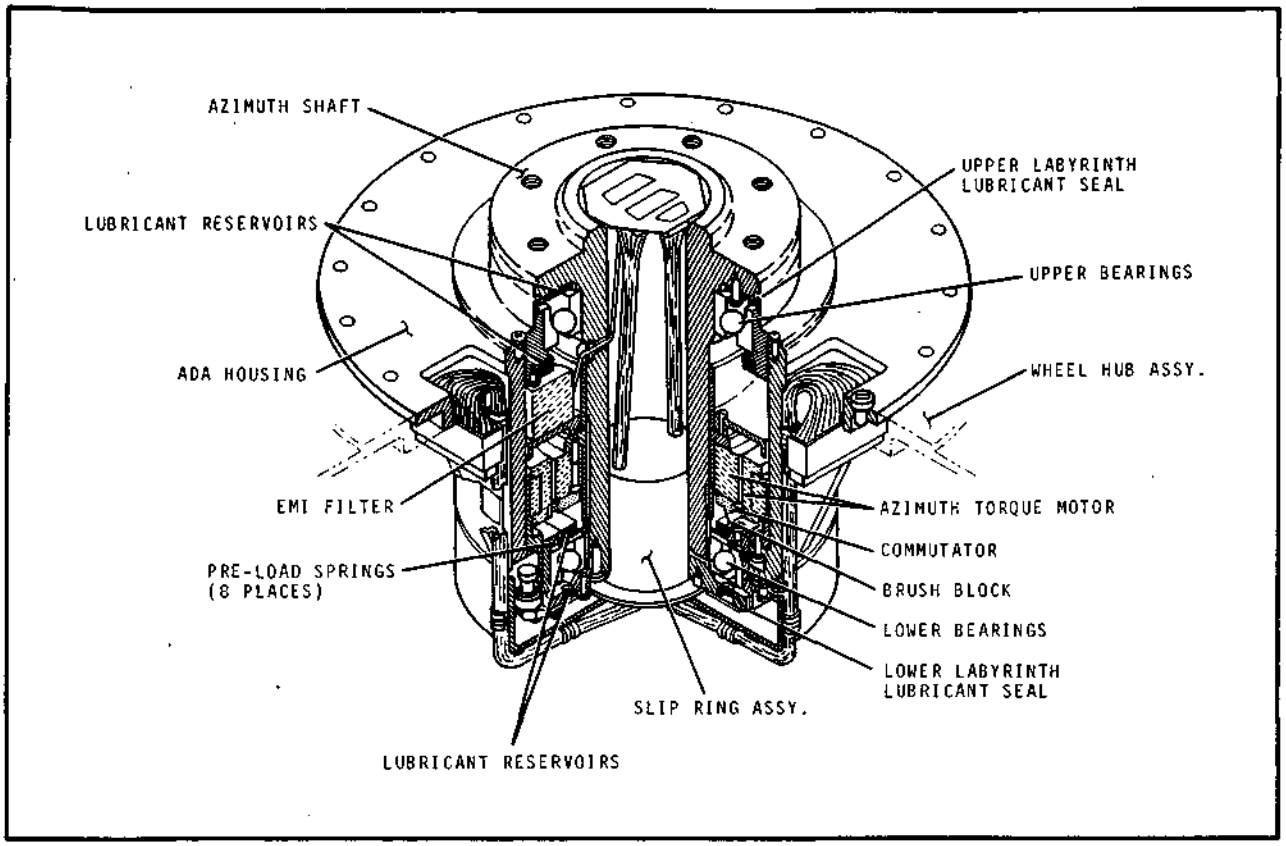

Figure 3-12 Azimuth Drive Assembly Configuration

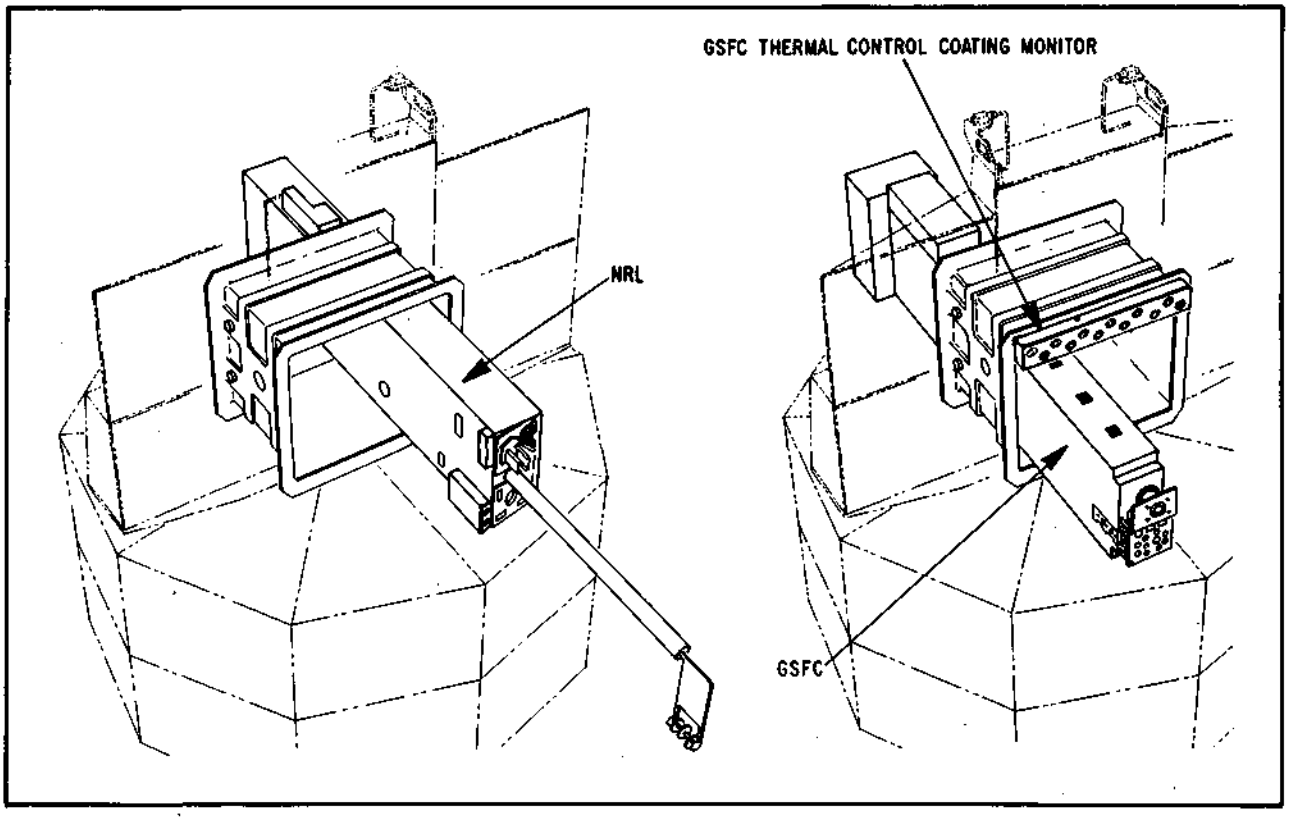

Figure 3-13 OSO-7 Sail Instrument Payload

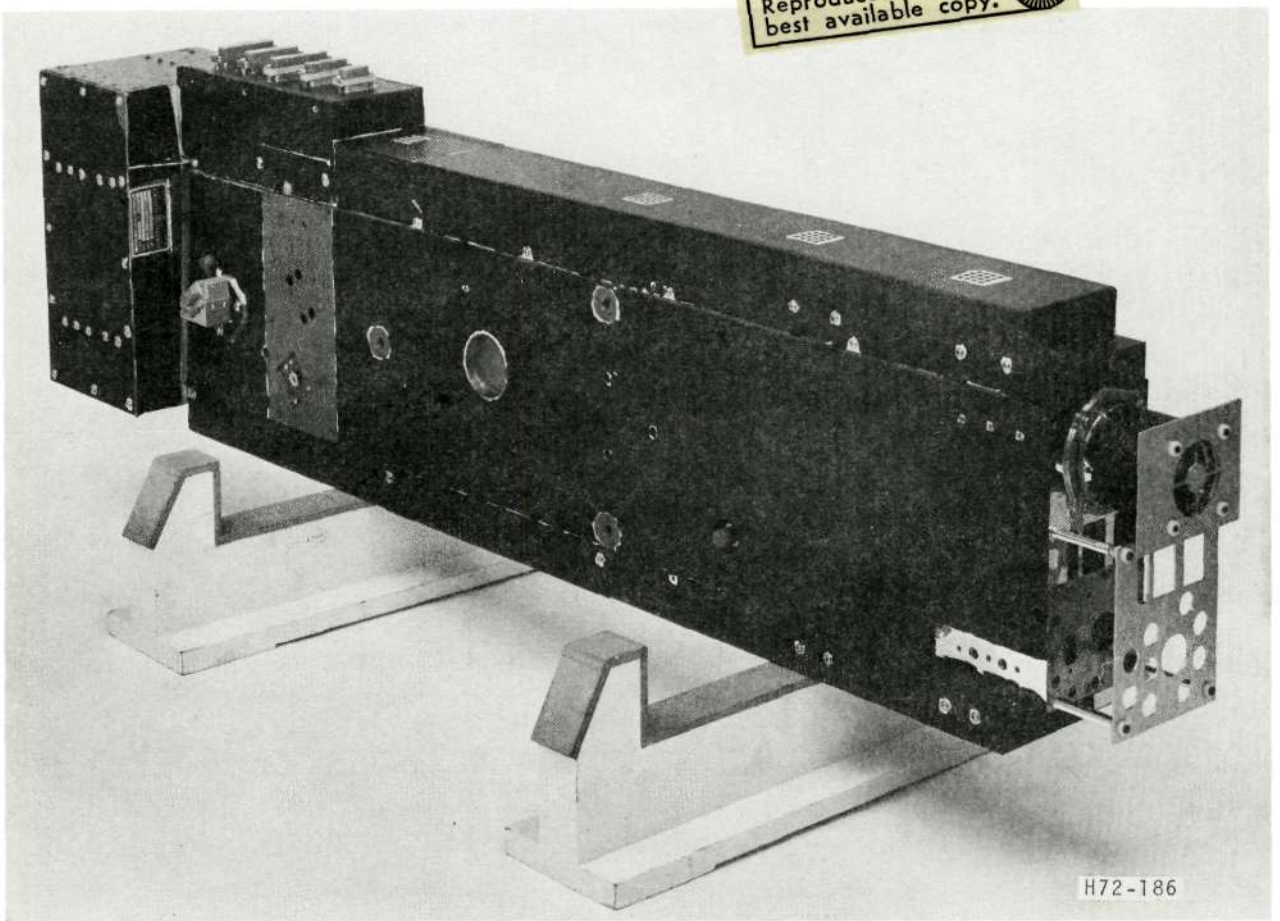

Figure 3-14 GSFC EUV/X-Ray Spectroheliometer

active periods and in local regions of high activity. Actually there are five separate monitoring experiments within the GSFC pointed instrument: EUV from 170Å to 400Å with spectral resolution of 1Å; H-α at 6563Å with a wavelength accuracy of ±0.1Å; long X-ray in five (1-2Å) bands from 8Å to 15Å; short X-ray in three (0.1-0.3Å) bands from 1.7Å to 2.5Å; and a polarimeter for analyzing the polarity of flare X-rays in the range of 20 - 40 keV. The spatial resolution of EUV and X-ray experiments is approximately 20 x 20 arc-seconds. Two EUV lines (or one EUV line and the H-α line) plus two X-ray lines can be monitored simultaneously. The primary functional mode of operation is to map the solar disc or a localized section of it using the spacecraft large raster or small raster pointing control system. Optional modes include spectral scanning in EUV and X-ray while the pointed instrument assembly is in either the sun-centered or offset point mode.

The primary operational mode involves mapping line emissions from ionized light-weight elements in the "cool" chromosphere and from ionized heavy elements in the intensely hot corona. Because each specific state of ionization has a maximum probability of existing at a specific temperature, the line emission mapping is indirectly a temperature mapping.

The OSO-7 pointing control system provides for large 60 x 60 arc-minute and small 5 x 5 arc-minute square raster patterns. The center of the large 60 x 60 arc-minute raster pattern is the center of the 32 arc-minute diameter solar disk and the center of the small 5 x 5 arc-minute raster pattern can be offset to any point in a 128 x 128 grid within the 60 x 60 arc-minute pattern. In this manner large or localized isothermal maps can be generated at specific selected temperatures from 10,000°K in the chromosphere to several million°K in the corona. The large raster mapping takes 8 minutes and 12 seconds and the small raster mapping takes 1 minute and 1.5 seconds. There is one data point available every 0.04 second for a total of 12288 data points in the 64 line large raster pattern and 1536 data points in the 16-line small raster pattern. These are divided amongst the four simultaneously active channels.

The EUV instrument uses a grazing incidence Cassegrainian telescope to focus the solar radiation on the primary slit of a grating spectrometer whose resolution can be adjusted over the range of 10 x 20 to 60 x 20 arc-seconds. The various discrete wavelengths are detected by three Bendix magnetic electron multipliers mounted on a moving carriage. An H-alpha monitor senses the zero-order radiation from the grating.

The long and short X-ray Ross-type spectroheliographs differ only in the filters and detectors. A grid-type collimator provides spatial resolution of 20 x 20 arc-seconds for the radiation reaching a six-position rotating filter wheel consisting of six pairs of thin metallic membrane filters. The detectors are two-channel proportional counters which view the sun through different filter pairs. The difference in the count rates of the two channels gives the flux in a narrow spectral band, as defined by the transmission characteristics of the filters.

The polarimeter determines the X-ray polarization by scattering the incoming photons from a beryllium block. Six proportional counters are used in anticoincidence around the scattering block to determine the polarization.

Figure 3-15 is a block diagram of the instrument.

3.2.2 NRL WL/XUV Coronagraphs

The NRL Coronagraph (Figure 3-16) is the second primary sail-mounted, solar-oriented instrument. The instrument contains both a white light coronagraph (WLC) and a XUV coronagraph experiment. The WLC uses a telescope and a vidicon to view in detail the outer solar corona from 3900Å to 6500Å. Occulting disks are used to block out the bright solar corona within three solar radii, which leaves a field of view of from three solar radii to ten solar radii (except for a small loss due to occulting disk structural support). The XUV coronagraph uses a separate telescope in viewing the solar corona from 170Å to 550Å. The XUV coronagraph is made up of four individual detectors each of which scans a different, but partially overlapping, 60 x 60 arc-minute region, using the spacecraft large raster mode. The four detectors provide complete spatial coverage out to two solar radii and partial spatial coverage out to five solar radii. The primary objectives of the NRL instrument are to study the outer corona in white light, the inner and limited outer corona in XUV, and to correlate the WL and XUV features, particularly during active periods.

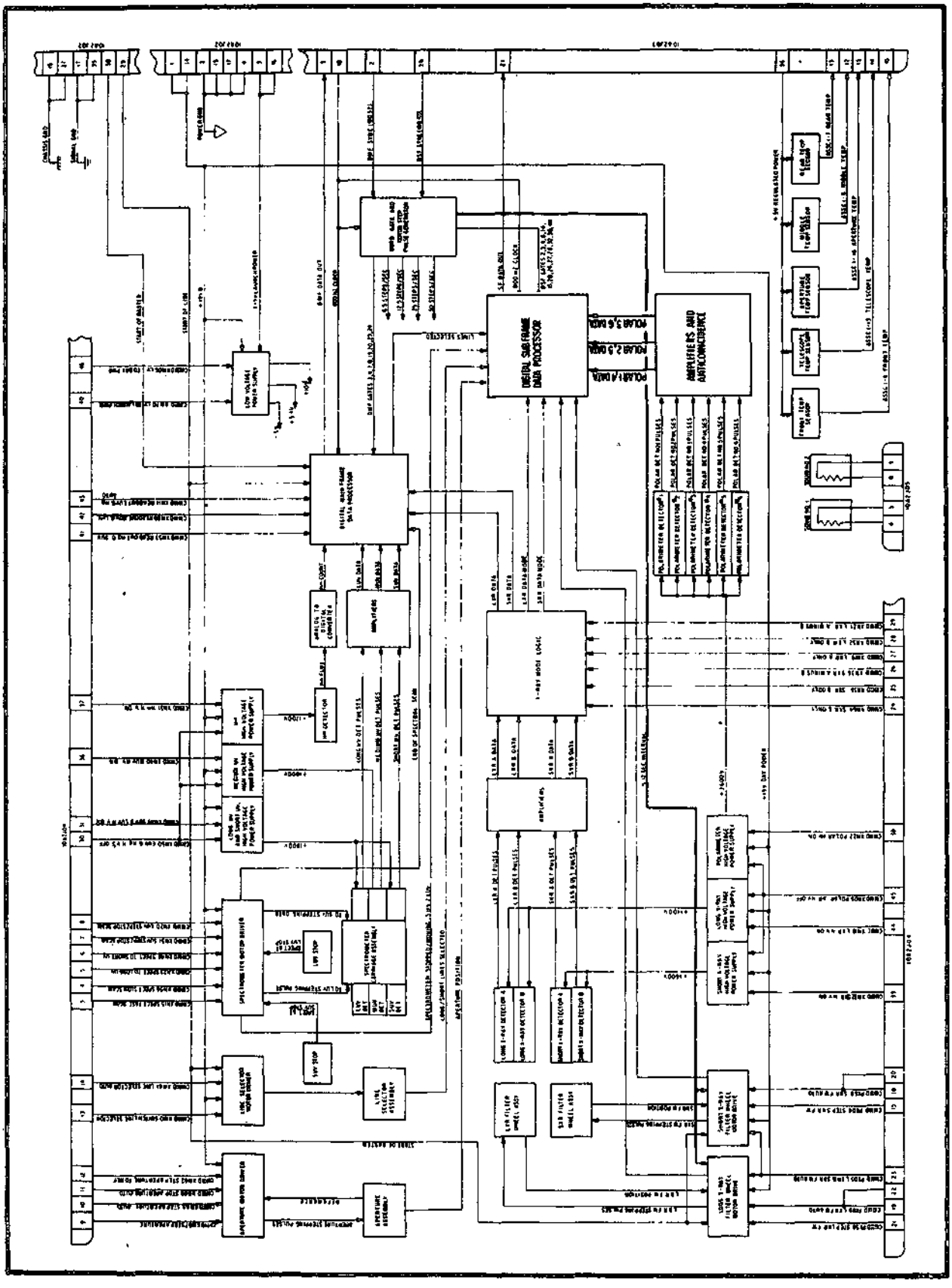

Figure 3-15 Functional Block Diagram for GSFC-EUV/X-Ray Spectroheliometer

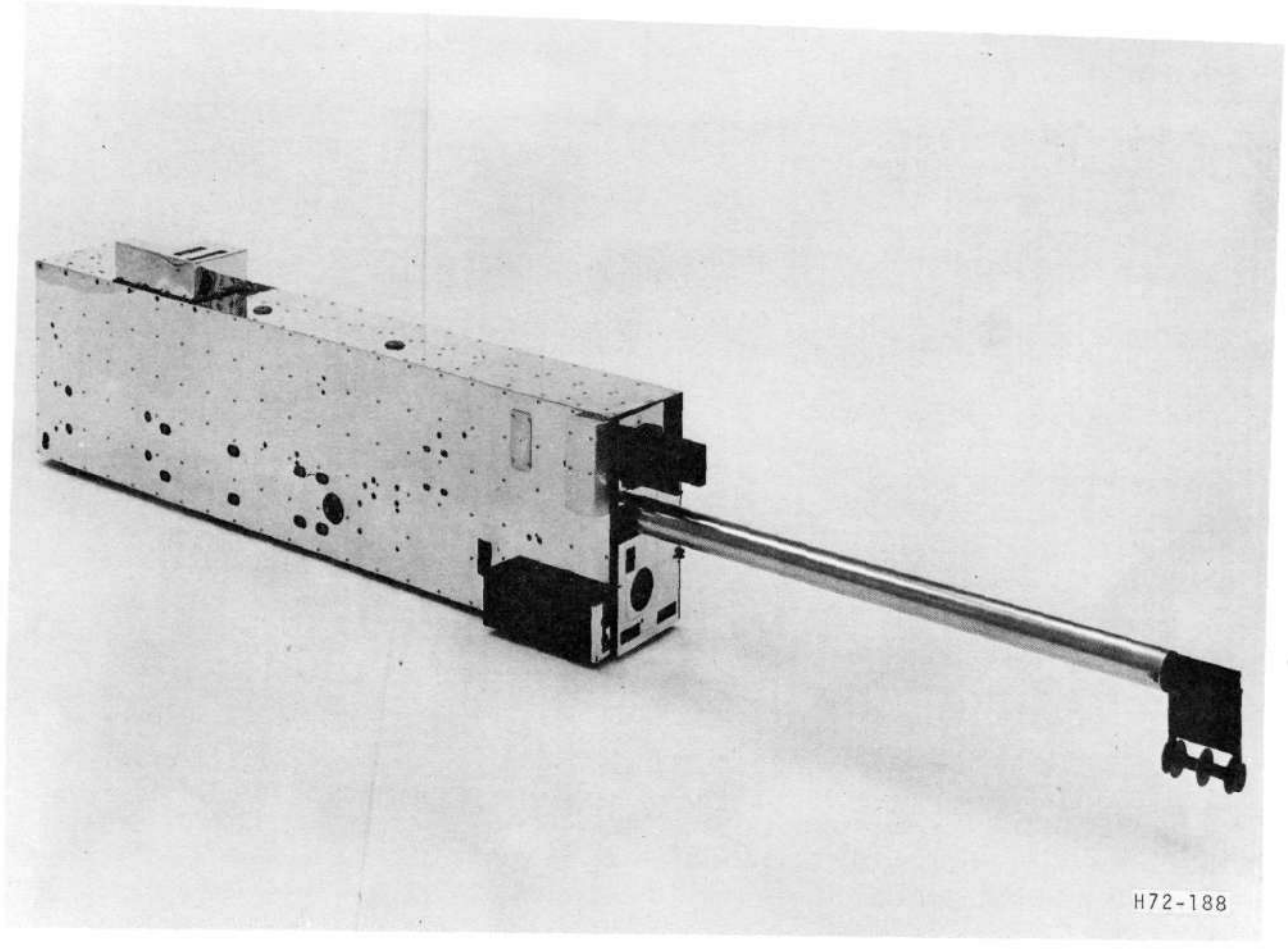

Figure 3-16 NRL-WL and XUV Coronagraphs

Operation of the WLC and the XUV experiments within the NRL pointed instrument must be cycled because the WLC is only useful in the sun-centered point mode and the XUV experiment is only useful in the large raster mode and the experiments share telemetry channels. The vidicon of the WLC is scanned in a 256 x 256 grid which results in a spatial resolution of 1.25 x 1.25 arc-minutes. The intensity of each of the 65,536 elements read-out is digitized on a scale of 0 to 127, which is fully used considering the variable vidicon exposure time of from 0.64 second to 8.96 seconds per line. There are also three alternate operating modes of improved time resolution (lower intensity resolution) if the 40-minute picture time is excessive. The spatial resolution of the sun-centered detector of the XUV coronagraph is 20 x 20 arc-seconds and each of the remaining three XUV detectors has a 1 x 1 arc-minute spatial resolution. There is one data point available every 0.04 second for a total of 12,288 data points in the 64-line large raster pattern. These are divided among the four simultaneously active detector channels.

The WL instrument is a modified Lyot coronagraph which artificially eclipses the sun with the spar-mounted occulting disk assembly. The faint outer corona may then be observed against "black" space. The XUV coronagraph has no occulting boom. It uses an off-axis parabolic mirror, three 100Å aluminum filters, and four Channeltron detectors placed behind slits in the focal plane of the mirror where the sun image is focused. The aluminum filters keep white light out and define the spectral range of XUV of the instrument. The detectors are open-ended channel photomultipliers.

Figure 3-17 is a functional block diagram of the NRL instrument.

3.2.3 GSFC - Thermal Control Coating Monitor

A third instrument, not one of the primary solar physics experiments, is mounted on the elevation frame which holds the primary GSFC and NRL instruments. Twelve thermal control coating specimens are exposed to the vacuum and solar radiation environment of space. By monitoring the temperature of each coating, and the mounting case temperature, it is possible to assess thermal property degradation (absorptivity and emissivity) of the thermal control coatings throughout the mission. The temperature sampling rate of once every 6.15 minutes for each temperature is adequate for such a long-term experiment.

3.3 OSO-7 WHEEL INSTRUMENT PAYLOAD

Integrated into the OSO-7 wheel are the Massachusetts Institute of Technology Celestial X-Ray instrument, University of California-San Diego Cosmic X-Ray and Solar X-Ray instruments, and the University of New Hampshire Gamma Ray Spectrometer. Figure 3-18 shows the location of these instruments on the wheel and the following paragraphs briefly describe each instrument, its function, and its scientific objectives. The descriptions are accompanied by photographs and functional block diagrams.

3.3.1 MIT Celestial X-Ray Telescope

The objectives of the MIT instrument (Figure 3-19) include precise location of known cosmic X-ray sources, identifying and locating new sources having intensities several magnitudes less than known sources, and measuring the intensity and variation of all sources in broad spectral bands from 1 to 60 keV. The five energy bands monitored are: 1 to 1.5 keV, 1 to 4 keV, 3 to 15 keV, 15 to 40 keV, and 30 to 60 keV. Sources as faint as 1×10^{-3} photons/cm^2-sec can be detected. Hundreds of new X-ray sources should be discovered, because this sensitivity is close to the celestial background intensity of 5×10^{-4} photons/cm^2-sec in this energy range.

The instrument has two highly sensitive X-ray detectors which "look" 15° above and below the wheel plane (i.e., above and below the sun) and have conical view angles of 1° and 3°, respectively. The data from the 1° view angle detector is used for fine spatial resolution of sources and the data from the 3° view angle detector is used for detection of faint sources.

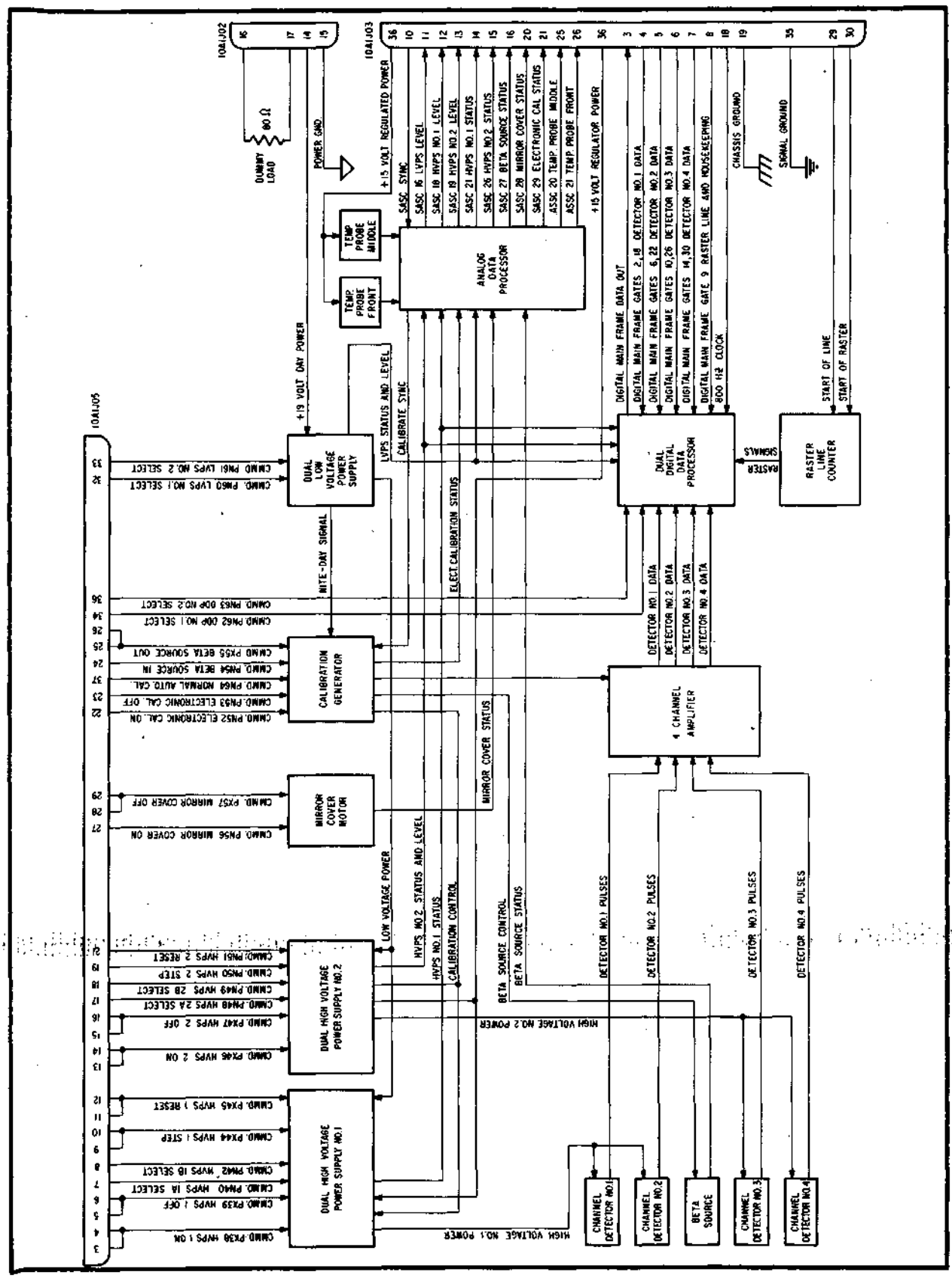

Figure 3-17 Functional Block Diagram for NRL-WL and XUV Coronagraphs

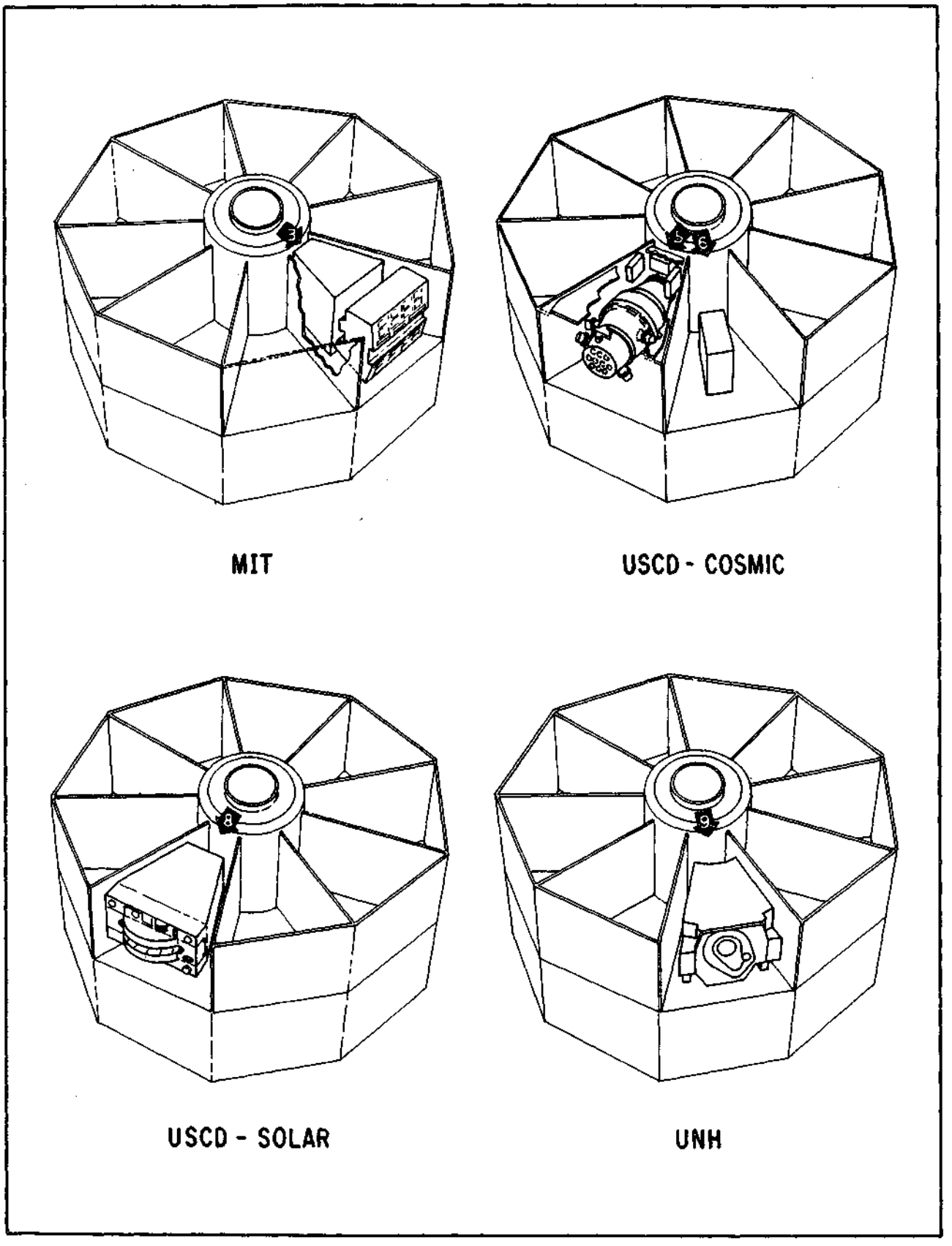

Figure 3-18 OSO-7 Wheel Instrument Payload

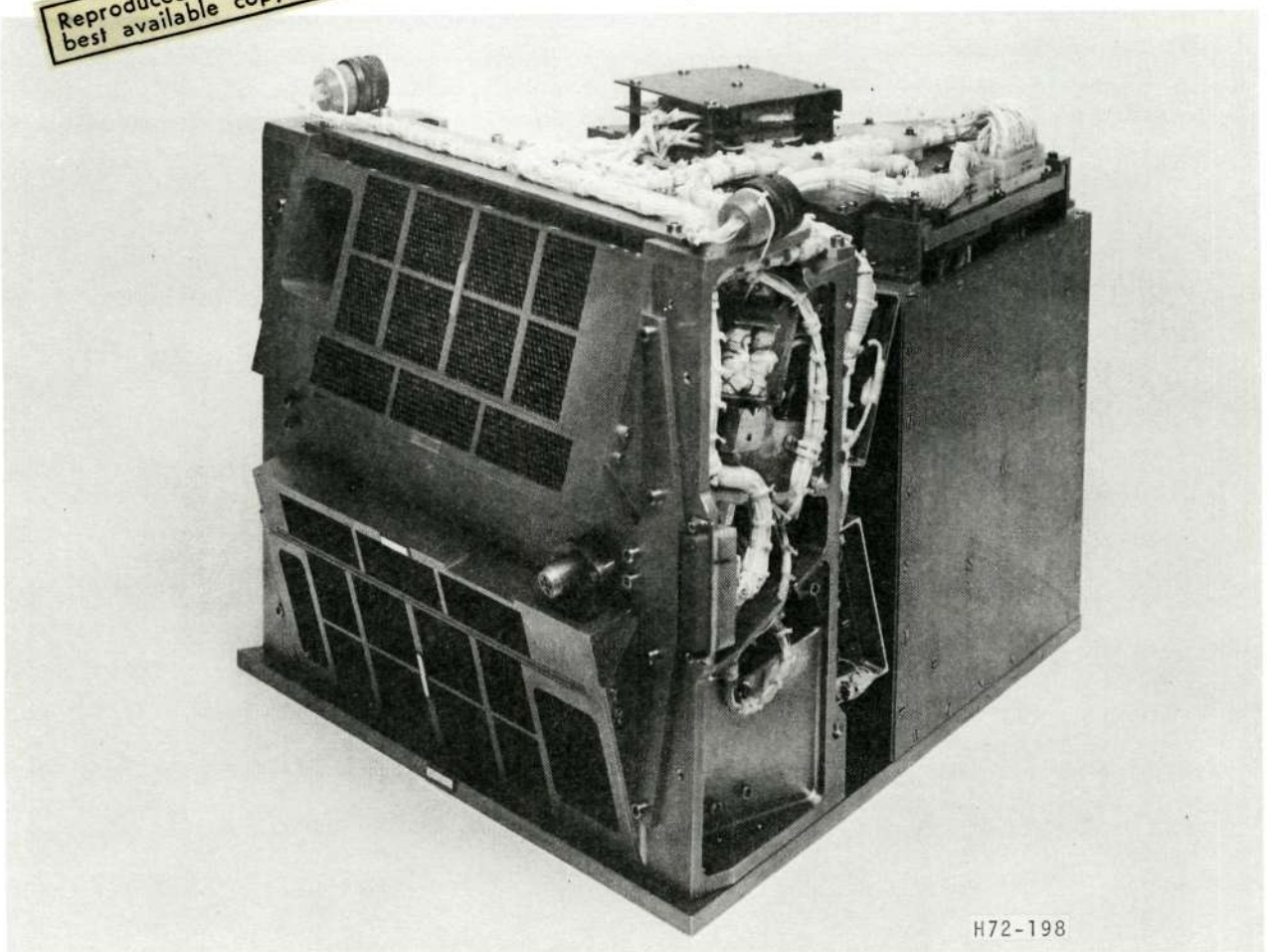

Figure 3-19 MIT-Celestial X-Ray Telescope

The sensitive axes of the detectors sweep out two celestial circles each wheel revolution, which results in nearly total celestial sphere coverage within six months (with the wheel plane perpendicular to the ecliptic plane the observatory must pitch approximately 1° per day to maintain the same relative solar vector). The instrument has a built-in safety feature to automatically turn the detectors off when source strength is high enough to cause detector degradation. The instrument also has its own radioactive source for periodic complete system calibration. The instrument internally divides wheel rotation in 256 increments (data "bins") during the nominal 2-second wheel rotation. However, sources can be pinpointed to ±0.1° by using statistical analysis (owing to slow observatory pitch rate), which is equal to the accuracy of the wheel aspect system.

Each detector assembly is made up of an integrated four-chamber counter, a single-chamber counter, and a collimator. Each counter is a gas-filled metallic chamber with a 1 to 3 kV potential from the wall to the center conductor. X-rays ionize the gas and cause sharp current pulses. The single-chamber counter has a very thin window for the lower energy response. The collimators are hexagonal arrays of closely packed cylindrical tubes, one array having tubes of 1° conical view and the other array having tubes of 3° conical view.

Figure 3-20 is a block diagram of the MIT instrument.

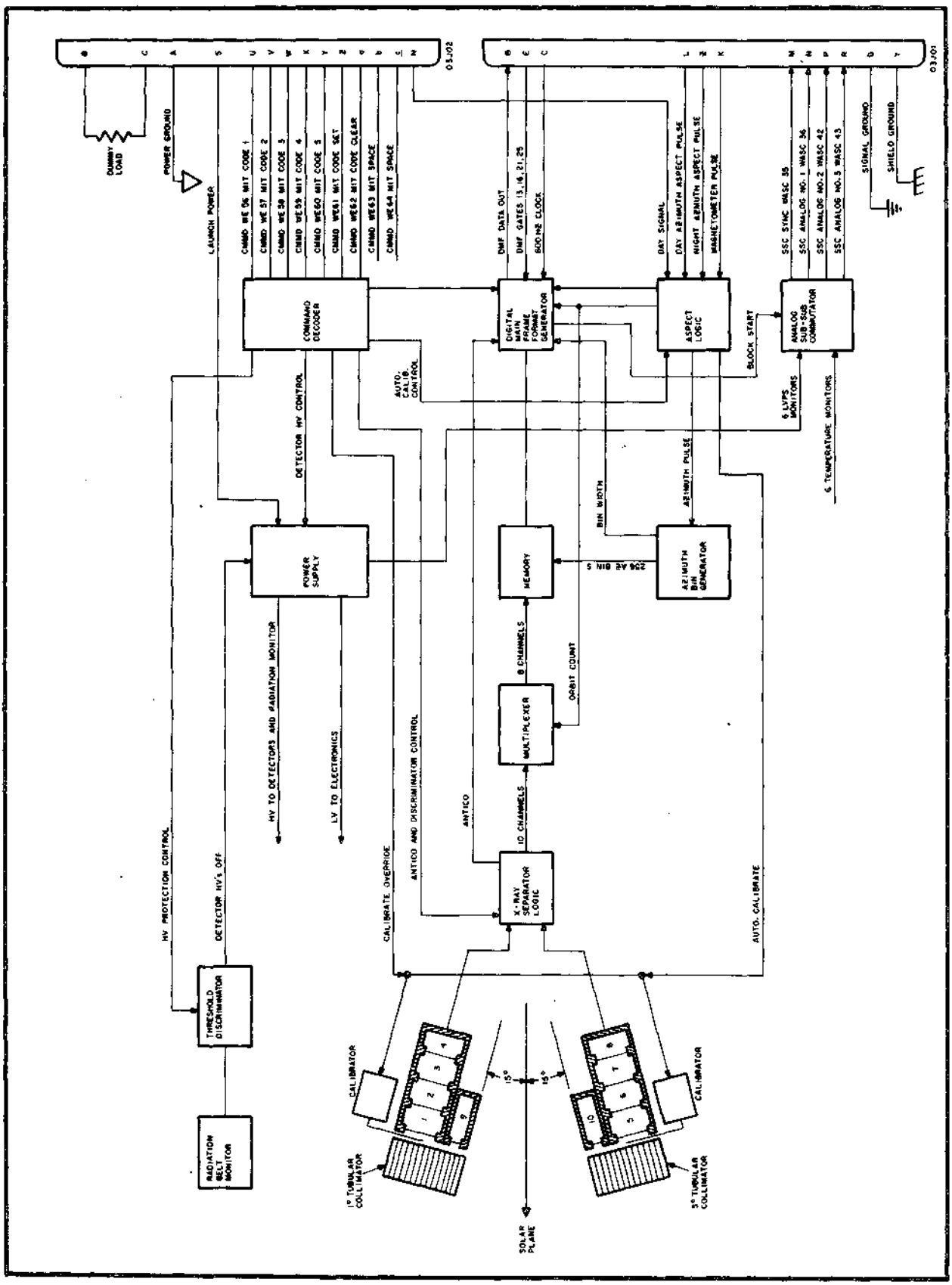

Figure 3-20 Functional Block Diagram for MIT-Celestial X-Ray Telescope

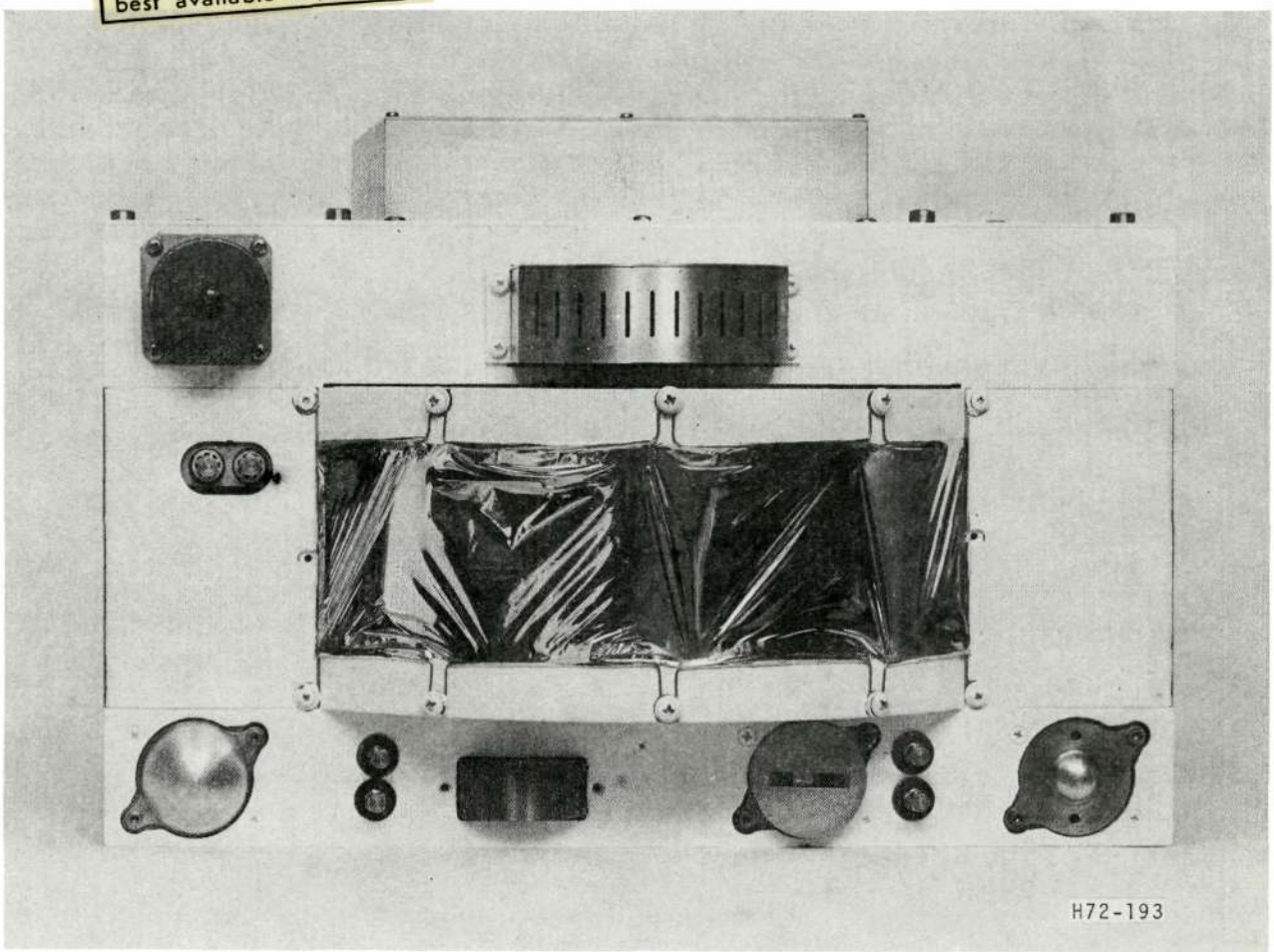

Figure 3-23 UCSD Solar X-Ray Telescope

evaluate X-ray detector background counts, one being sun gated for 90° azimuth field of view and the other two having continuous data integration periods. The hard X-ray sodium iodide detector has a built-in radioactive calibration source for checking the data system. The proportional counter, having a life limited by the total number of counts it produces, is automatically turned off (by a signal from one of the solid-state detectors) when the observatory passes through the earth's inner radiation belt.

Figure 3-24 is a functional block diagram of the instrument.

3.3.4 University of New Hampshire Gamma Ray Spectrometer

The primary objective of the UNH instrument (Figure 3-25) is to monitor the solar high energy photon spectrum from 0.3 to 9.1 MeV with respect to intensity and time variation. The instrument, in combination with the observatory telemetry system, must have sufficient resolution so that specific line spectra can be observed. For this reason, a 377-channel pulse height analyzer is used with the photon count in each of the 377 discrete channels being the primary instrument data. Also, neutrons from 10 to 40 MeV are identified by

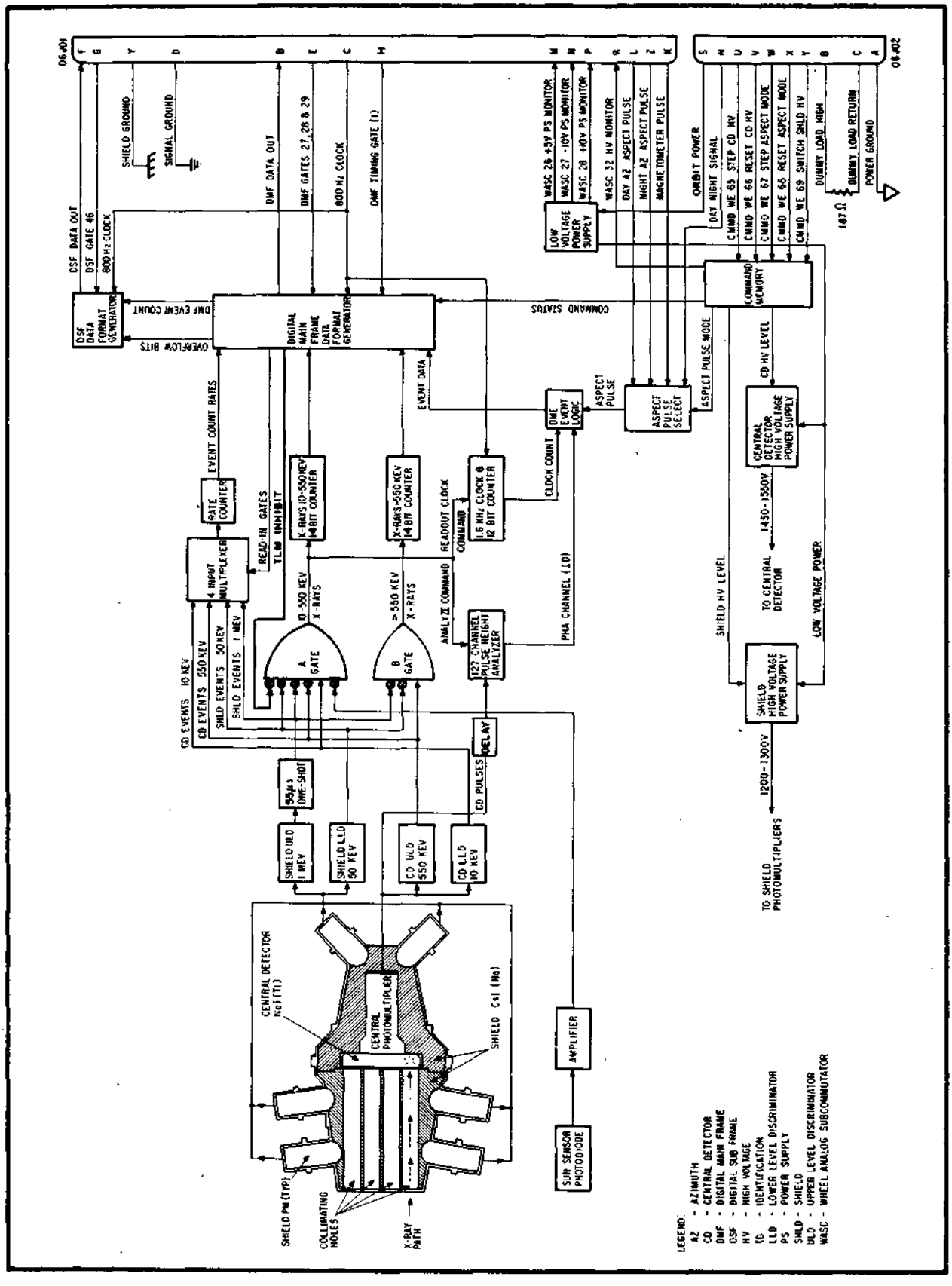

Figure 3-22 Functional Block Diagram for UCSD-Cosmic X-Ray Telescope

A solar sensor with a view angle of ±6° from the detector optical axis enables solar X-rays to be inhibited from the event analyzing electronics, as they would cause saturation. The instrument derives wheel aspect from a 1600 Hz clock, which divides a nominal wheel revolution into 3200 increments. Detected X-rays are referenced to this clock, which in turn is referenced to the observatory aspect system. Statistical analysis enables the source to be located within ±0.2°. The prime experiment data, which is single photon energy and aspect information, is limited to 3.12 events per second. The instrument also monitors total events in wide energy ranges, which, because background radiation is quite stable, will detect actual system performance, degradation, and settings.

The X-ray detector is a 4 inch diameter by 0.37 inch thick thallium-activated sodium iodide scintillation crystal which is viewed by a 3 inch photomultiplier. The detector is surrounded by a thick sodium-activated cesium iodide scintillation crystal shield with ten holes bored through it along the optical axis. The shield scintillator is viewed by six 1.5 inch photomultipliers. Light pulses in the detector crystal are caused by X-rays passing through the ten shield openings. These light pulses have relatively slow rise times and intensities proportional to the photon energy. The corresponding proportional current pulses out of the detector's photomultiplier are recognized as valid photon events and are processed by the experiment data system. X-rays or particles passing through the shield crystal cause light pulses with fast rise times and corresponding pulses in the shield's photomultiplier. Pulses from the shield's photomultiplier are used to electronically reject simultaneous pulses from the detector's photomultiplier, thereby ensuring data processing of only those X-rays passing through the ten collimating holes.

Figure 3-22 is a functional block diagram of the instrument.

3.3.3 UCSD - Solar X-Ray Telescope

The UCSD - Solar instrument (Figure 3-23) measures solar X-ray flux from 1.4 to 300 keV with good spectral, intensity, and time resolutions. Two detectors are used and the spectrum is resolved by 17 logarithmically spaced pulse height analyzer energy channels. A thallium-activated sodium iodide scintillating crystal detector is used for hard X-rays from 10 to 300 keV and a proportional counter is used for the soft X-rays from 1.4 to 10 keV. Counts from each of the energy channels are accumulated and read out into the observatory telemetry system in periods of 10.24 seconds. The intensity range on each of the 17 channels is from 0 to 65,536 which is resolved into 0 to 255 telemetry counts.

Both detectors have collimated look angles of ±45° in azimuth and ±10° in elevation. The sodium iodide detector is collimated by a cesium iodide anticoincidence shield and the gas-filled proportional counter has a passive metallic collimator. The wide look angles provide maximum sun exposure while cutting off outside exposure. A silicon photovoltaic cell, shielded by an assembly of twelve slits, is used as a sun gate sensor. It provides from a 90° data read-in (0.50 sec nominally) to a 8.2° data read-in (0.045 sec nominally) per wheel revolution. The latter accommodates any high count rate periods. The X-ray detectors are supplemented by three solid-state detectors that are filtered to respond to high energy charged particles (electrons and protons from 100 keV to 54 MeV). These are analyzed to

3.3.2 UCSD - Cosmic X-Ray Telescope

The objectives of the UCSD cosmic instrument (Figure 3-21) include precise location of known cosmic X-ray sources, detection of new sources, measuring the intensity of all sources, and most important, the spectral analysis of these sources from 10 to 550 keV. The sensitivity of detection is 5×10^{-4} photon/cm^2-sec which is close to the celestial background of 2×10^{-4} photon/cm^2-sec in this energy range. The 10 to 550 keV energy range of the instrument is spectrally resolved by a 128 channel spectrum analyzer (pulse height analyzer).

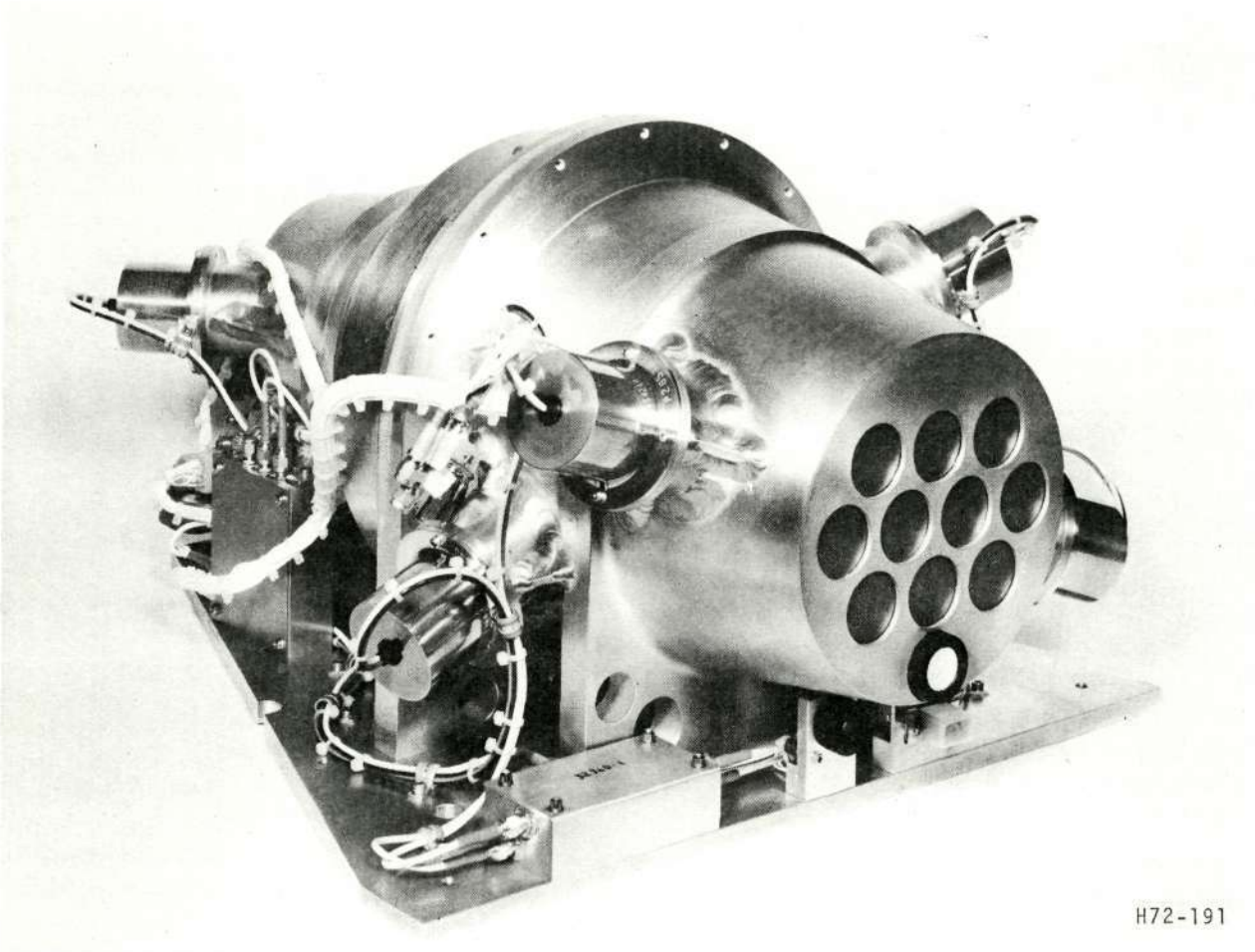

Figure 3-21 UCSD-Cosmic X-Ray Telescope

The instrument's highly sensitive X-ray detector views radially from the wheel in a ±3.2° cone angle about its optical axis. The sensitive axis sweeps out a celestial circle each wheel revolution which results in nearly total celestial sphere coverage within six months.

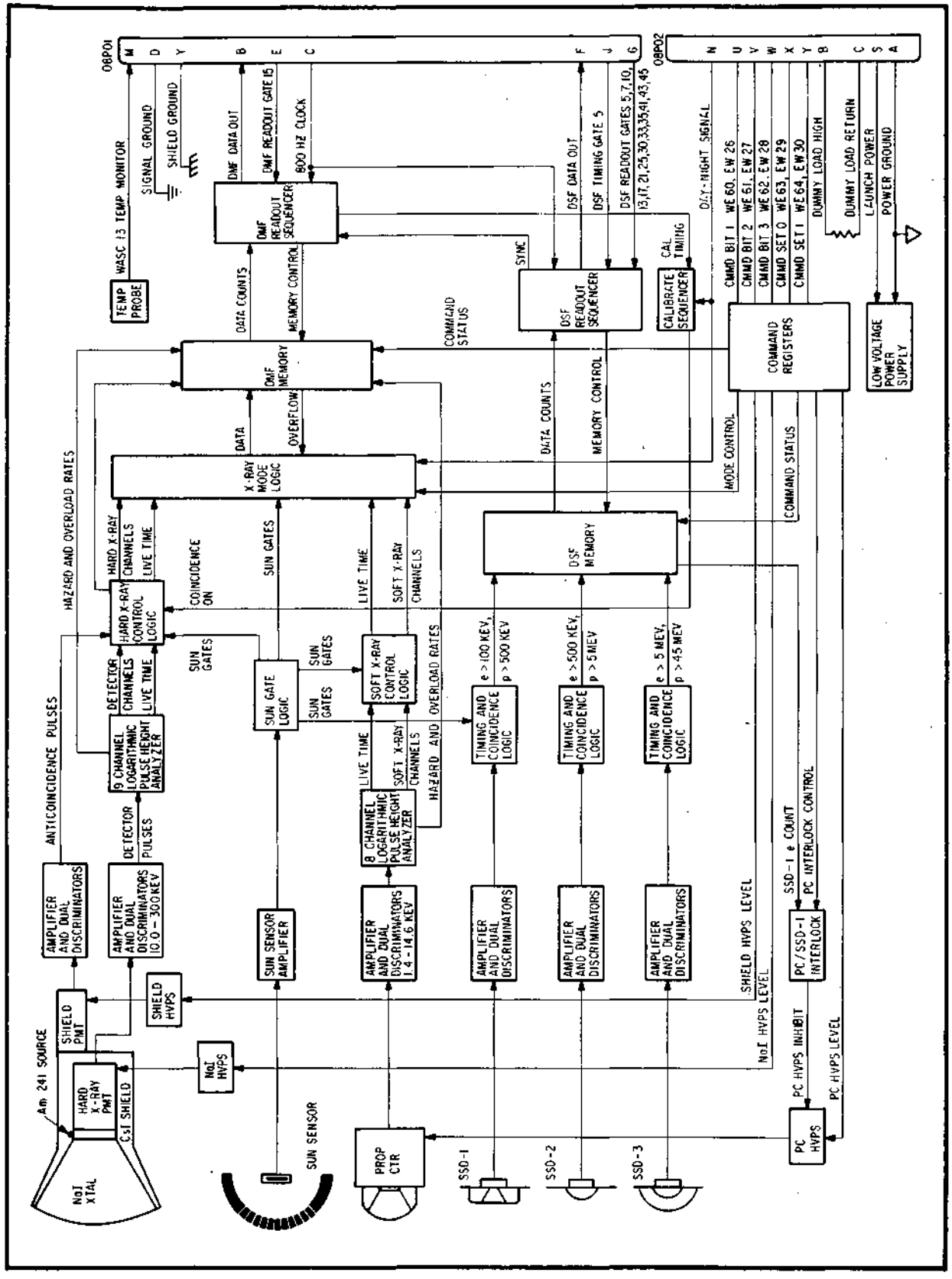

Figure 3-24 Functional Block Diagram for UCSD Solar X-Ray Telescope

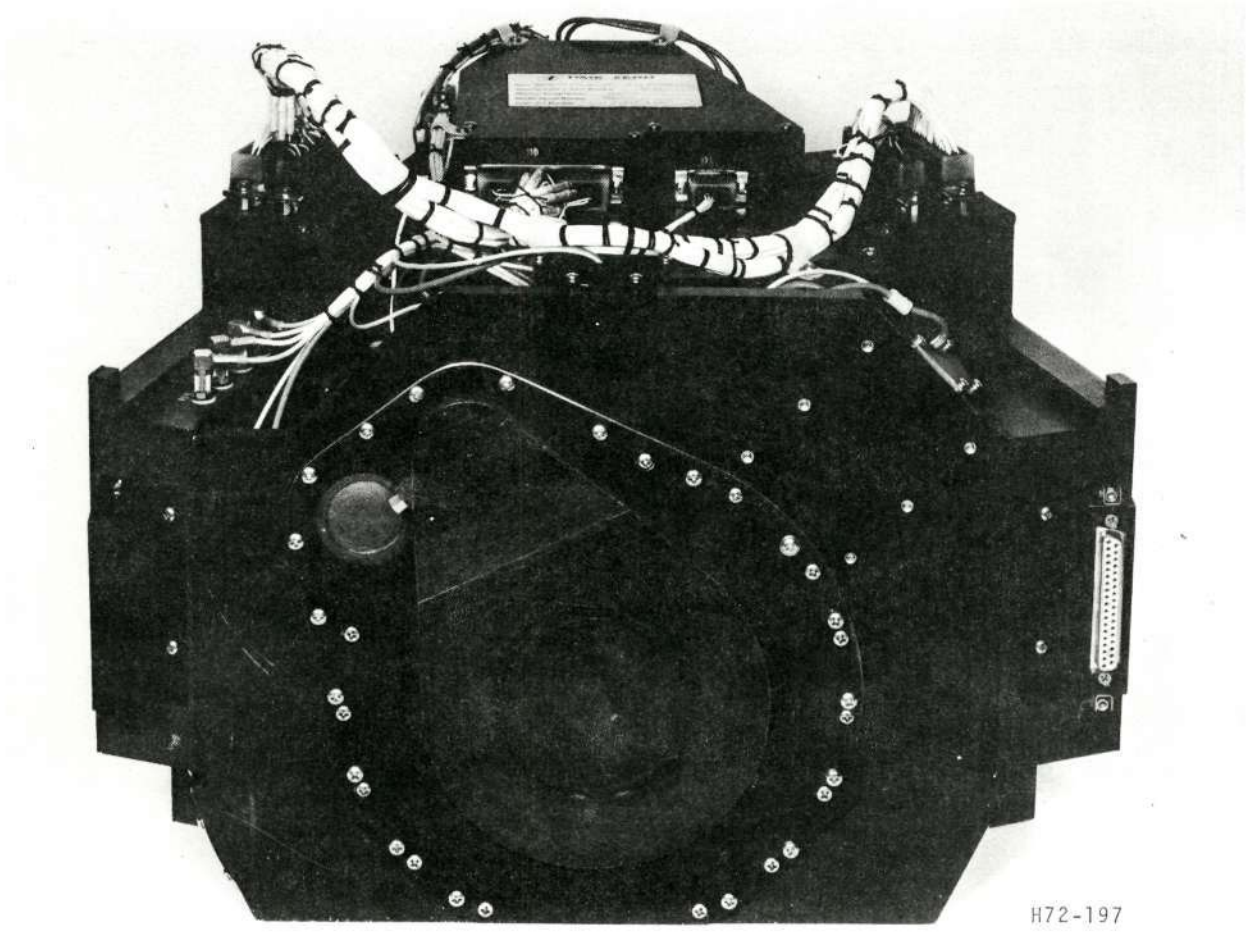

Figure 3-25 University of New Hampshire Gamma Ray Spectrometer

pulse-shape analysis and are spectrally analyzed by a three-channel pulse height analyzer. For correlation purposes in the data analysis, a secondary system detects X-rays from 7.5 to 120 keV using a four-channel pulse height analyzer.

Although primary interest is in solar direction monitoring, the instrument has a "quadrant generator" to provide four 90° data-in gates per wheel revolution. The instrument uses the observatory's day solar-sensor azimuth aspect pulse and the night gyro azimuth aspect pulse (or the night magnetometer pulse) to trigger the quadrant generator. The primary mode is to take data in the solar and anti-solar quadrant each wheel revolution, with the anti-solar direction providing basically background correlation. However, an alternate mode may be used where the two quadrants perpendicular to the solar direction are used as data-in gates. Normally the instrument processes all 377 gamma-ray channels in approximately three minutes. By discarding some channel data, better time resolution is possible on the remaining channels of interest. The instrument has built-in gamma-ray and X-ray calibration sources and an injectable electrical pulse for checking the data processing of the detector pulses.

Celestially, the instrument will be studying earth albedo gamma rays and electron bremsstrahlung. The UNH data analysis will be instrumental in determining the future direction of detector development for solar and celestial gamma-ray research astronomy.

The instrument incorporates a sodium iodide scintillating crystal viewed by a photomultiplier and a cesium iodide anticoincidence shield viewed by additional photomultipliers. The X-ray detector also uses a thin, collimated sodium iodide scintillating crystal viewed by a photomultiplier.

Figure 3-26 is a functional block diagram of the UNH gamma-ray instrument.

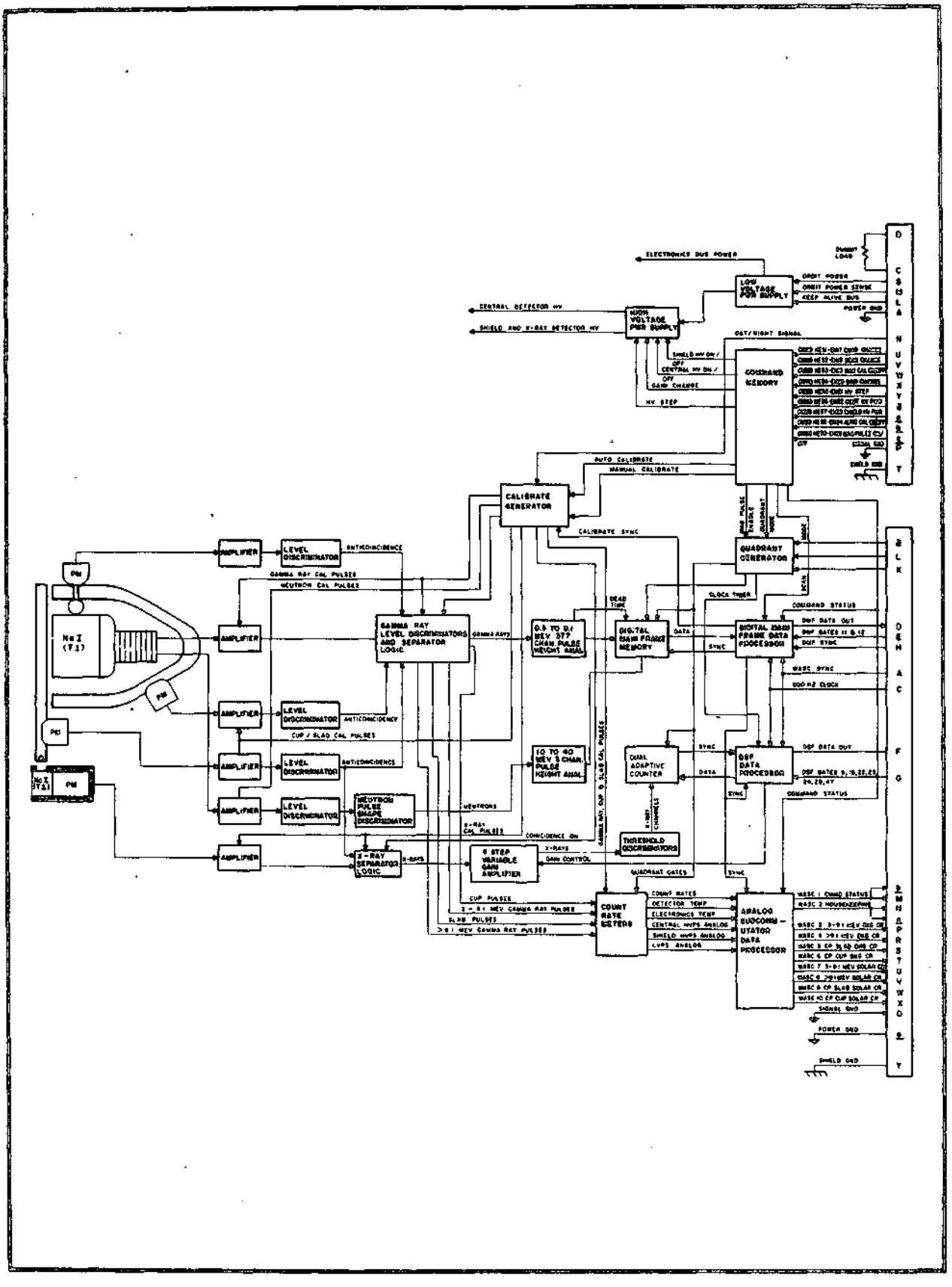

Figure 3-26 Functional Block Diagram for University of New Hampshire Gamma-Ray Spectrometer

Section 4
OBSERVATORY OPERATION AND PERFORMANCE FROM LAUNCH SEQUENCE THROUGH ONE YEAR IN ORBIT

4.1 LAUNCH PHASE PERFORMANCE

Final prelaunch preparations took place on the morning of September 29, 1971, and the vehicle was prepared for a liftoff at 0945 GMT. Data from the spacecraft was received at the Orbiting Solar Observatory Operation Control Center (OSO OCC) prior to liftoff; the status of the spacecraft was as listed below:

Spin Gas Pressure - 2952 psi

Pitch Gas Pressure - 2931 psi

Battery Voltage - 19.1 Vdc

Spacecraft Load Current - 0.76 amps

Tape Recorders - both on and recording in manual mode

Temperatures - Between 21.6°C (despin drive) and 24.8°C (compt. #4 deck)

Gyro Power - OFF

Spin - Manual

Pitch - Manual

Solar Panels - Enabled

Dummy Loads - OFF

Undervoltage Turn-On Disabled

SORE Alternate - Encoder Enabled

The launch sequence did not proceed as planned due to a vehicle second-stage malfunction. However, the mission was saved by execution of several phases of a detailed launch sequence contingency plan that had been perfected prior to launch. The contingency plan basically covered the appropriate instantaneous corrective action (spacecraft command sequences) required to recover from a variety of abnormal spacecraft conditions. The contingency plans had been tested and perfected by numerous computer dynamic simulations.

4.1.1 The Intended Versus Actual Launch Sequence of OSO-7

Intended OSO-7 Launch Sequence. The intended spacecraft launch sequence events are shown in the upper trace of Figure 4-1. When the vehicle fairing is ejected, the spacecraft azimuth servo is energized and placed in a mode which spins up the sail to about 40 rpm. The sail continues to spin through the coast phase, second stage restart, and orbit injection.

After the second-stage restart is terminated, the spacecraft is separated from the launch vehicle. The angular momentum of the spinning sail stabilizes the spacecraft against normal tip-off rates occurring during separation.

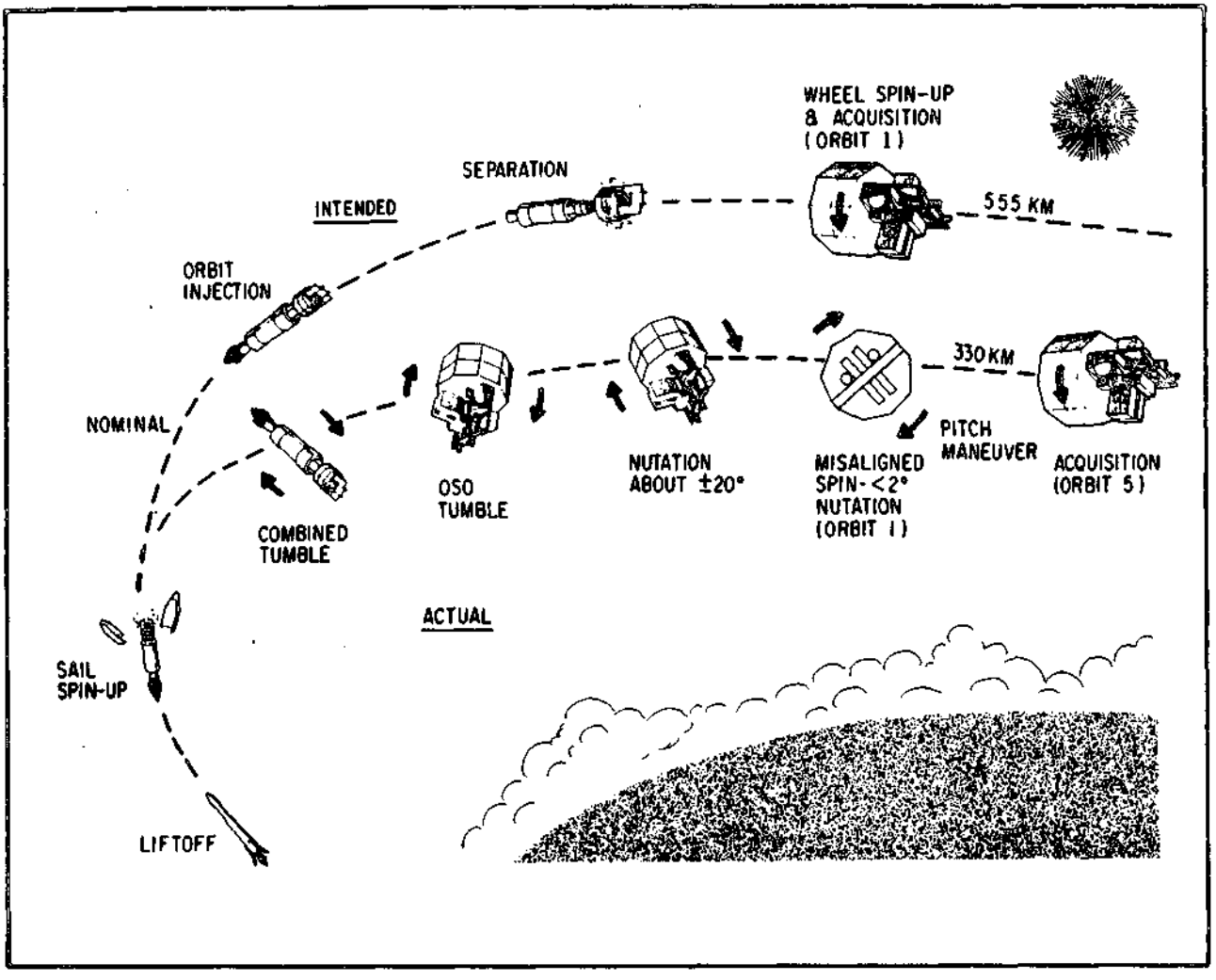

Figure 4-1 Intended Versus Actual Launch Sequence of OSO-7

When the spacecraft is separated from the launch vehicle, the injection attitude is controlled so that the spin axis is perpendicular to the line-of-sight of the sun within 10 degrees. The azimuth servo is automatically switched to the sun-pointing mode and the sail begins to despin under control of the coarse azimuth solar sensors. Gas is also released from spin-up jets on the wheel for about 180 seconds to bring the wheel up to its normal operating spin rate of about 30 rpm. In the mean time, the sail has despun and acquired in azimuth and if the pitch axis is more than three degrees from perpendicular to the line-of-sight to the sun, the automatic pitch system precesses the spacecraft to reduce the pitch error.

Upon acquiring the sun in azimuth an on-target signal from a solar sensor releases the bob of the fluid-filled nutation damper and unlocks the elevation gimbal so that the pointed instruments are free to move under the control of the elevation servo.

Actual OSO-7 Launch Sequence. The actual launch sequence events for OSO-7 are shown in the lower trace of Figure 4-1. Lift-off, occurring at 9:45 GMT on September 29, 1971, was followed by completely normal vehicle and spacecraft behavior through the boost phase, fairing ejection, sail spinup, and the coast phase. Table 4-1 lists actual launch sequence events.

Table 4-1
ACTUAL LAUNCH EVENTS

ORBIT "Q"

094500.86Z	Lift Off OSO-OCC receiving data from Ft. Myers.
094855.5Z	Fairing ejection and sail spin-up. The sail spin rate increased to 24.3 rpm.
095003Z	Antigua AOS Data was of poor quality and the OSO-OCC could not obtain PCM lock throughout the pass.
095515Z	Ft. Myers LOS
100226Z	Antigua LOS
100330Z	Ascension AOS Data received indicated the sail spin rate had increased to 42.9 rpm.
101330.4Z	Telemetry detection of 2nd stage restart. After 2nd stage burn was completed, the relative spin rate between the wheel and sail decreased to Ø rpm. Azimuth motor current increased from 0.2 amps to 0.78 amps, indicating motor was attempting to increase sail spin rate.
101602Z	Joburg AOS
101716Z	Ascension LOS
101822.4Z	Telemetry detection of separation from the launch vehicle. Spin rate could not be determined from telemetry data. AGC reading at ground station indicated wheel spin rate was approximately 63 rpm.
102025.3Z	First reading of large angle pitch readout. Readout indicated +11° pitch.
102111.4Z	Spin gas stopped depleting. 500 psi of gas was used. The pitch readout continued to increase until a reading of +85°.

Soon after the second-stage engine was reignited to provide thrust to achieve orbital velocity, a vehicle malfunction caused the second stage to begin tumbling. At the completion of the second-stage burn the tumble rate was about 55 rpm.

The longitudinal acceleration at the spacecraft due to the tumbling motion was about 8 g's, increasing the axial thrust loading on the spacecraft azimuth shaft bearing to about 3600 pounds. The acceleration lasted more than 16 seconds, compared to a nominal period of 7 seconds. The spinning sail, constrained from precessing by the much larger angular momentum of the vehicle, came to a stop within a few seconds. The sail spinup circuits delivered full drive current to the azimuth motor in an attempt to increase the sail-to-wheel spin rate to a normal value.

After completion of the second stage restart burn, the roll control system on the booster continued to function and maintained the vehicle roll (motion about the longitudinal axis) rate near zero. Therefore, the spacecraft-vehicle rotated about a vehicle transverse axis with very little nutation.

4.1.2 Separation Dynamics of OSO-7

The dynamic motion of the spacecraft immediately following separation from the vehicle occurred in two phases. During the first phase, the spacecraft began tumbling about a transverse axis through its center of mass. Simultaneously, gas was automatically released from the spinup jets on the wheel, changing the momentum of the system and partially erecting the spacecraft. In the second phase, spinup torques were no longer present, and the orientation of the total angular momentum vector remained essentially constant. The elevation caging was released and the nutation began to decay as energy was dissipated by the elevation gimbal suspension.

Spin torques applied about the axis of the wheel produce widely varying attitude motion depending on the orientation of the original tumble axis relative to the transverse principal inertial axes, and the relative difference (asymmetry) between the transverse moments of inertia.

While spinup torques are applied, the wheel does not rotate appreciably about its axis of maximum moment of inertia (spin axis). Instead it oscillates through a fraction of a revolution. This explains the absence of data from the pitch angle solar sensor during most of the wheel spinup period, as shown in Figure 4-2.

When spinup torques ceased, the spacecraft motion approximated that of a disk-shaped body, rotating with large nutation. Data from the pitch attitude sensor are shown on the upper right of Figure 4-2. By the next station pass, about 1-1/2 hours later, the spacecraft was spinning about its normal spin axis and the nutation half-angle was about one degree. The pitch attitude relative to the sun was 71 degrees, indicating that the angular momentum vector was about 19 degrees from the antisolar direction.

When the spacecraft is in a pure tumble about a transverse axis, the line of sight to the sun traces out a cone, with half-angle of 19 degrees, centered about the tumble axis. As the nutation angle decreases, the sun cone intersects the sensor readout plane at different

pitch angles. The pitch readout sensor will generate data only when the wheel azimuth position is such that the sensor field of view plane intersects the sun cone; this occurs when $|\phi|$ <19 degrees.

The attitude sensor geometry and the relationship between the angular momentum vector and the line of sight to the sun restrict the pitch readout angles to those shown in Figure 4-3.

Using this graph to interpret the pitch-angle data in the upper right part of Figure 4-2, reveals that the spacecraft became partially erected during the few minutes following separation, and the nutation half-angle was reduced to less than 20 degrees.

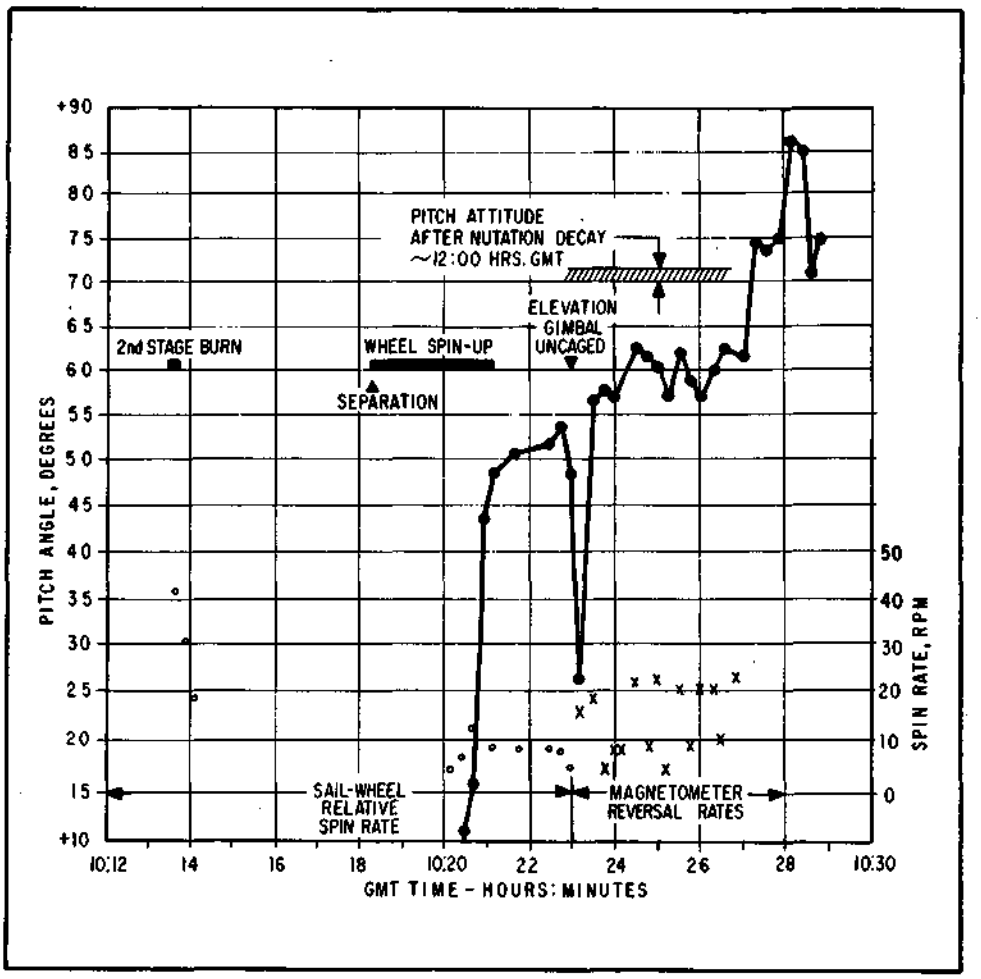

Figure 4-2 Pitch Attitude and Spin Rate Data

4.1.3 Recovery of OSO-7

The telemetry data, spacecraft modes and the command groups transmitted during the recovery operation are indicated on Figure 4-4. Two additional orbital revolutions, for which data are not shown, were used to return the spin rate to normal and place the spacecraft in a normal operating mode.

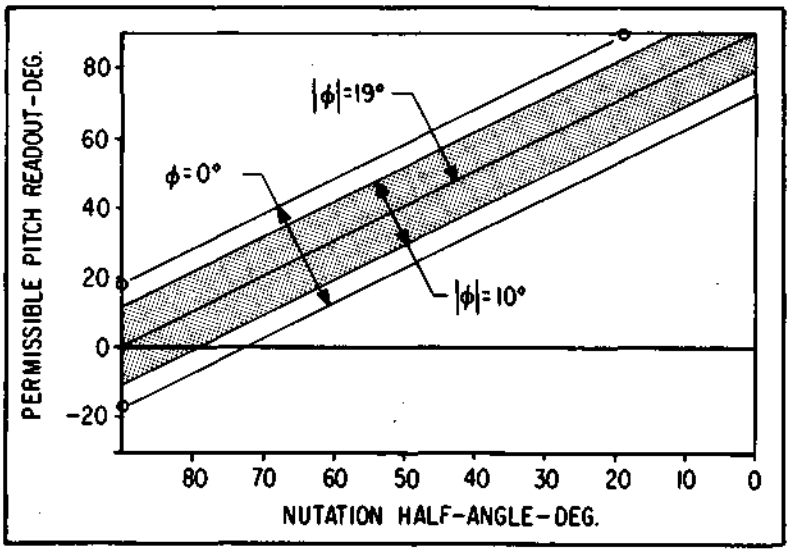

Figure 4-3 Permissible Pitch Attitude Readout-Momentum Vector 19 Degrees from Line of Sight to Sun

Command groups were executed at the field stations by use of previously

prepared paper tapes in accordance with instructions from the spacecraft control center. During some station contacts it was necessary to supplement the prepunched command tapes with additional commands, relayed to the field stations by voice communications.

As shown in Figure 4-4, the spacecraft load current reflects the additional current drawn by the azimuth servo during sail spinup and initial attempts at acquisition after separation while the spin axis was still broadside to the sun. Other fluctuations in the load current are due to bus voltage variations caused by current developed by the array as it occasionally viewed the sun or earth and by solenoid energizing current during gas expulsion.

The state of battery charge is indicated roughly by the bus voltage, which had declined to about 17 volts by orbit 4. This corresponds to about 75 percent discharge of the battery. While sufficient energy remained for one or two more orbital revolutions, operation below 16.8 volts could have resulted in undervoltage disconnect during current surges such as that accompanying azimuth acquisition.

The azimuth motor current, shown in the lower trace of Figure 4-4 reflects the action of the azimuth drive servo. The decaying current, during orbit Revolution 0, reflects the decrease in motor current as the sail comes up to terminal velocity. The increased drive current during Revolution 1 accompanied sail despin under gyro control. With the sail stopped, the normal level of azimuth motor current is shown in Revolutions 2, 3 and 4 (gyro control) and in Revolution 5 after normal solar acquisition.

The other traces on Figure 4-4 display the spin and pitch gas supply pressures which varied slightly from changes in reservoir temperatures and declined from an initial pressure of about 3000 psi as acquisition maneuvers were executed. At the beginning of normal orbital operations the spin and pitch gas pressures were 1540 and 2200 psi respectively.

Other telemetry data were used indirectly to confirm the spacecraft attitude. The incidence of the sun on the underneath side of the wheel introduced a substantial temperature gradient along the spin axis of the spacecraft. The temperature of the antenna skirt, located on the lower rim of the wheel, rose above 78°C compared with a normal temperature of about 25°C. The case temperature of the azimuth gyro, located in the sail, fell below -15°C, compared to a normal minimum temperature of 0°C.

These temperatures caused no permanent damage; however, the gyro gain was reduced to the point where azimuth acquisition was slowed. Excessive gyro drift caused changes in the sail position making it necessary to release test bursts and determine sail position on each station pass.

Recovery operations through the first six orbit revolutions are summarized below:

Revolution 0 - *Johannesburg* - Sent commands in accordance with contingency logic to (1) release elevation axis and nutation damper caging, providing mechanisms to damp nutation if present, (2) enable determination of spin rate from magnetometer data, (3) begin despin toward 9 rpm, (4) power-down spacecraft.

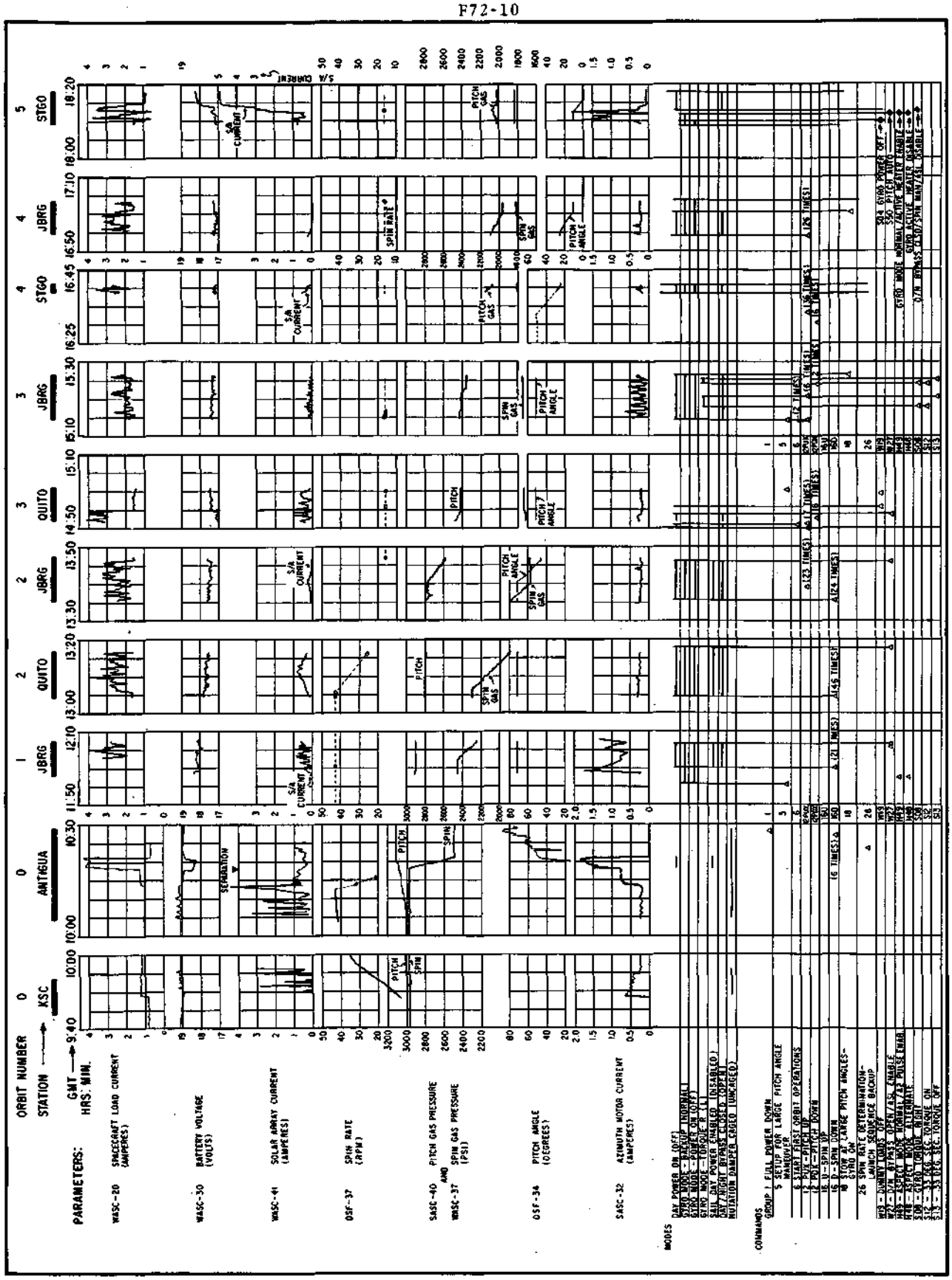

Figure 4-4 Telemetry Data, Modes, and Corrective Commands

Revolution 1 - *Guam* - Readout housekeeping data. Spin rate tentatively determined to be 43.5 rpm. (Data not shown on Figure 4-4.)

Ft. Myers - Repeated commands to (1) release nutation damper and elevation caging, (2) spinup (4 bursts) spacecraft slightly to observe and confirm spin rate, (3) stow spacecraft in power-down condition. Pitch angle read out +71 degrees. (Data not shown in Figure 4-4.)

Johannesburg - Sent commands to (1) set up for large angle pitch maneuver (turn on gyro), (2) sent 21 spindown bursts to make pitch maneuvers easier. Spin rate with sail stopped reduced from 60 rpm to 46 rpm.

Revolution 2 - *Santiago* - Sent 47 more spindown bursts, reducing spin rate to 26.6 rpm.

Johannesburg - Sent 24 spindown bursts, reducing spin rate to about 15 rpm. Sent 22 pitch-up bursts reducing pitch angle from 71 degrees to 47 degrees.

Revolution 3 - *Quito* - Sent 5 pitch-up bursts. Pitch angle increased to 53 degrees because gyro had drifted so sail was in wrong position. Erroneously sent command group placing spacecraft in sun-pointing mode, which allowed sail to rotate. Sent 6 pitch-up and 12 pitchdown bursts. No net effect on pitch angle because sail was rotating.

Santiago - Sent commands to place gyro in control.

Johannesburg - Sent 3 pitch-up bursts to test for direction and sail position. Slewed 60 degrees right. Sent 6 pitch-up bursts. No appreciable effort. Slewed 40 degrees right to improve sail position. Sent 2 pitchdown bursts to confirm sail position and direction. Stowed spacecraft with gyro on.

Revolution 4 - *Santiago* - Sent 6 pitch-down bursts increasing pitch angle. Sent 36 pitch-up bursts decreasing pitch angle to 26 degrees.

Johannesburg - Sent 26 pitch-up bursts, reducing pitch angle to 12 degrees. Stowed spacecraft in minimum power configuration (gyro on).

Revolution 5 - *Santiago* - Enabled sun-pointing mode by turning gyro off. Enabled auto-pitch mode. Pitch angle reduced to -1 degree automatically. Pointing system acquired sun.

Revolution 6 - *Santiago* - Sent 18 spin-up bursts, increasing spin rate from 15.6 to 24 rpm. Opened day/night bypass. Fired experiment deployment squibs. High and low dummy loads ON.

On subsequent orbits, spin control was switched to the automatic system and the wheel rate increased in a normal fashion to 26 rpm. When attempts were made to play back the onboard tape recorders and retrieve stored data, only one of the two redundant recorders responded. It is assumed the second recorder was damaged by the accelerations experienced during the launch sequence. All scientific experiments operated normally.

Orbital operation has continued for 14 months (as of November 29, 1972). The vehicle malfunction resulted in an orbit with apogee altitude of 310 nautical miles and perigee altitude of 178 nautical miles instead of the 300-nautical-mile circular orbit normally used. This has had no effect on the performance of the spacecraft. However, orbital decay may end the operation life about three years after launch.

4.2 COMMAND STATISTICS THROUGH ONE YEAR IN ORBIT

The data handling and telemetry system continues to function normally after twelve months in orbit. The single surviving tape recorder has been operated continuously, with no evidence of degradation.

As of 1 October 1972, 120,503 commands had been transmitted. The length of pass time for sending commands is somewhat reduced when orbital perigee occurs over a ground station; in some cases, to lengthen the pass time, commands have been transmitted at elevation angles less than 10°, where the probability of missed commands increases.

Of the 120,503 commands transmitted, 119,293 (99%) were successfully executed. A total of 156 of the 1210 missed commands occurred at low elevation angles, making the execution ratio 99.1% at normal elevation angles. There has been no evidence of commands executed which were not transmitted (i.e., no spurious command responses).

Although command system performance has been excellent with no spurious commands received (a previous problem), the occasional missed commands have been a small problem for experimenters who depend upon a long sequence of commands for experiment mode set-ups. Repeat sequences have been necessary on occasion causing some loss of data during the time between repeat sequences.

4.3 DATA RECOVERY STATISTICS THROUGH ONE YEAR IN ORBIT

During the first year of orbital operation all but about 2.3 percent (190 hours) of the data were recovered. The main cause of lost data was the absence of the Lima, Peru station which left a gap in the data recovery pattern. If both spacecraft tape recorders had been operable, this difficulty would have been circumvented by using the recorders in the serial record mode.

About 13 hours of data (0.1 percent) were lost due to communications difficulties, operator errors, and conflict with higher priority activities.

4.4 SPIN AXIS ATTITUDE AND CELESTIAL POINTING

The observatory has been maneuvered during its first year in orbit to allow wheel instruments to scan essentially the entire celestial sphere. Figure 4-5 traces the spin axis attitude throughout the entire year in terms of its declination and right ascension angular coordinates in the celestial sphere. The attitude shown is along the spin axis as it leaves the top of the sail structure. Also, Figure 4-6 shows the observatory's roll angle orientation throughout the first year in orbit. Table 4-2 then summarizes several significant astronomical sources viewed by the various instruments, the associated calendar dates and the scientific instruments primarily used in monitoring along the associated source direction.

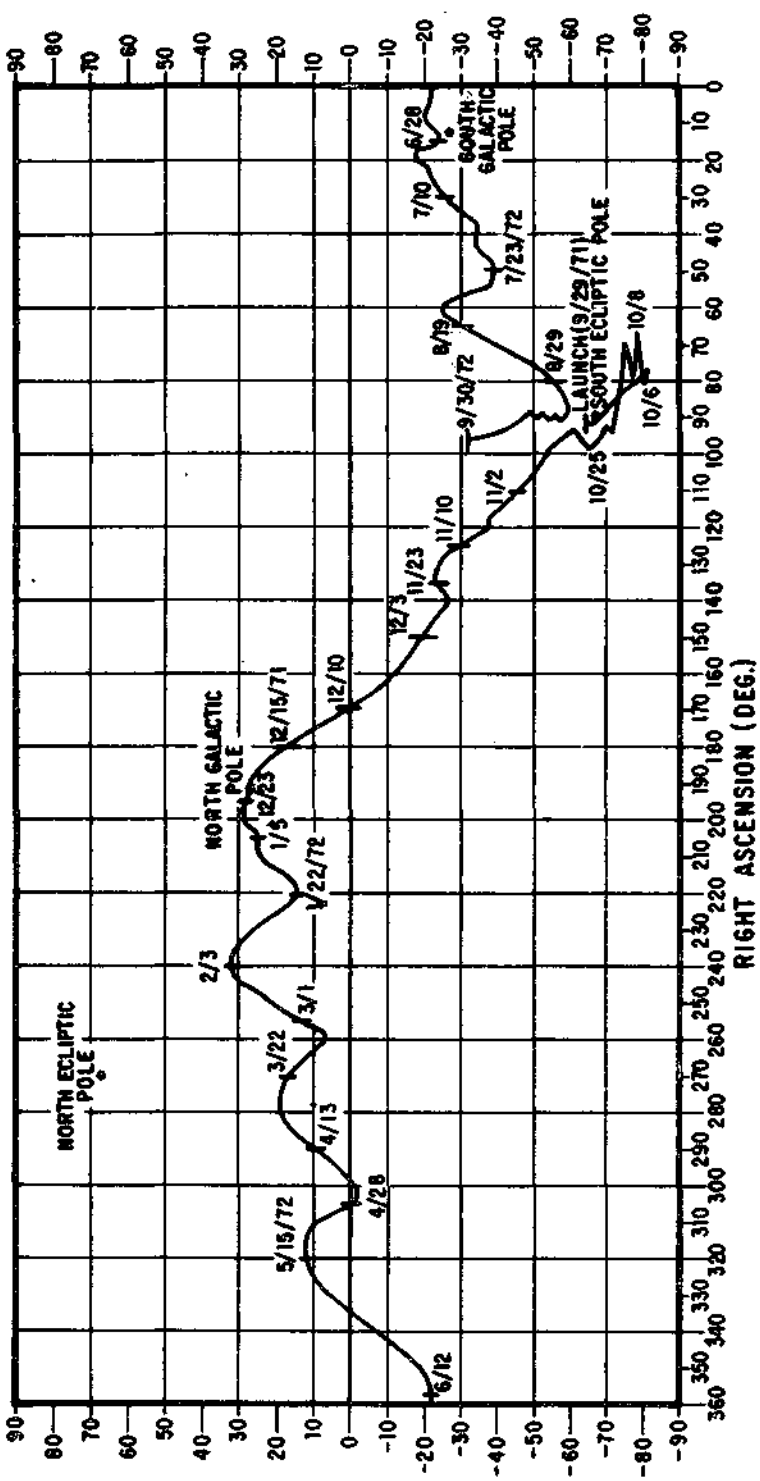

Figure 4-5 OSO-7 Spin Axis Attitude History

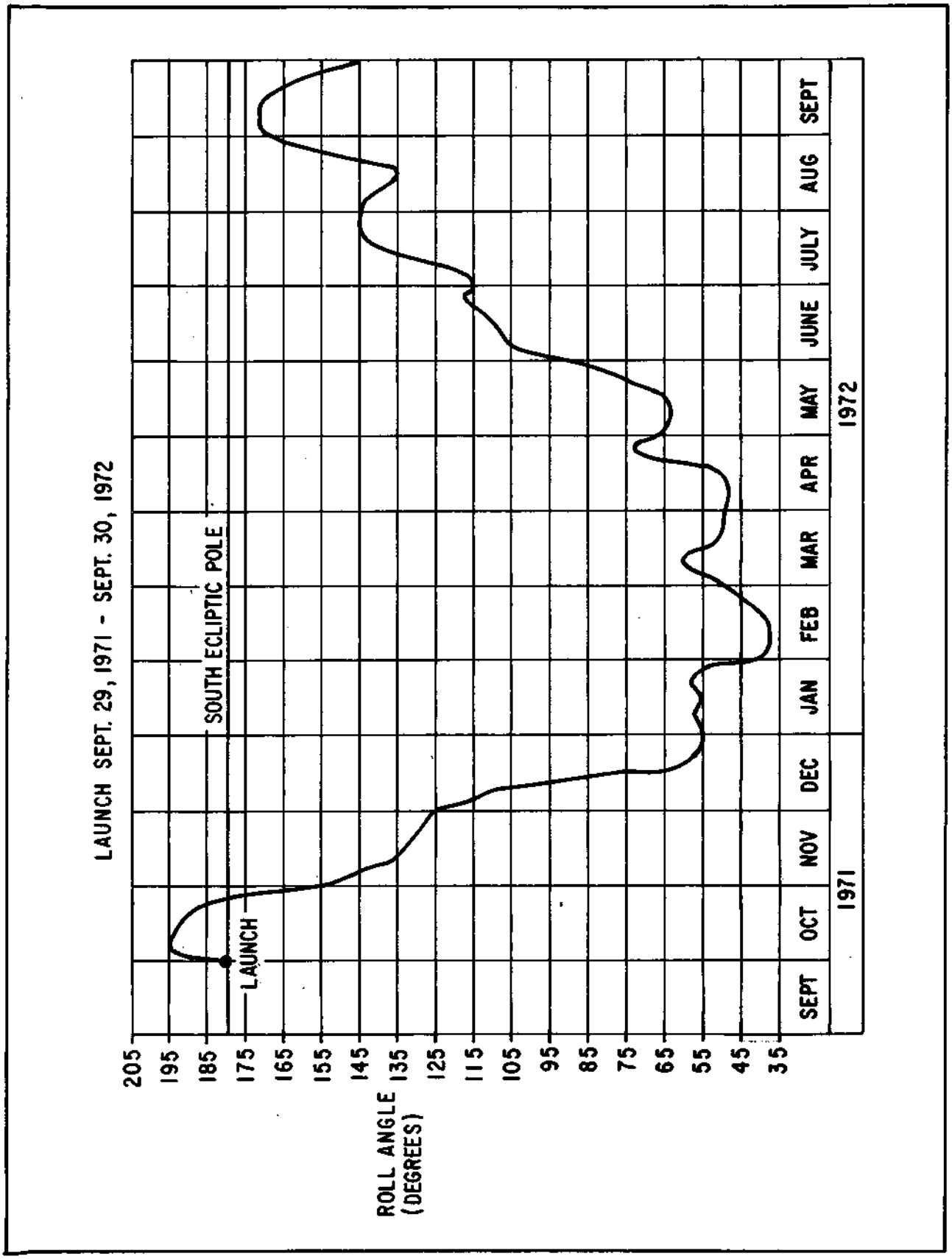

Figure 4-6 OSO-7 Roll Angle Orientation History

Table 4-2

SIGNIFICANT ASTRONOMICAL SOURCES VIEWED BY INSTRUMENTS THROUGH ONE YEAR IN ORBIT

Approximate Date	Astronomical Source Viewed (Primary Instrument)
Launch September 29, 1971	In Wheel Plane When Spin Axis Pointed at South Ecliptic Pole (Pointed)
October 28-November 20, 1971	SCO X-1 (MIT 105 deg.)
December 10, 1971	SMC (MIT 105 deg.)
December 13-14, 1971	CYG X-1 (MIT 105 deg.)
December 20, 1971	In Wheel Plane When Spin Axis Pointed at North Galactic Pole (UCSD-C and MIT)
January 7-11, 1972	Norma Nova (MIT 105 deg.)
January 10-19, 1972	CYG X-1 (MIT 75 deg.)
February 23-28, 1972	Cent XR-3 (MIT 105 deg.)
March 5-14, 1972	SMC (MIT 105 deg.)
March 15-20, 1972	Cent XR-3 (MIT 105 deg.)
April 24-27, 1972	Nova GX331+5 (MIT 75 deg.)
May 2-7, 1972	Perseus (UCSD-C)
May 10-12, 1972	SCO X-1 (MIT 75 deg.)
May 23-June 1, 1972	SCO X-1 (UCSD-C)
June 5-14, 1972	SCO X-1 (MIT 105 deg.)
June 21-24, 1972	CYG X-1 (UCSD-C)
June 19-30, 1972	In Wheel Plane When Spin Axis Pointed at South Galactic Pole
July 8-10, 1972	CYG X-2 (UCSD-C)
July 13-18, 1972	CYG X-1 (MIT 105 deg.)
August 19-25, 1972	Special Source (UCSD-C)
August 29-September 6, 1972	SCO X-1 (MIT 105 deg.)
August 29-September 19, 1972	In Wheel Plane When Spin Axis Pointed at South Ecliptic Pole (Pointed)
September 23-28, 1972	Perseus (UCSD-C)

NOTE: UCSD-C refers the UCSD-Cosmic X-Ray radially viewing wheel instrument, MIT 75 deg refers to the detector on the MIT Celestial X-Ray Telescope which views 15° above the wheel plane, MIT 105 deg refers to the detector on the MIT instrument which views 15° below the wheel plane, and pointed refers to the pointed instruments (primarily the NRL instrument) as being the primary monitor instruments.

Section 5
SPACECRAFT SUBSYSTEM PERFORMANCE THROUGH ONE YEAR IN ORBIT

The status of the OSO-7 spacecraft after 12 months in orbit is as follows: All spacecraft subsystems are operative except the redundant tape recorder which was damaged by the tumbling vehicle. Minor difficulties have been encountered with the vernier offset bit in the raster offset system, evidenced by a small shift in the indexing of the raster and offset point grids. These defects have been eliminated by avoiding the use of the vernier bit. This limits the resolution of the commandable offset indexing to about 0.6 arc-minute instead of 0.3 arc-minute. The spacecraft has provided excellent instrument interfacing with only an occasional missed command from ground.

5.1 GENERAL LONG-TERM PERFORMANCE OF SPACECRAFT

The spin axis of the spacecraft was pointing almost directly at the south ecliptic pole after the initial launch acquisition, somewhat different than would have been the attitude with a normal launch sequence.

As shown in Figure 4-5, the spin axis remained pointed near the south ecliptic pole for several weeks. Then the spacecraft was caused to drift in roll so the spin axis was oriented to the north galactic pole by December 18th. This roll maneuver was achieved by using the roll magnetic torquing coils. The use of these coils also applied spin torques and spin gas was consumed in maintaining the wheel spin rate within the automatic control limits.

The wheel spin rate and the spin gas pressure history are shown in Figure 5-1. At the end of the initial launch sequence, the spin gas pressure was about 1540 psi. Another 450 psi of gas was used in the roll maneuver to the north galactic pole. Virtually no spin gas has been used since this maneuver was completed.

Spin rate corrections were made using both manual spin control via the command system and by the automatic on-board spin rate control system. Both systems function properly.

The pitch attitude of the spacecraft has been controlled almost exclusively by magnetic torquing using the pitch coil. The coil status, the corresponding pitch angle, and the pitch gas pressure are shown in Figure 5-2. Both manual and automatic pitch bursts were used to keep the pitch angle within ±3 degrees. Use of the pitch coil was somewhat restricted during the roll maneuvers, since it also exerts roll torques, and to increase the rate of roll correction, pitch gas was used instead of magnetic torquing.

Figure 5-3 shows the spacecraft bus voltage, load current, and solar array current. The points on these plots, as are all the long-term data points, are taken at noon in each orbit. Variations in the loading, solar intensity, solar array temperature, and battery state-of-charge cause scatter in the power system data.

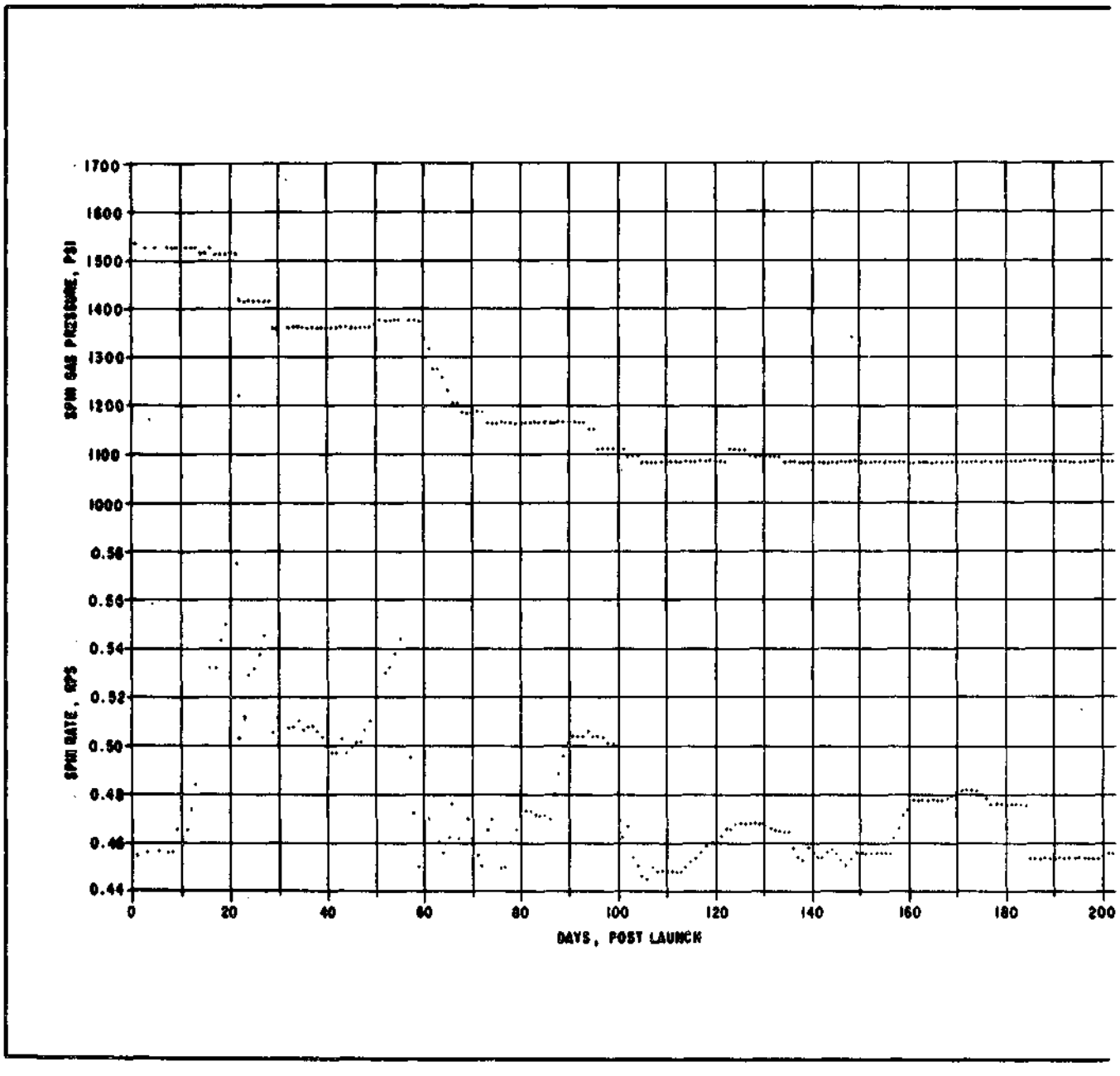

Figure 5-1 Wheel Spin Rate and Spin Gas Pressure History (1 of 2)

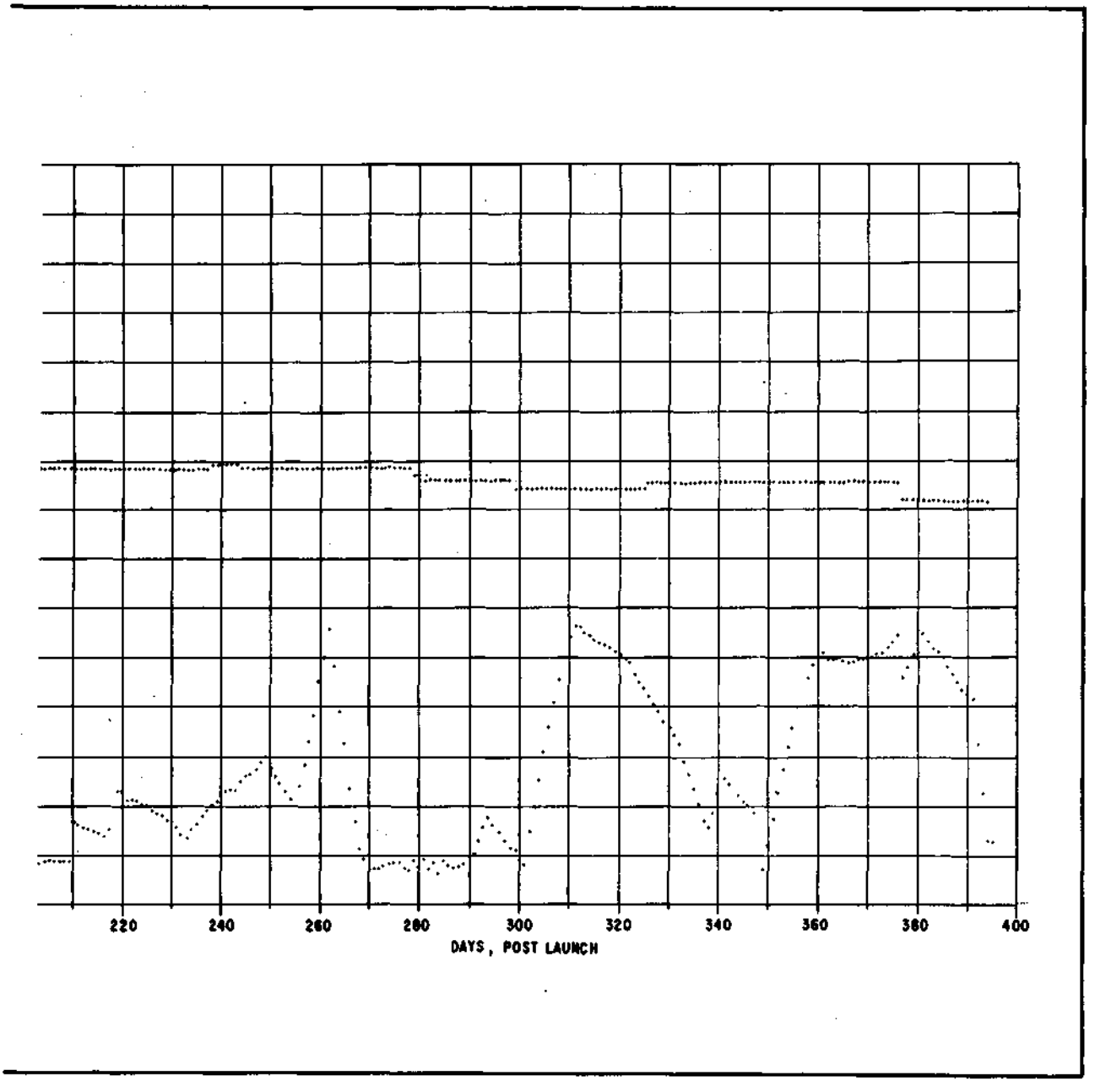

Figure 5-1 Wheel Spin Rate and Spin Gas Pressure History (2 of 2)

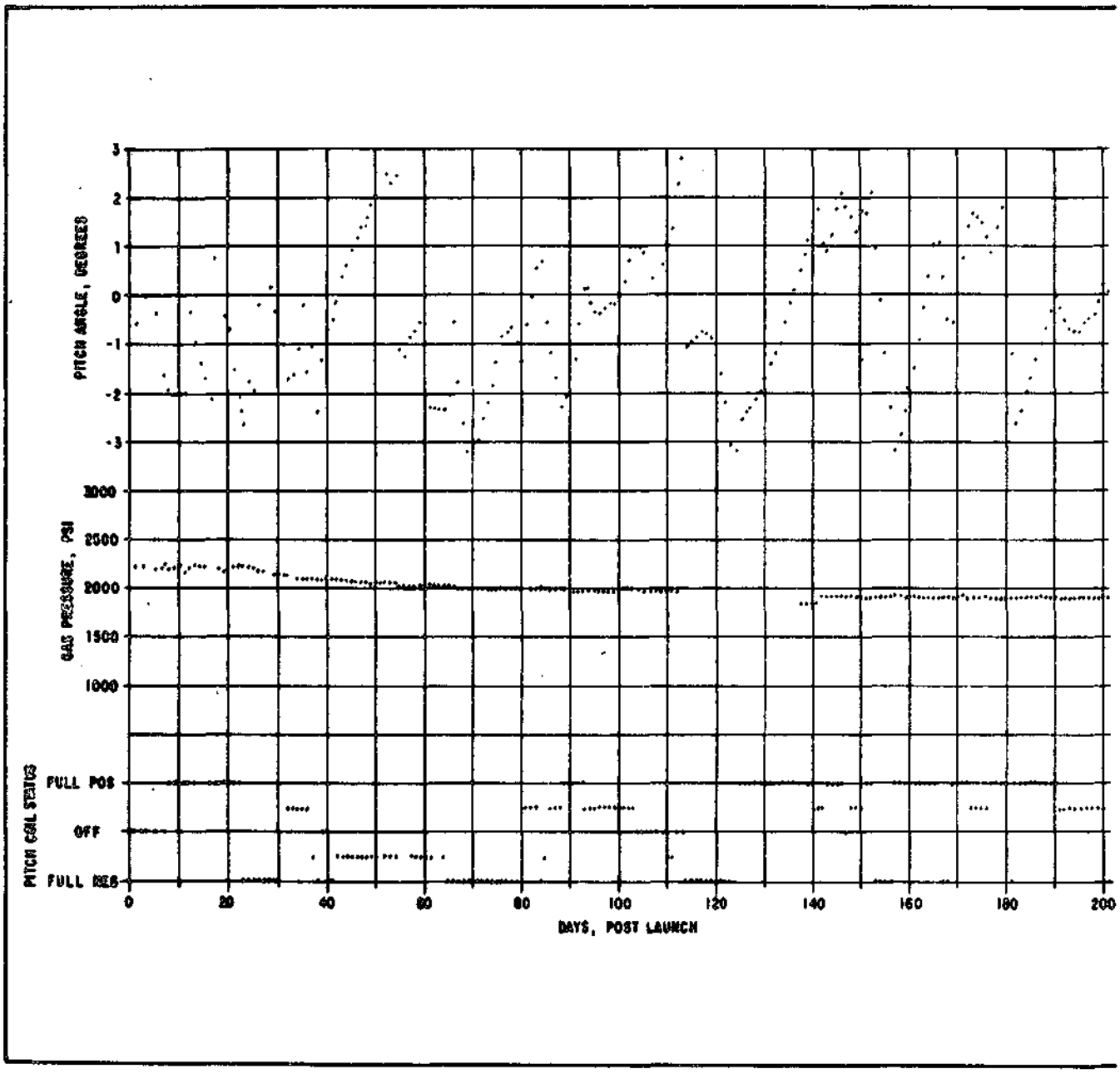

Figure 5-2 Pitch Attitude, Pitch Coil Status, and Pitch Gas Pressure History (1 of 2)

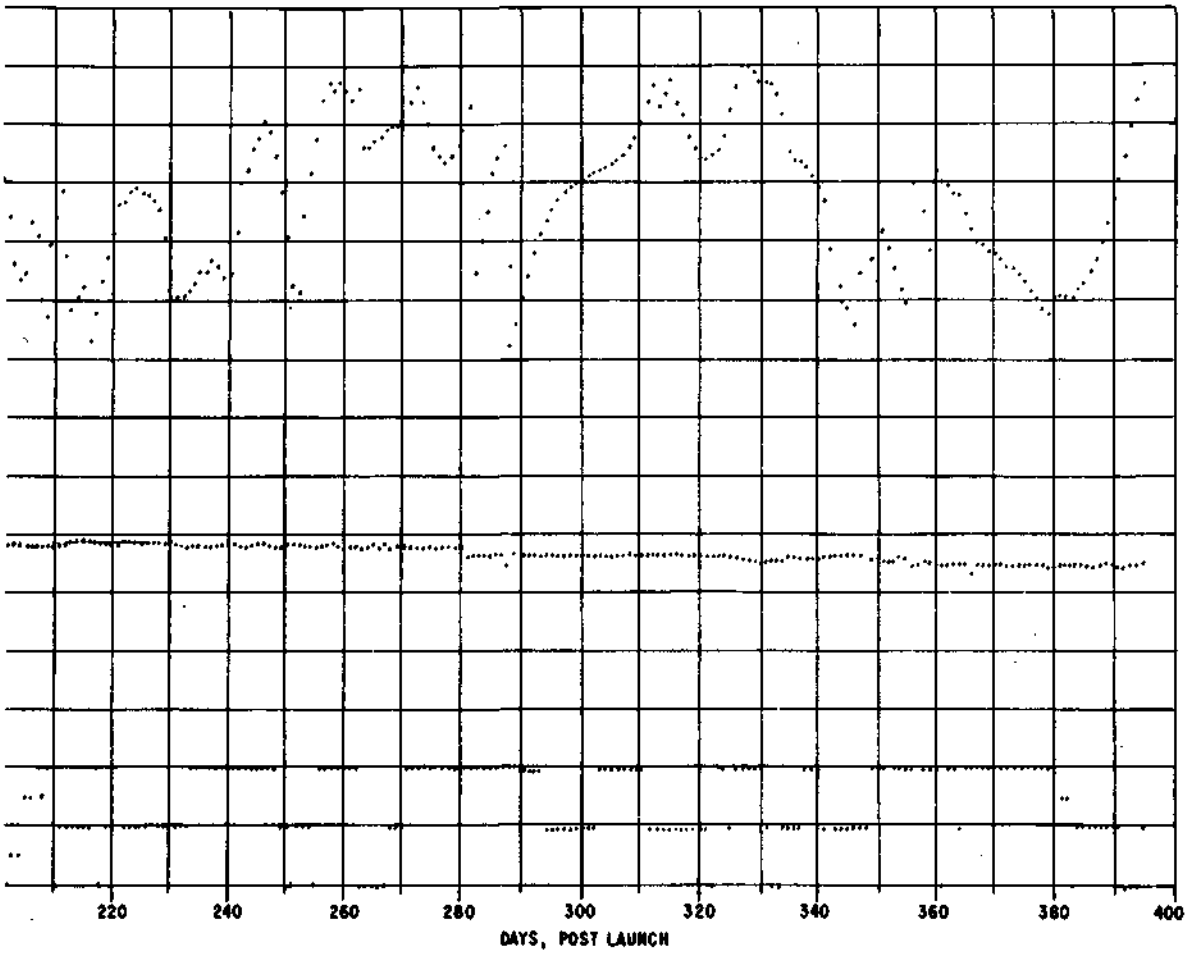

Figure 5-2 Pitch Attitude, Pitch Coil Status, and Pitch Gas Pressure History (2 of 2)

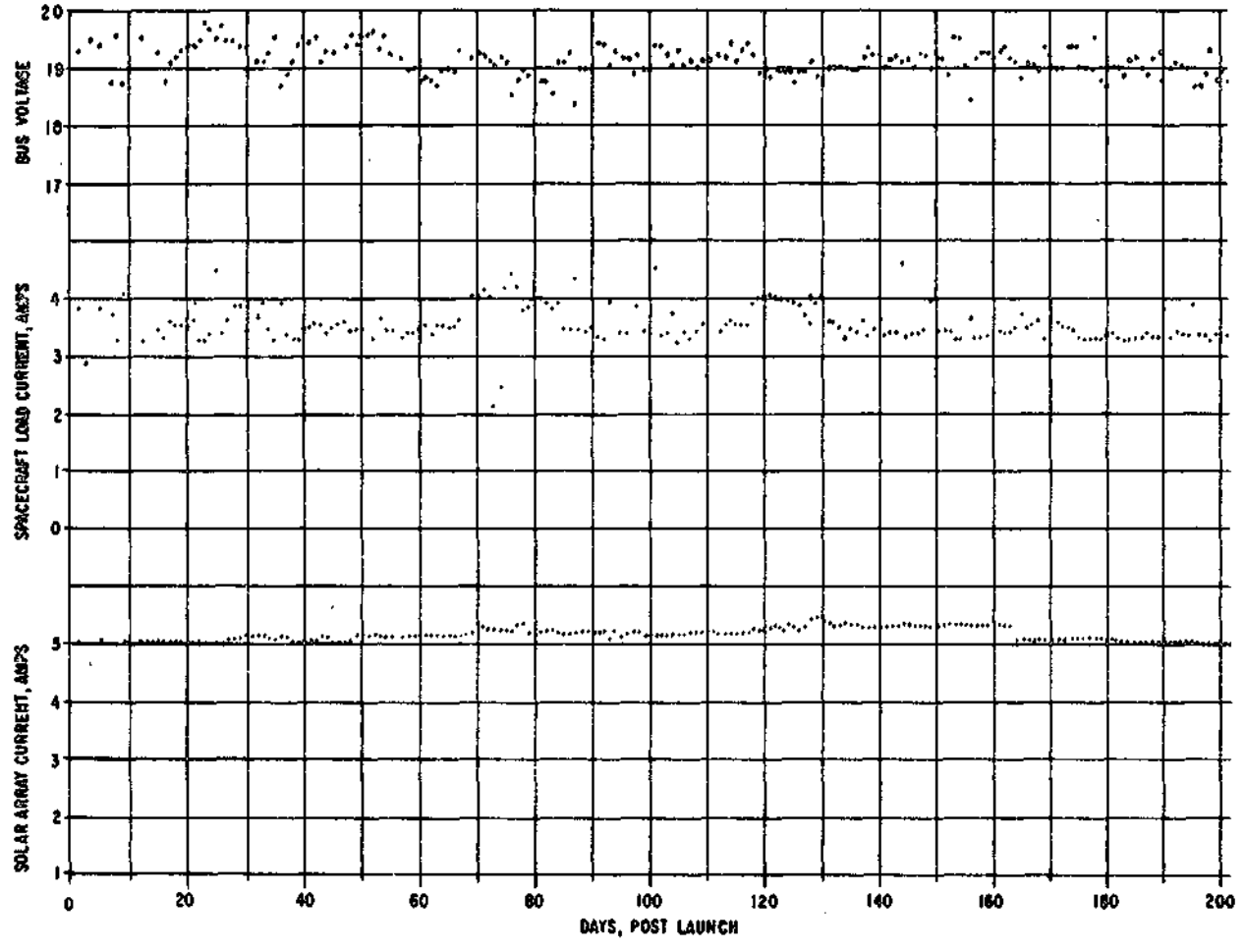

Figure 5-3 Spacecraft Bus Voltage, Load Current, and Solar Array Current History (1 of 2)

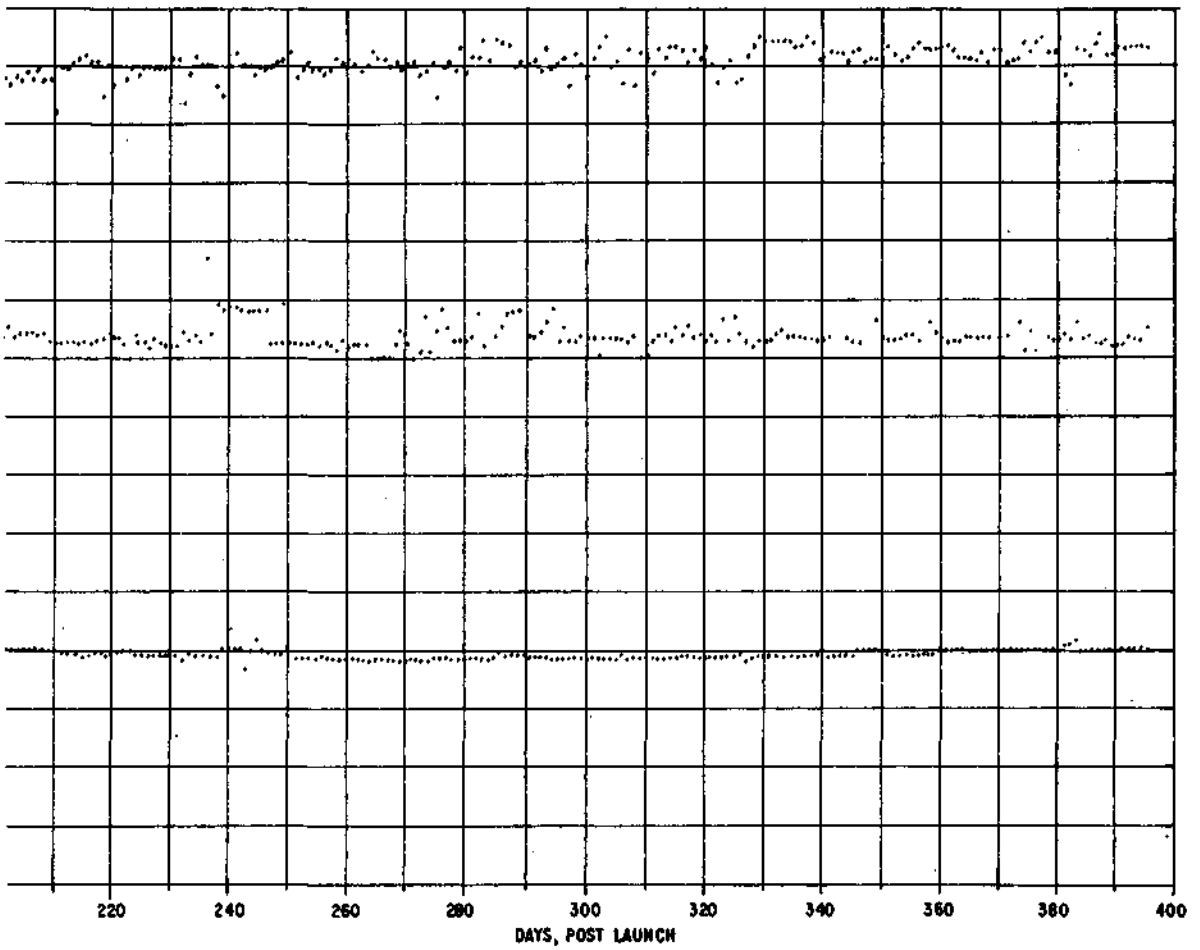

Figure 5-3 Spacecraft Bus Voltage, Load Current, and Solar Array Current History (2 of 2)

There has been no perceptible degradation in the power system performance over 12 months in-orbit. Figure 5-4 shows the integrated solar array power for five orbits picked at random. The output of the array, over 75 percent of the daylight portion of the orbit, is about 97 1/2 watts. These plots have been adjusted for the effects of solar intensity, and the data was taken at times when the attitude of the spacecraft was similar, so that the array temperatures were about the same.

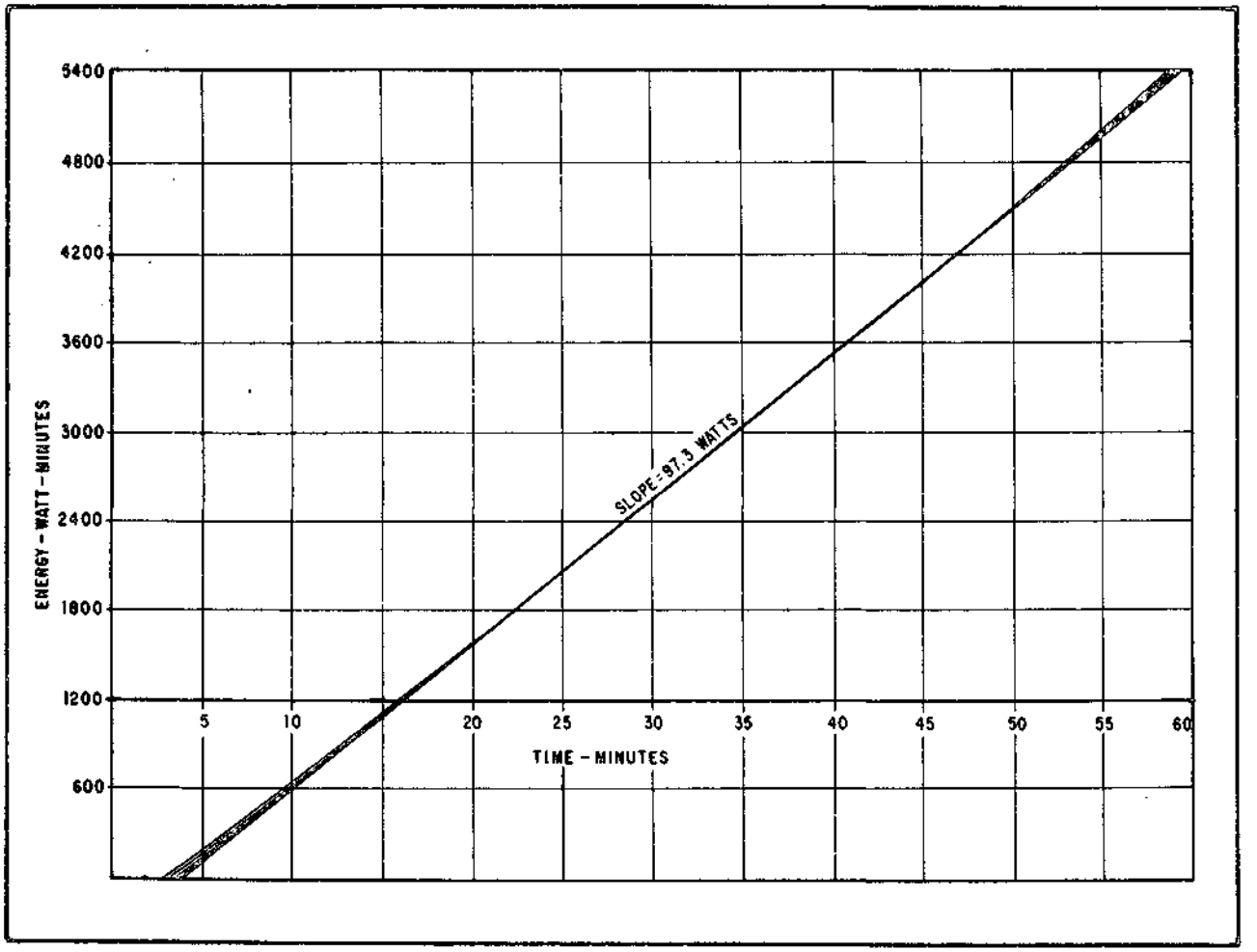

Figure 5-4 Solar Array Energy Developed During Orbit Revolution Nos. 225, 274, 665, 892, 1905

The motor torques on the elevation and azimuth axes have shown little change over the life of the spacecraft and have been as anticipated, as discussed in Section 5.2. All spacecraft temperatures, except the SASC and SASSC, are operating within their acceptance test temperature limits and all spacecraft components are operating within their qualification test temperatures. No solar array panel temperature has exceeded 60°C and therefore solar array performance has been reliable and efficient. Section 5.3 covers in-orbit versus predicted subsystem temperatures.

Figure 5-5 shows the orbit plane angle (β) throughout the first year in orbit. Also shown on this plot are the approximate corresponding minutes per orbit day and minutes per orbit night for each orbit through the year. Figure 5-6 shows the normalized solar intensity through the first year in orbit. Ideally, this normalized plot would be flat at the mean solar intensity, as the yearly variation of ±3 percent has been adjusted out. However, a small variation remains which is in phase with the orbit plane angle variation. This is due to the fact that the target eye output is somewhat temperature-sensitive and the target eye temperature peaks at the higher orbit plane angles. Also shown on this plot are orbit-noon temperatures of the front of the GSFC instrument and the raster read-out eyeblock, which confirm the nature of the variation in the normalized solar intensity plot.

Table 5-1 compares in-orbit performance with contractual design requirement specifications for all spacecraft subsystems.

5.2 STRUCTURAL PERFORMANCE

Structural performance is indirectly evaluated through the proper functioning of the other observatory subsystems. Structural integrity for the most part must be assumed since the spacecraft control and attitude systems functioned normally after exposure to the severe launch sequence environment. The successfully completed launch sequence mechanical events included proper booster fairing/wheel connector separation, sail spin-up using the ADA while the observatory remained on the second booster stage, separation switch activation during observatory/booster separation, wheel spin-up using spin pneumatics after observatory/booster separation, and the pyrotechnic release of the launch-locked nutation damper and pointed instrument package once in orbit.

The low residual wheel wobble throughout the first year of operation shows that the pre-flight dynamic balance resulted in the principal axis of inertia of the wheel being located within 3 arc-minutes of the ADA bearing axis and that the ADA bearing axis orientation has remained extremely stable with respect to the wheel. This is well within the design requirement of no more than 6 arc-minutes zero-to-peak variation in wheel plane motion while the observatory is solar pointing. The observatory's mass moments of inertia (and the accuracy of their measurement at no more than 0.5 percent error) are basically verified by actual nutation decay rate, wobble amplitude, pneumatic and magnetic gyroscopic precession rates, ADA drive rates, and so on.

The suitability of the pointed instrument's alignment adjustment hardware has been confirmed by the very slight shift in the relative alignment between pointed instruments from the time before final environmental test through orbit injection (the allowable change was 15 arc-seconds). The observatory's pneumatic system mass flow rate required accuracy of 15 percent and the total nitrogen leak rate of less than 35 scc/hr have been easily met. The observatory's pre-flight magnetic dipole balancing was adequate, as was the performance of the pitch and roll magnetic coils. No pecularities (such as corona breakdown in high voltage instruments) have been observed due to pneumatic system leakage, venting of the

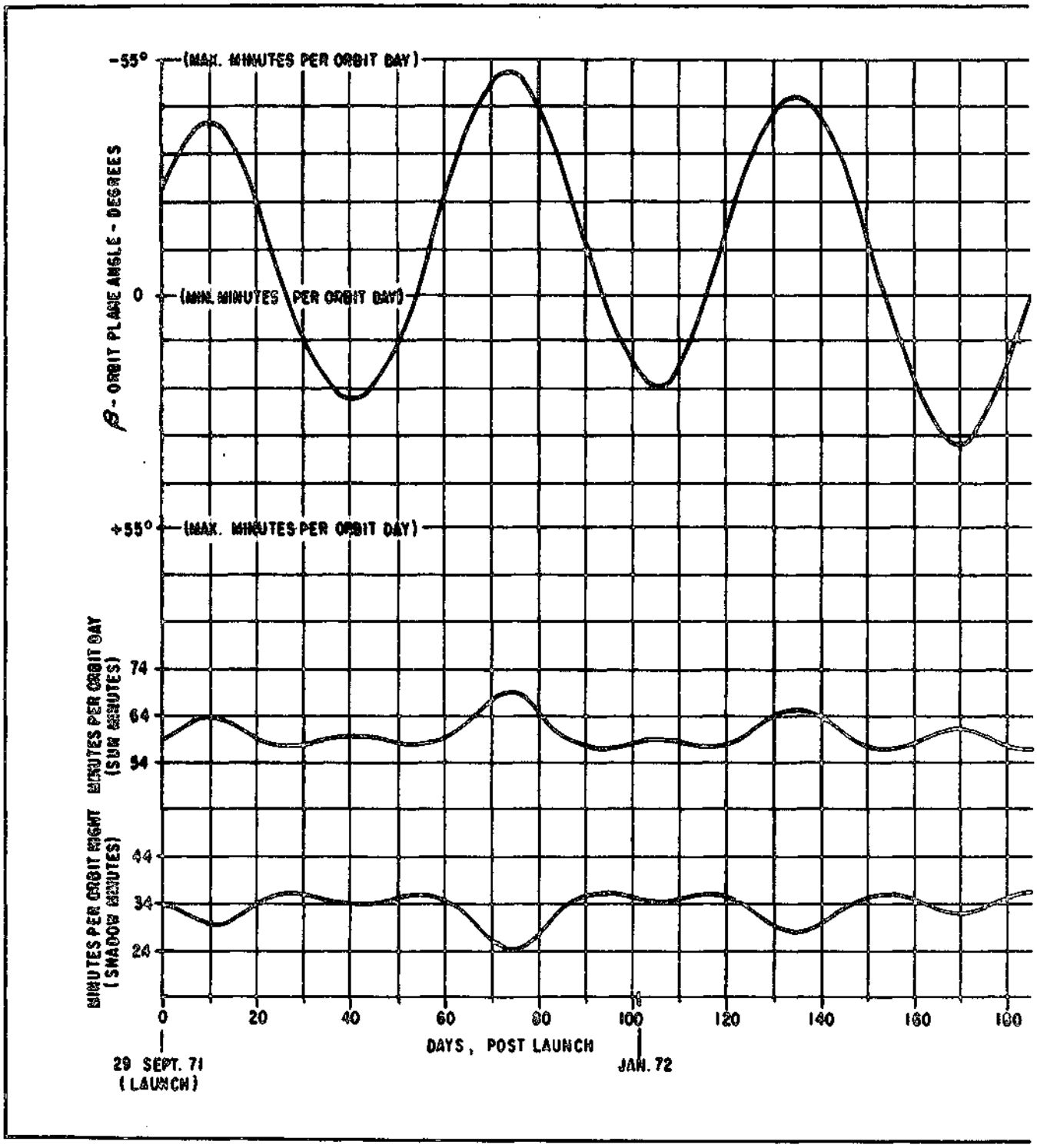

Figure 5-5 Orbit Plane Angle History of OSO-7 Through One Year In Orbit (1 of 2)

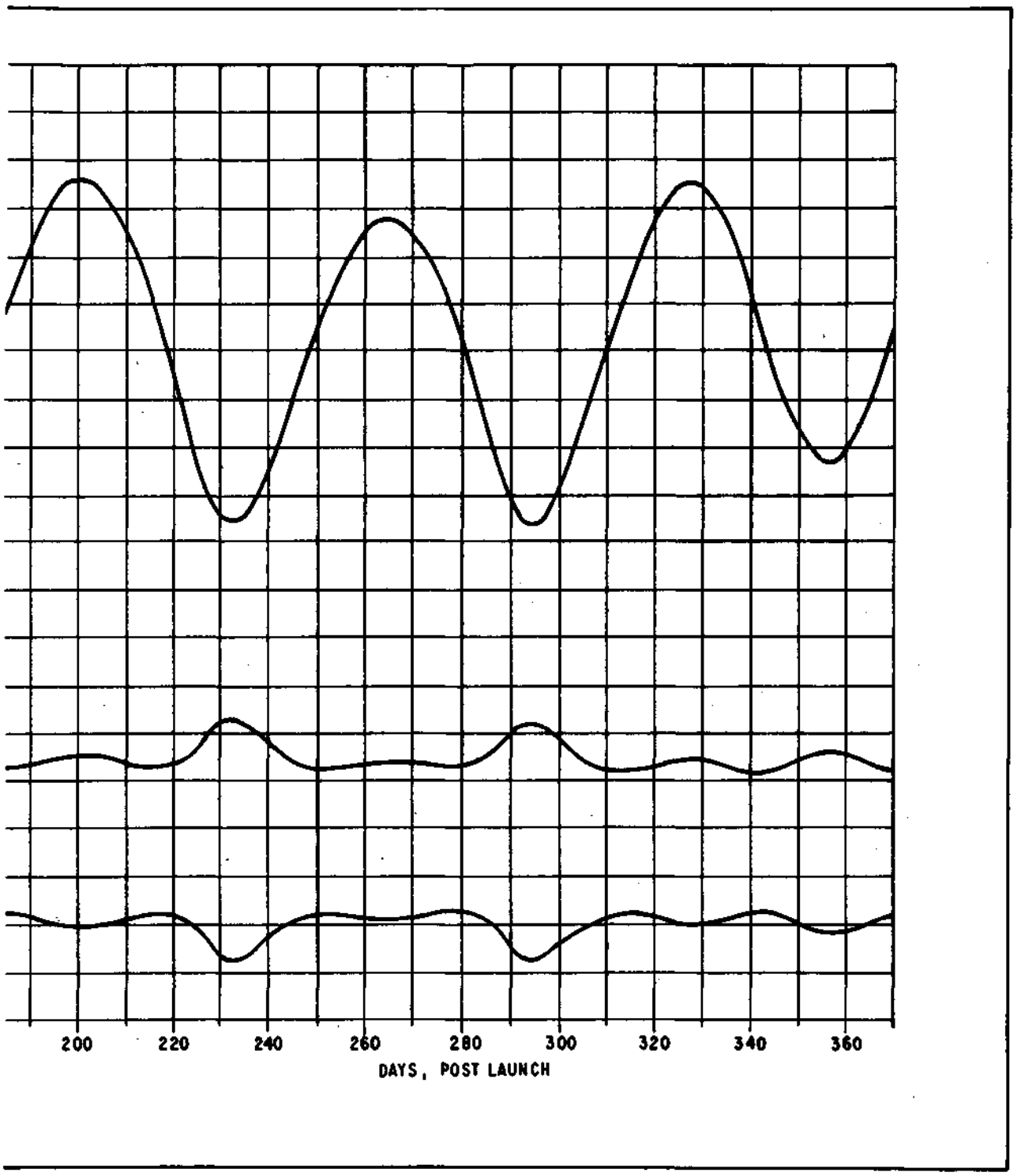

Figure 5-5 Orbit Plane Angle History of OSO-7 Through One Year In Orbit (2 of 2)

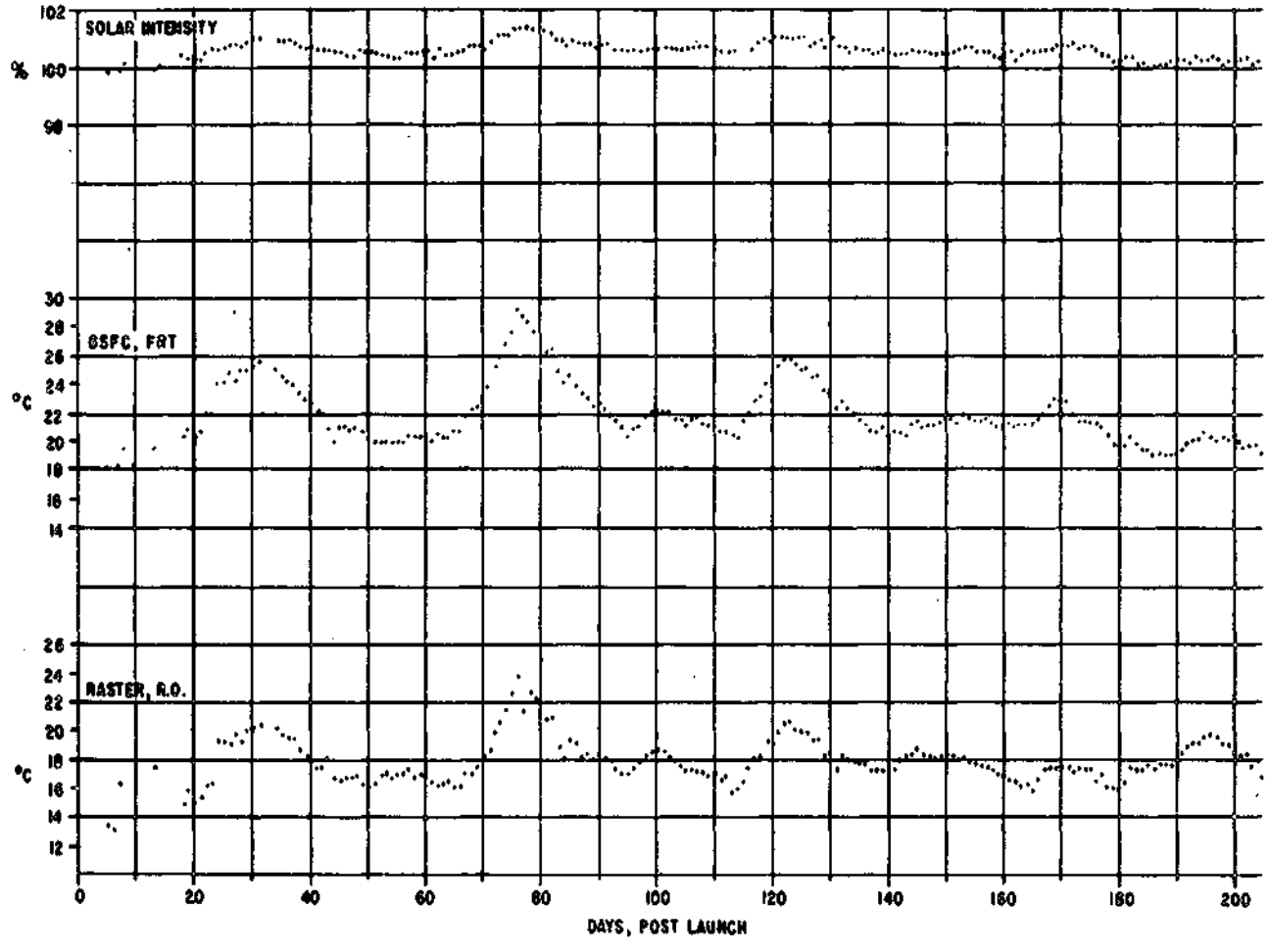

Figure 5-6 Normalized Solar Intensity Through One Year In Orbit (1 of 2)

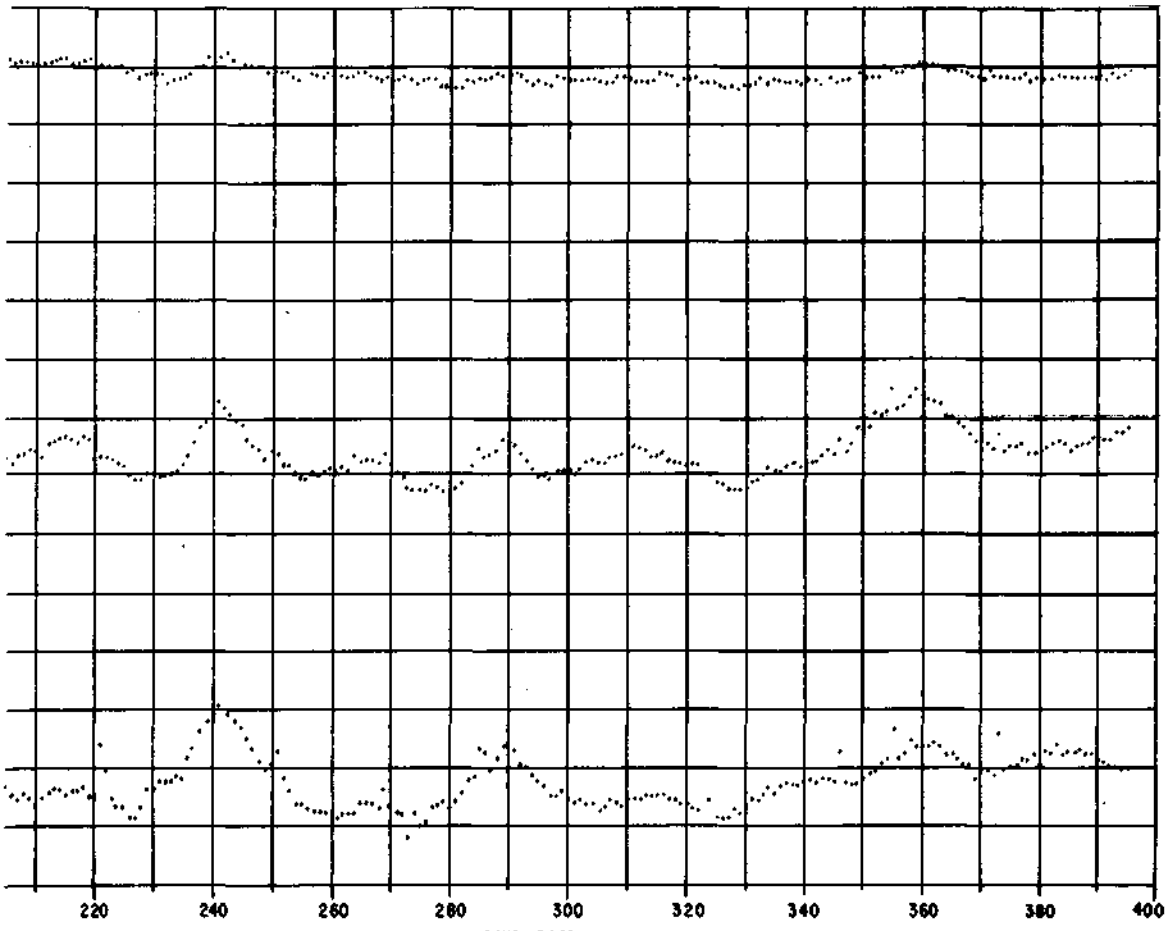

Figure 5-6 Normalized Solar Intensity Through One Year In Orbit (2 of 2)

Table 5-1
OSO-7 PERFORMANCE VERSUS DESIGN REQUIREMENTS

Item	Design Requirement	Actual Performance
Weight	<1500 lb	1415.5 lb
Pneumatic System Capacity and Leak Rate	Pitch gas for 360° pitch + 15° at orbit injection = 375°	416° Total
	Spin gas for 3.3 rps total at launch	3.3 Total
	Leak rate <35 std cc/hr of He tracer (mixture 10% He, 90% N_2)	<3 std cc/hr of He tracer at -10°C (<10 std cc/hr N_2 at -10°C in orbit with 100% N_2 gas)
Solar Array Output	4.7 amp-hrs/orbit at 19V for first 6 months (for nominal orbit day length = 63 minutes)	5.1 amp-hr/orbit
Bus Voltage	19 ± 3V	18.5 ± 1.4V normal operation
Absolute Pointing Accuracy	<1 arc-min (azimuth)	0.5 arc-min azimuth*
	<1 arc-min (elevation)	0.1 arc-min elevation* (*on-board correction can reduce relative error to <0.1 arc-min once absolute error is known)
Pointing Drift	<10 arc-sec during orbit (azimuth)	<6 arc-sec
	<10 arc-sec during orbit (elevation)	<6 arc-sec
Pointing Jitter	<3 arc-sec rms random motion (azimuth)	<1.5 arc-sec P-P
	<5 arc-sec peak, clipped sinusoid (elevation)	<1.5 arc-sec P-P
Large Raster Size	60 az arc-min x 60 el arc-min ±3 arc-min (at mean solar intensity)	61.1 az arc-min x 61.1 el arc-min
Small Raster Size	5 az arc-min x 5 el arc-min ±0.5 arc-min	5.15 az arc-min x 5.13 el arc-min
Pattern Center Offset	<0.1 arc-min (large raster)	Approximately 0.07 arc-min
	<0.1 arc-min (small raster)	Approximately 0.07 arc-min
	<0.2 arc-min (offset grid)	Approximately 0.07 arc-min
Day to Night Shift (Inertial Ref. Auto Mode)	<15 arc-min shift in azimuth	<5 arc-min
Inertial Reference Drift	<0.5°/hr	<0.1°/hr
Auto Spin Mode Control	0.43 rps to 0.68 rps	0.45 rps to 0.58 rps (manual mode often used)
Pneumatic Spin Rate of Change	0.01 rps/burst ± 25%	0.0097 rps/burst (calculation)
Pneumatic Pitch Rate of Change	0.036° - rps/sec = approx 0.72°/burst at 30 rpm	0.038° - rps/sec = approx 0.76°/burst (calculation)
Large Angle Pitch Readout	±90° coverage with ±1° accuracy	OK

Table 5-1 (Cont.)

Item	Design Requirement	Actual Performance
Max Spin Rate Change Per Wheel Revolution	Such that wheel spin location can be predicted within 0.1° based on spin rate of previous revolution	<0.1°
Auto Pitch Limits	Spin axis ±4° from perpendicular to solar direction	+2.8 to -3.2° (manual mode and magnetic torquing are often used)
Nutation Control and Spacecraft Stability	Day wheel plane excursion <±0.1° in 3 minute period	<±0.05°
	In offset point mode, <±0.1° within 2 minutes after turn on	This is met if offset point mode is turned on 5 minutes or more after start of day acquisition
Magnetic Dipole Moment	Accuracy of magnetic dipole moment along each axis (coils off) <500 gauss-cm^3	Due to GSFC instrument's internal moving magnets this accuracy cannot be guaranteed. Actual moments and variation as follows: X=0±820, Y=0±1700, Z=-6040±1050
Aspect System	Magnetometer to locate spin axis (coils off) <3°	Approximately 3°
Aspect System	Magnetometer to locate spin axis (coils on) <6°	Approximately 5°
	Locate wheel az angle, with respect to OSO time, <0.1° at least once every 15.36 sec each orbit night	<0.1°
Aspect Sensor	Locate spin axis <0.1° (in conjunction with magnetometer)	<0.05°
Receiving Antenna Gain	Gain >-18dB over at least 3.8π steradians	≥-18dB (avg -12 dB)
Transmitter Power Output	RF power output >+27dBm at 19V	+28.5dBm
Transmitting Antenna Gain	Nominally -8dB	≥-6dB

sealed honeycomb structure, or normal pneumatic system nitrogen bursts. Contamination (and therefore degradation) of optical surfaces from outgassing materials has not been a concern during the first year of OSO-7 in-orbit operation.

Both the azimuth and elevation drives have performed in accordance with their requirements. Bearing friction ripple has been low enough so that pointing jitter in both systems is less than 1.5 arc-seconds compared to the allowable 3 arc-seconds RMS. Figure 5-7 shows azimuth and elevation motor torques through the first year of operation. The azimuth motor torque is seen to vary from 38 to 44 oz-in., which corresponds closely to predicted ADA values at hub temperatures from 18°C to 8°C. The elevation motor torque is seen to remain fairly constant over the long term at about 14 oz-in., with the predominant portion (12 oz-in.) being due to the elevation bias spring. This is as expected.

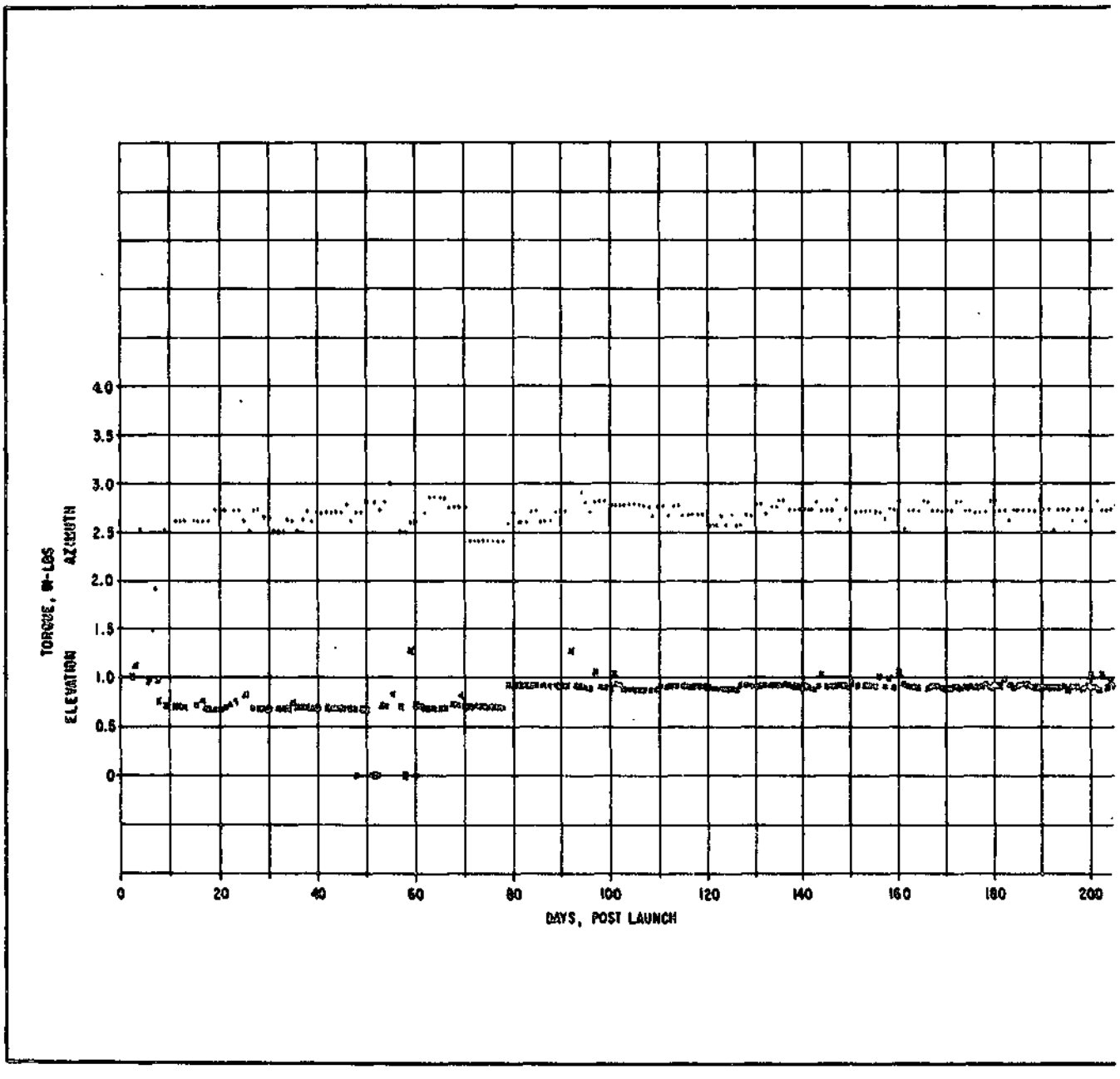

Figure 5-7 Elevation and Azimuth Motor Torque History (1 of 2)

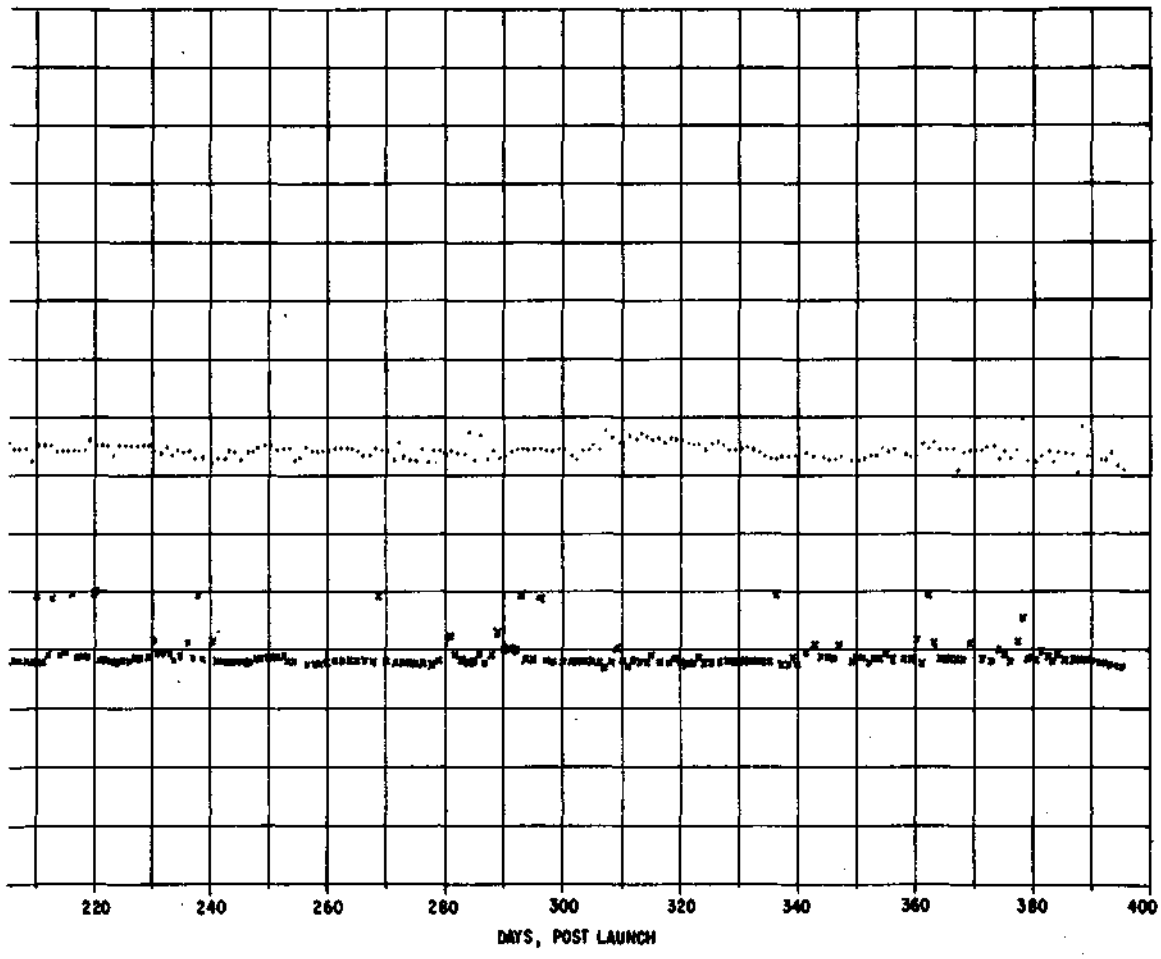

Figure 5-7 Elevation and Azimuth Motor Torque History (2 of 2)

The mechanical/structural aspects relating to individual subsystems are covered in greater detail in each individual subsystem performance section that follows.

5.3 THERMAL PERFORMANCE

Table 5-2 compares the analytically predicted minimum, nominal, and maximum spacecraft subsystem temperatures to the actual observed minimum, nominal, and maximum temperatures during orbit revolution 77. For this orbit, the orbit plane angle and solar intensity were very close to the nominal values used in the thermal analysis. The roll angle orientation was different by 75°, but the temperature difference is only a few degrees C and only really affects rear sail temperatures. As can be seen, all the wheel temperatures are within 5°C of the predicted values. Nearly all the sail components, excluding the instruments, are operating within 5°C of the predicted values. The solar array panels are operating 7 to 15°C cooler than anticipated, which is beneficial from an efficiency and reliability standpoint. The power amplifier appears to be operating about 14°C too warm but this has been attributed to the temperature probe being located at a hotspot and the actual mean-mass temperature is considered to be within 5°C of the predicted value. Figures 5-8 through 5-11 show wheel component, wheel instrument, sail component and sail instrument transient temperatures through the "day" and "night" portions of orbit revolution 77. Figure 5-12 shows the two solar array panel temperatures throughout the first year in orbit (all data taken at orbit-noon).

Orbit revolution 1178 had an orbit plane angle of 53.6° and very nearly maximum solar intensity and therefore the spacecraft subsystems are the hottest for this orbit. Table 5-3 compares these peak in-orbit temperatures to the predicted peak predicted temperatures. It is seen that only 2 temperature sensitive components, the SASC and the SASSC, were hotter than their analytically predicted acceptance temperatures (SASC too hot by 5.7°C and SASSC too hot by 2°C). All components are performing within their qualification temperature limits as predicted by analysis and the thermal balance test.

5.4 PITCH ATTITUDE CONTROL SUBSYSTEM PERFORMANCE

Figure 5-13 indicates the behavior of the spin axis as the spacecraft comes into orbit day, and acquires in elevation. The nutation of approximately 0.8 degree peak-to-peak at the beginning of orbit day is caused by the momentum disturbance as the elevation drive moves the pointed instrument assembly off its snubber, overcoming the bias spring, and into pointing position. During this orbit, the spacecraft was in the small raster pointing mode, and the associated residual peak-to-peak variation in wheel plane angle is seen to be less than 0.16 degree. The design specification for peak-to-peak variation is 0.2 degree.

Table 5-2

PREDICTED FLIGHT TEMPERATURES VERSUS ORBIT NO. 77 FLIGHT DATA
(Nominal Orbit Plane Angle and Nominal Solar Intensity)

		Temperature, °C					
		Prediction			Flight Data		
Node	Name	Max	Nom	Min	Max	Nom	Min
1	Despin Drive (Housing on Wheel Side)	17.3	17.1	17.0	18.5	18.4	18.0
	Despin Drive (Shaft on Sail Side)	17.3	17.1	17.0	16.2	16.2	16.2
4	Wheel Hub	13.3	12.9	12.6	12.5	12.2	11.3
27	Spin Gas Bottle	12.3	12.3	12.2	13.2	11.7	12.5
78	Rib Comp No. 7	12.9	12.2	11.5	14.1	12.5	10.9
103	Upper Left Solar Panel	67.8	38.4	-28.3	52.9	28.9	-21.3
105	Lower Left Solar Panel	63.8	43.5	1.2	57.2	36.8	3.7
112	Left Trunnion	20.6	19.8	19.0	20.4	19.4	18.1
134	Sail Analog Subcommutator	8.9	2.6	-4.8	13.0	8.4	1.5
135	Power Amplifier	16.8	15.5	14.0	31.0	29.2	27.0
136	Servo Amplifier	21.4	20.2	18.4	19.6	18.7	17.7
139	NRL (Fore)	18.9	18.1	17.1	---	---	---
	NRL	18.9	18.1	17.1	14.5	13.3	10.8
140	NRL (Mid)	17.6	17.3	16.9	---	---	---
	NRL	17.6	17.3	16.9	---	---	---
	NRL	17.6	17.3	16.9	9.4	9.1	8.2
142	NRL (Eyeblock)	22.7	20.1	16.5	15.0	11.9	8.0
143	GSFC (Fore)	30.0	29.2	28.3	19.0	17.6	15.9
	GSFC	30.0	29.2	28.3	19.0	17.7	16.3
144	GSFC (UV) Slit	28.2	27.9	27.6	16.7	16.3	15.9
	GSFC (Mid)	28.2	27.9	27.6	15.6	15.3	14.8
145	GSFC (Aft)	28.5	28.0	27.6	17.8	15.5	12.9
150	Sail Analog Sub-Subcommutator (Left)	24.5	21.0	17.2	24.9	21.4	17.9
162	GSFC - Thermal Monitor	23.4	21.0	18.3	17.5	15.1	9.2
	GSFC - Thermal Monitor	23.4	21.0	18.3	17.1	13.1	11.3
331	Pitch Gas Bottle (Right Aft)	19.2	15.3	11.2	6.7	3.0	-0.7
505	OIRU (TG Temperature)	44.1	39.5	34.5	43.4	38.7	31.7
506	OIRU Mounting Flange	31.9	25.7	17.1	39.5	32.4	24.2
601	Antenna	12.6	10.6	8.6	15.2	10.6	3.5
1012	Batteries Comp No. 1	14.3	13.8	13.5	15.7	14.9	13.6
3010	MIT (Power Converter)	17.5	16.5	15.6	20.0	20.0	20.0
	MIT (Base Plate)	17.5	16.5	15.6	14.3	13.5	13.0
	MIT (Cal. Actuator)	17.5	16.5	15.6	18.2	16.8	15.2
	MIT (Memory)	17.5	16.5	15.6	20.2	20.2	20.2
	MIT (Lower Detector)	17.5	16.5	15.6	16.8	15.8	15.4
	MIT (Upper Detector)	17.5	16.5	15.6	17.8	17.4	16.7
4000	Deck Compartment No. 4	16.8	16.3	16.0	14.4	14.4	14.4
4001	Cover Compartment No. 4	13.4	12.4	11.6	16.9	12.4	10.2
7000	Deck Compartment No. 7	13.7	13.4	13.1	13.7	13.6	13.0
7003	Rim Compartment No. 7	17.3	11.8	4.5	17.0	13.2	8.2
8010	UCSD-S	10.7	10.3	9.9	14.5	14.1	13.5
9010	UNH (Electronics)	13.8	13.6	13.4	17.4	17.2	16.7
	UNH (Detector)	13.8	13.6	13.4	14.5	14.1	13.8

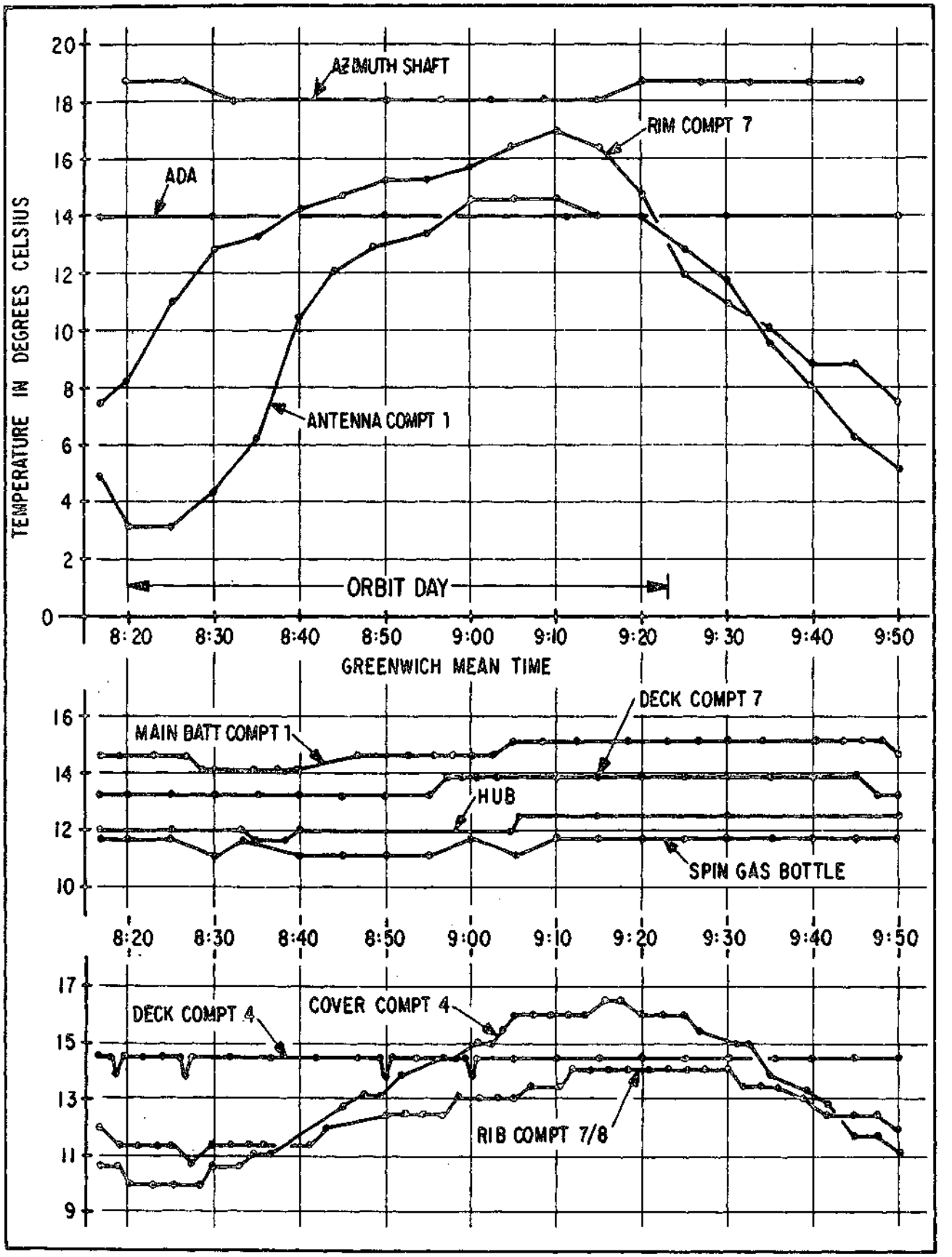

Figure 5-8 OSO-7 Wheel Transient Temperatures, Orbit Revolution 77

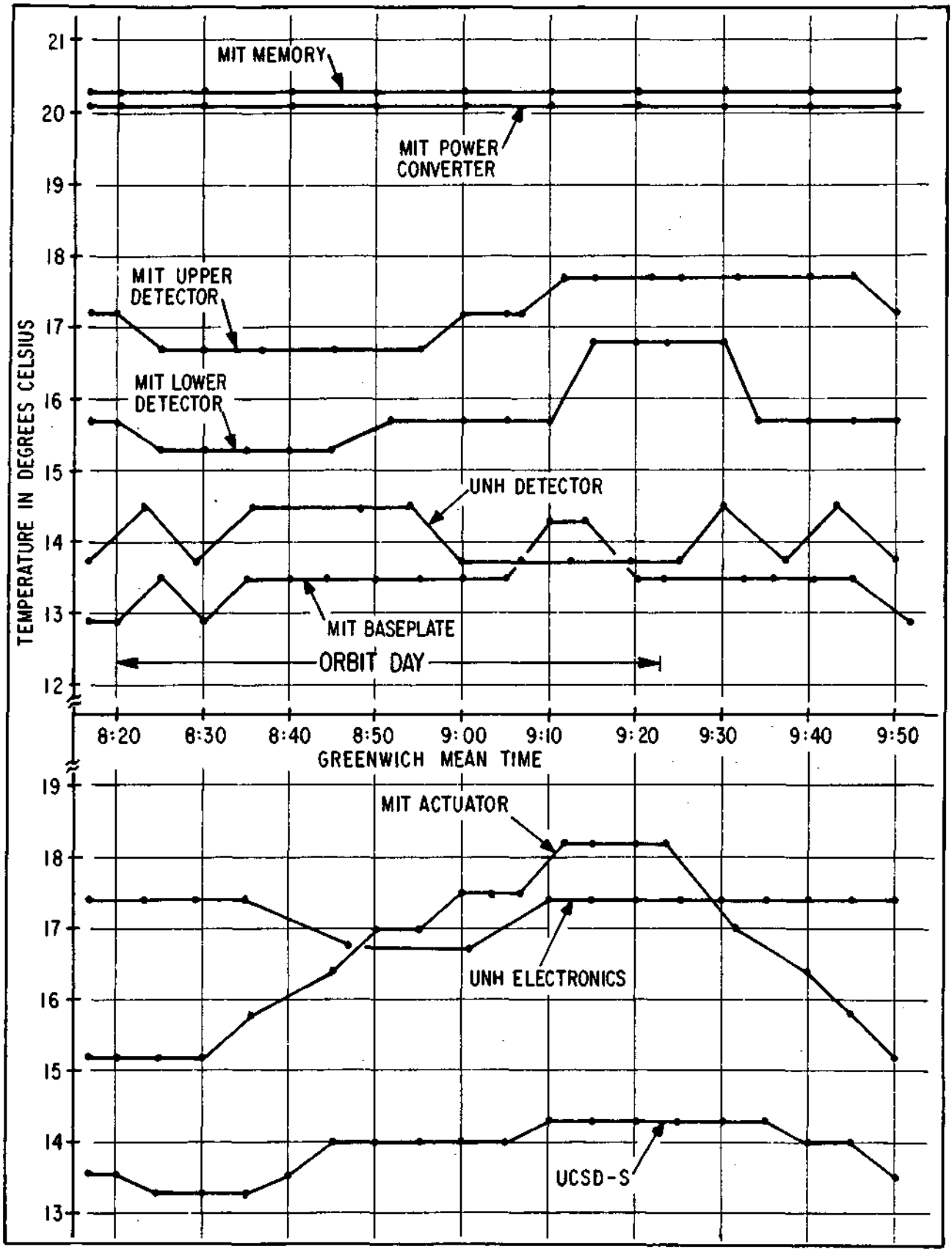

Figure 5-9 OSO-7 Wheel Experiment Transient Temperature, Orbit Revolution 77

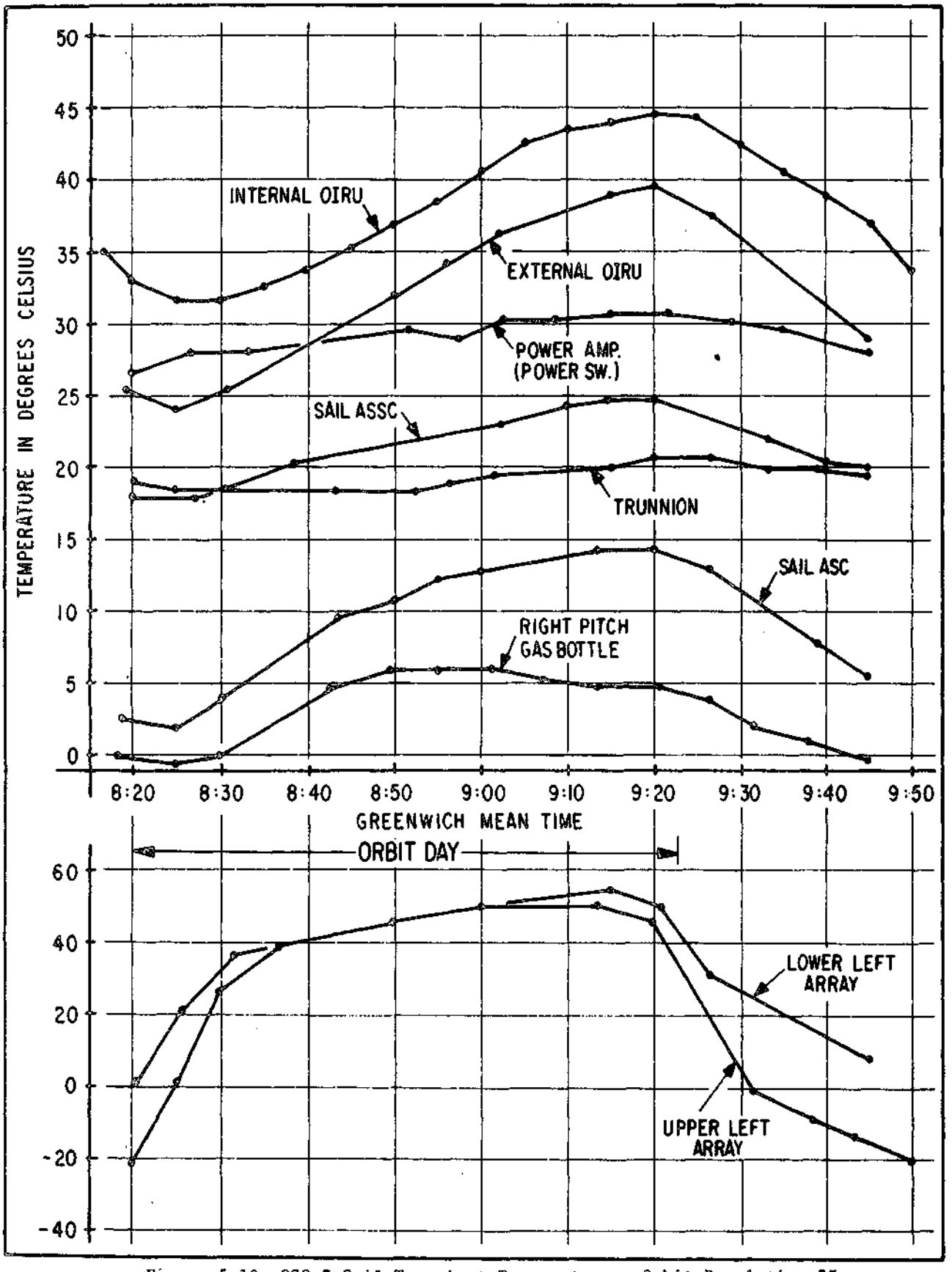

Figure 5-10 OSO-7 Sail Transient Temperatures, Orbit Revolution 77

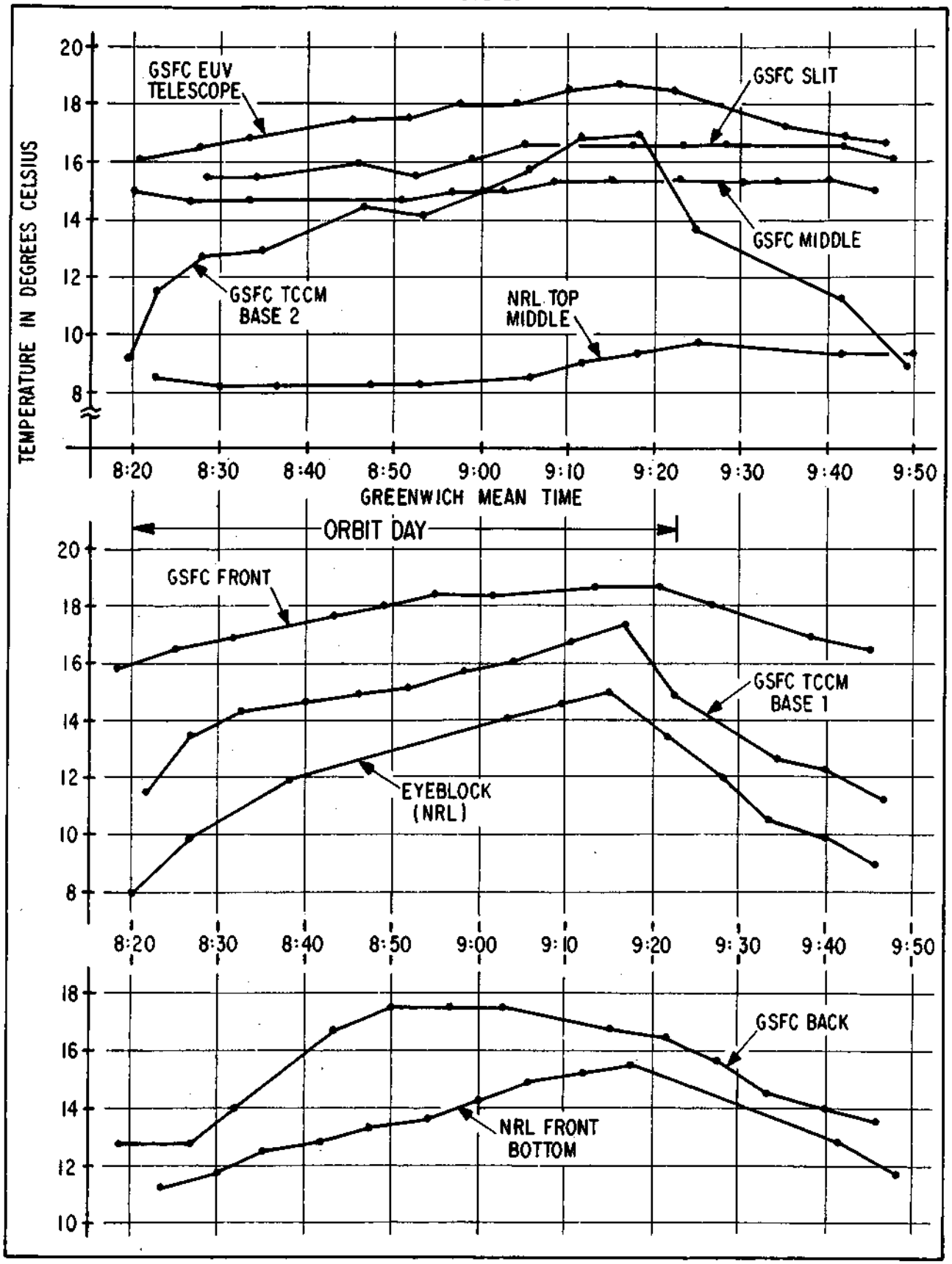

Figure 5-11 OSO-7 Pointed Experiment Transient Temperature, Orbit Revolution 77

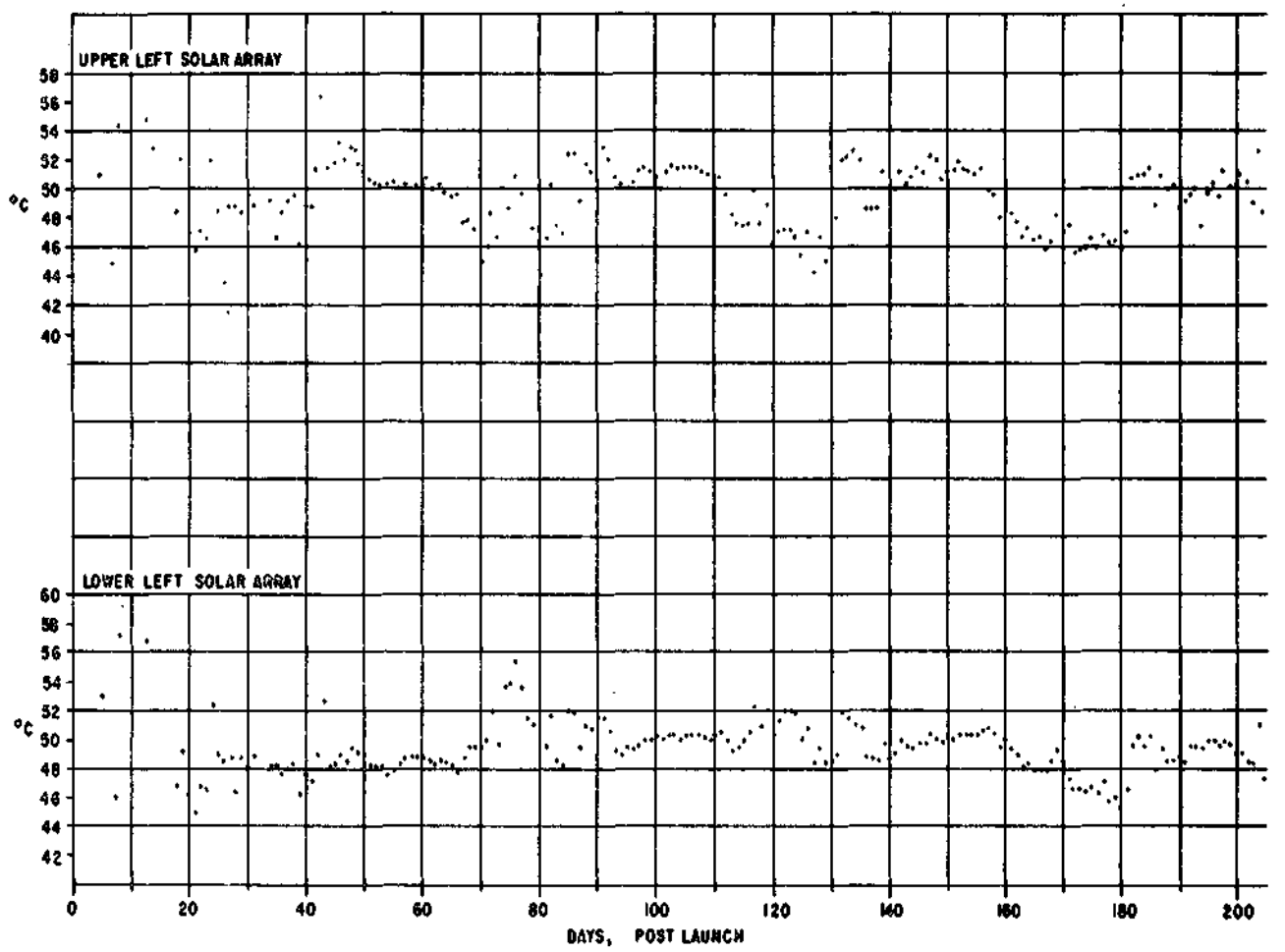

Figure 5-12 Solar Array Temperature History (1 of 2)

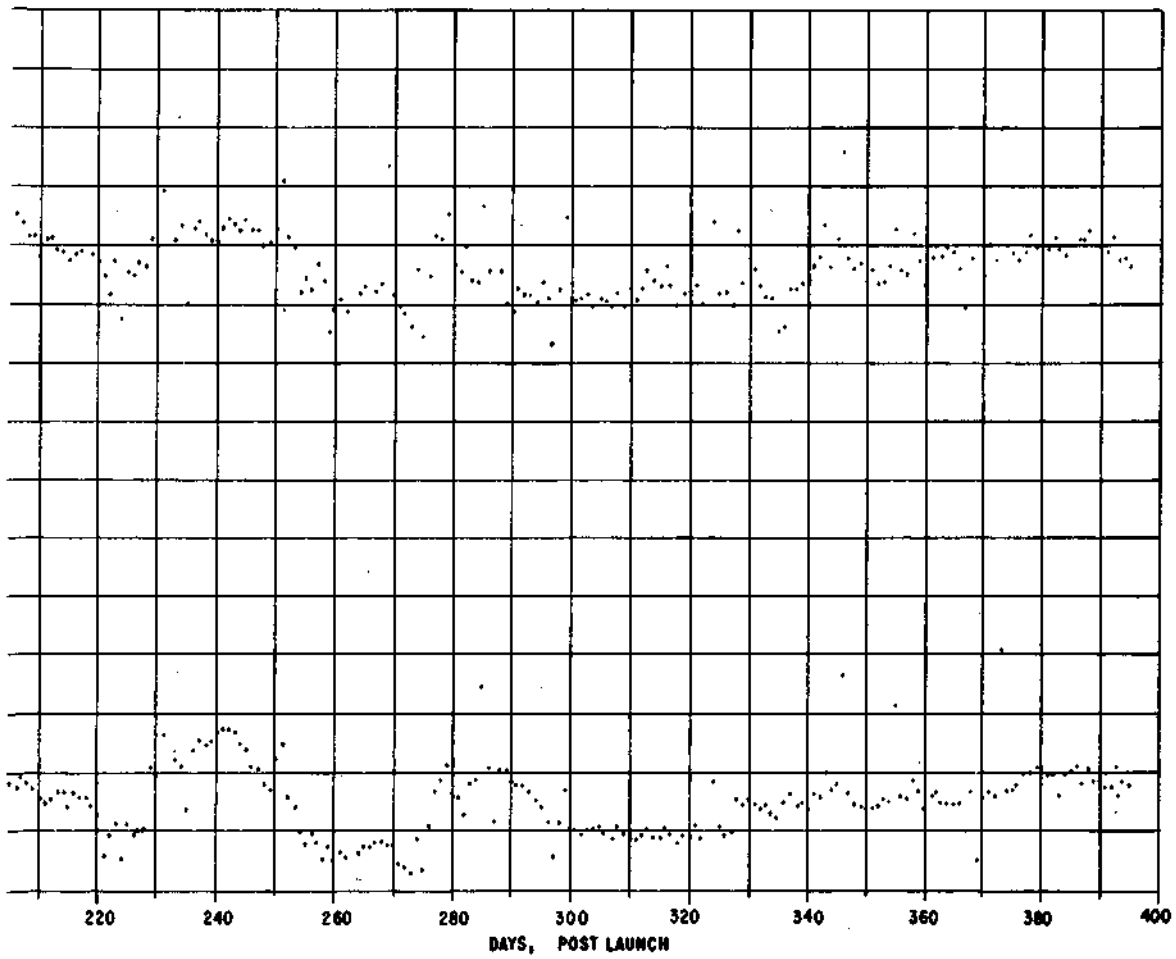

Figure 5-12 Solar Array Temperature History (2 of 2)

Table 5-3

PREDICTED PEAK ACCEPTANCE TEMPERATURES AND PEAK ORBIT TEMPERATURES FROM ORBIT REVOLUTION 1178

(Maximum Orbit Plane Angle and Maximum Solar Intensity)

Node	Name	Temperatures - °C	
		PREDICTED* Peak Orbit Temperatures Acceptance	FLIGHT Peak Temps. β=53.6°, Orbit 1178
1	Despin Drive SASSC #2-6	27.8	(25.5) 27.7
	Despin Drive WASC-17	27.8	23.2
4	Wheel Hub WASC-23	23.8	20.4
27	Spin Gas Bottle WASC-18	22.8	21.2
78	Rib Comp. #7 WASSC-3,11,19	23.4	21.9
103	Upper Left Solar Panel SASSC #2-1	78.3	55.1
105	Lower Left Solar Panel SASSC #1-5	74.3	60.7
112	Left Trunnion SASSC #2-7	31.1	30.1
134	Sail Analog Subcomm SASSC #2-4	19.4	25.1
135	Power Amplifier SASSC #1-11	27.3	
136	Servo Amplifier SASSC #2-3	31.9	26.8
139	NRL (Fore) SASSC #1-19	29.4	
	NRL SASSC #1-21	29.4	23.7
140	NRL (Mid) SASSC #1-17	28.1	
	NRL SASSC #1-18	28.1	
	NRL SASSC #1-20	28.1	17.7
142	NRL (Eyeblock) SASSC #1-10	33.2	25.9
143	GSFC (Fore) SASSC #1-4	40.5	29.5
	GSFC (Telescope) SASSC #1-13	40.5	29.5
144	GSFC (UV) Slit SASSC #1-16	38.7	27.1
	GSFC (Mid) SASSC #1-6	38.7	35.9
145	GSFC (Aft) SASSC #1-7	39.0	27.1
150	Sail Analog Sub-Subcomm (Left) SASSC #1-9	35.0	37.0
162	GSFC - Thermal Monitor SASSC #2-20	33.9	29.0
	GSFC - Thermal Monitor SASSC #2-12	33.9	29.8
331	Pitch Gas Bottle (Right Aft) SASSC #1-3	29.7	16.9
505	OIRU (TG Temperature) SASC-42	54.6	49.8
506	OIRU Mounting Flange SASSC #2-5	42.4	44.5
601	Antenna WASC-38	23.1	20.6
1012	Batteries Comp #1 WASSC-1,9,17	24.8	23.4
4000	Deck Compt. #4 WASC-19	27.3	23.5
4001	Cover Compt. #4 WASSC-6,14,22	23.9	23.6
7000	Deck Compt. #7 WASSC-4,12,20	24.2	22.8
7003	Rim Compt. #7 WASC-21	27.8	24.5

*These temperatures are the maximum predicted orbit values from Table 5-2 with an added +5°C for modeling errors and +5.5°C for yearly orbital variations.

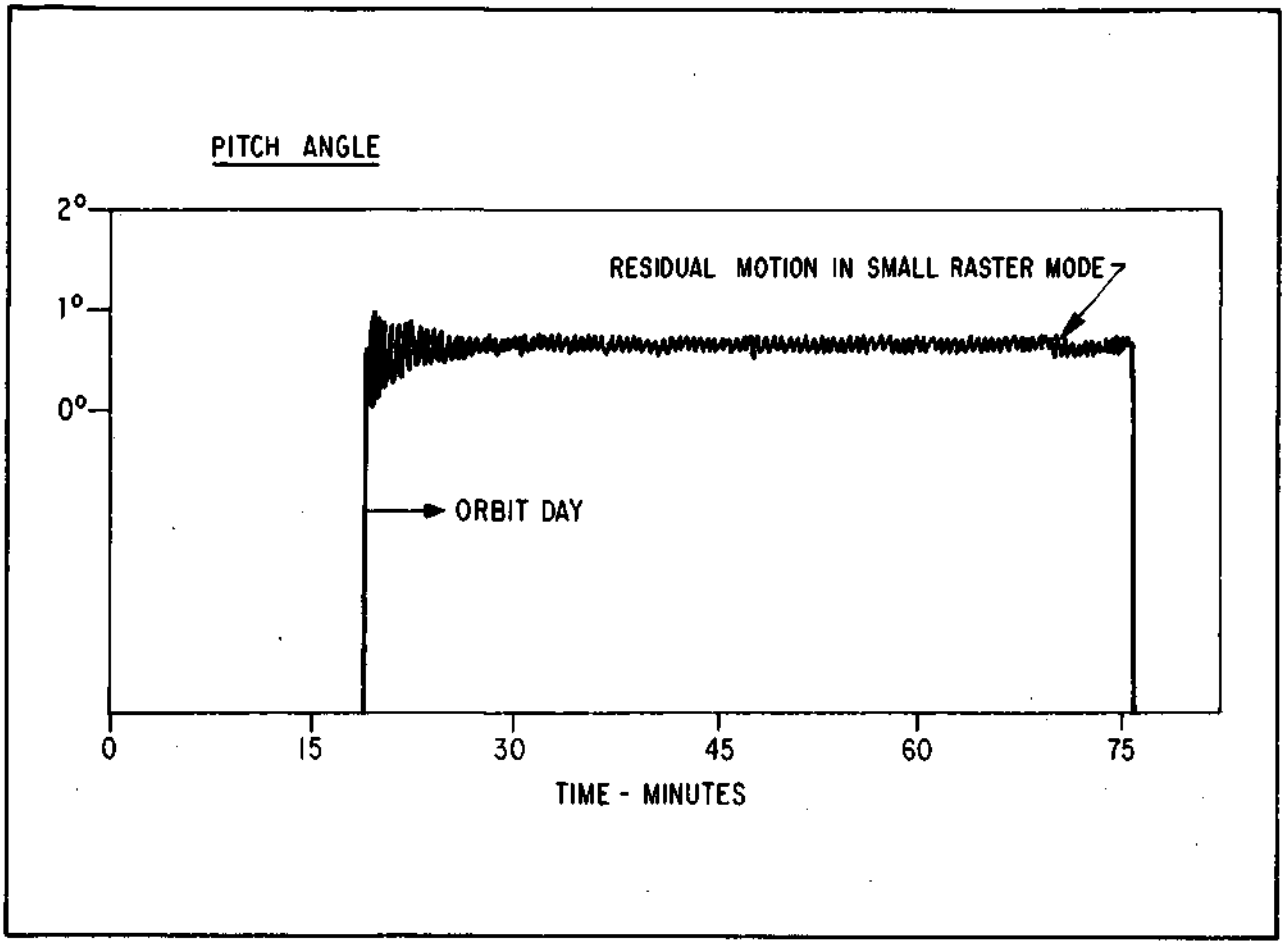

Figure 5-13 Spin-Axis (Pitch) Motion After Dawn Acquisition (Gyro Control During Night-Orbit Revolution No. 968) While in Small Raster Pointing Mode

In Figure 5-14, the spacecraft was in the small raster mode, the offset point mode, and then in the large raster mode. The change to large raster is seen to increase the nutation amplitude as the instruments are indexed to begin large raster.

In Figure 5-15, the spacecraft was in the sun-centered point mode and it is seen that the residual peak-to-peak variation in wheel plane angle is about 0.08°. This shows that the misalignment between the azimuth bearing axis and the principal inertia axis of the wheel is about 3 arc-minutes. This corresponds to a dynamic unbalance of about 500 oz-in^2 which is consistent with the ground dynamic balance measurements. The residual wheel plane variation, from orbits randomly selected throughout the year, indicates that no perceptible change in the ADA bearing axis orientation has occurred.

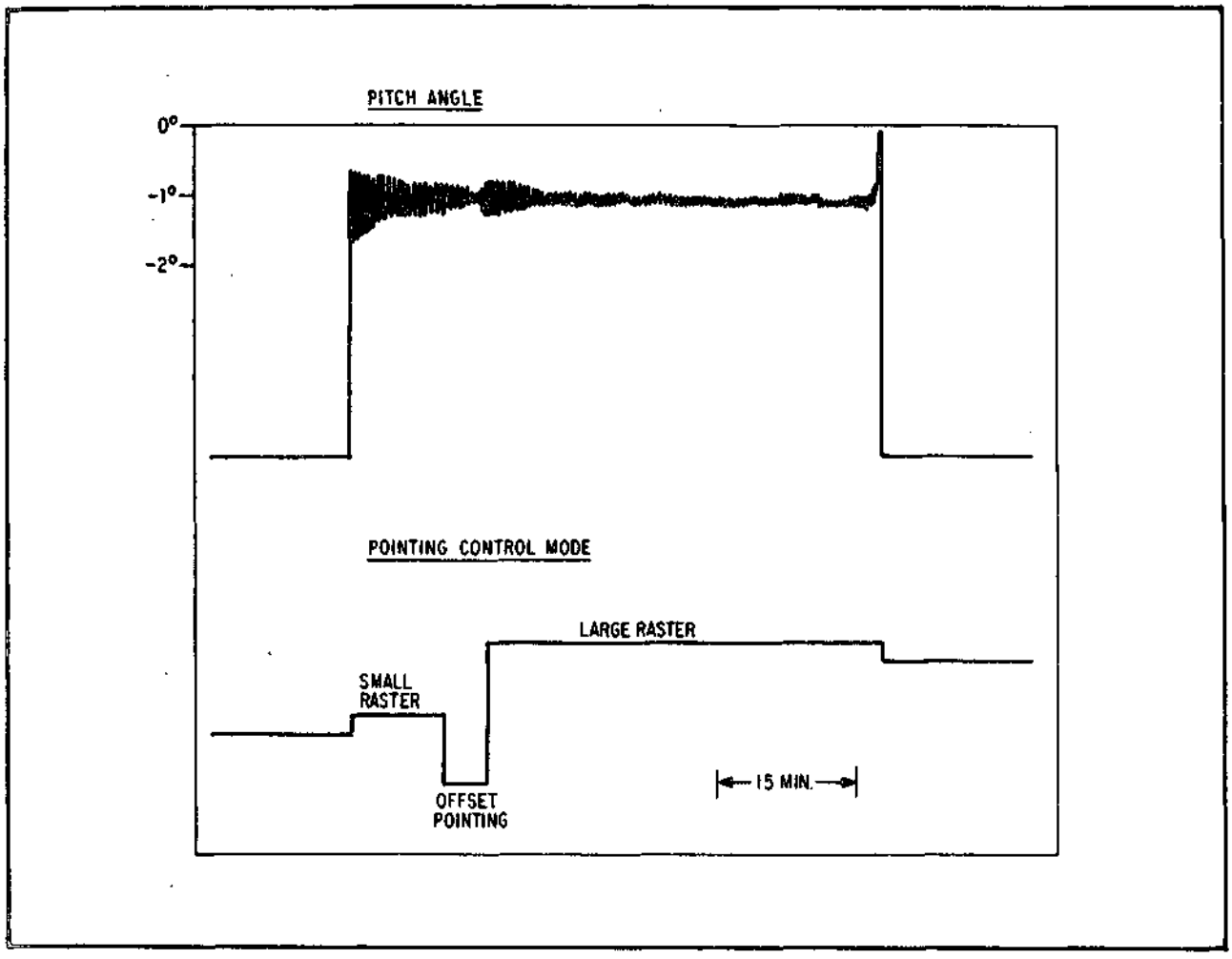

Figure 5-14 Spin Axis Motion During Pointing Mode Changes (Orbit Revolution 846)

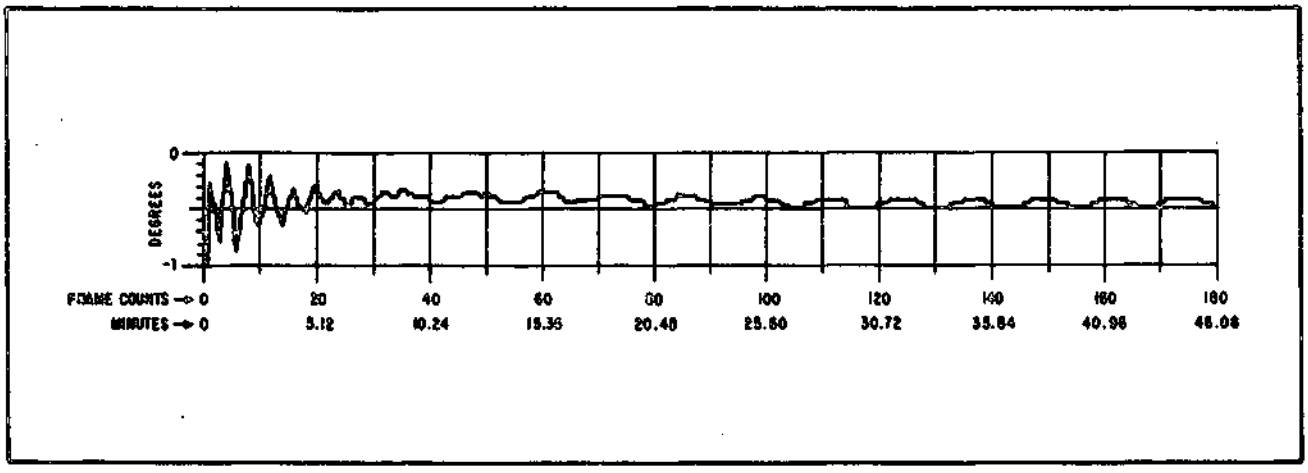

Figure 5-15 Spin Axis Motion During Sun-Centered Point Mode (Orbit Revolution 76)

A review of about 40 typical orbits shows that the dawn nutation transient decays to its residual value in about 5 minutes at low in-orbit spin rates (0.46 rps) which is as anticipated. However, it appears that the settling time at the highest in-orbit spin rates (0.58 rps) is sometimes greater than 10 minutes, which while satisfactory is somewhat longer than anticipated. The associated nutation decay time constant of 3 to 5 minutes may be due to a fluid viscosity deviation, but to pinpoint the cause a more detailed review throughout a broader range of spin rates than is presently available would be necessary. The nutation damper temperature and spin rates approaching the upper limit of the auto-spin range (0.68 rps) would be required for such a study.

5.5 SOLAR POINTING CONTROL SUBSYSTEM PERFORMANCE

Figure 5-16 shows telemetry records of the azimuth and elevation fine point sensors. The telemetry system resolution is about 1 1/2 arc-seconds. The jitter amplitude is less than 1 1/2 arc-seconds peak-to-peak for both the azimuth and elevation systems.

The pointing control stability in the sun-centered mode is about 3 arc-seconds peak-to-peak, including medium-term drift over 90 percent of the orbit day. For a few minutes at the beginning and end of an orbit day, there is a shift of about 6 arc-seconds as scattered light from the earth enters the control eyes.

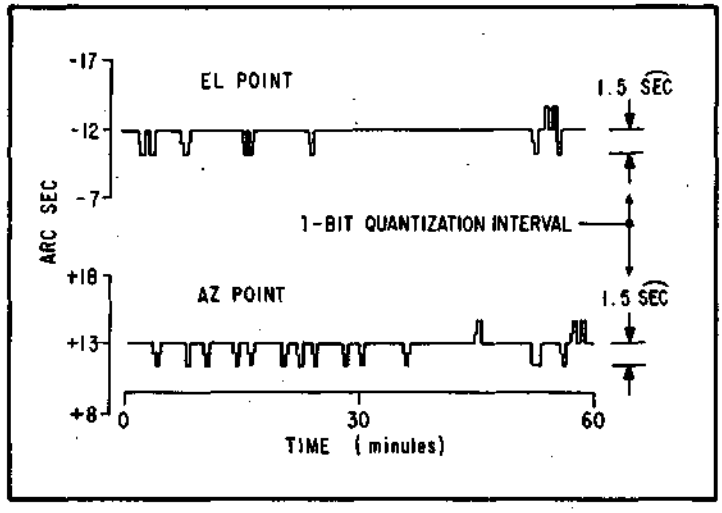

Figure 5-16 Pointing Control Performance Read-Out Sensor Output - Orbit Revolution 75

The albedo of the earth (sun reflection off the clouds, water, etc.) will enter the fine solar sensors when the earth is in the sensor field of view. This will bias the sensor and make the spacecraft point toward the earth a small amount from where it was commanded to point.

Although a shift was known to be present, the amount of shift is small and thus was not detected by experimenters on previous spacecraft. Since both control and readout sensors are biased the same, it is not detected by the position readout sensors.

The shift was first detected in the data from the GSFC instrument on OSO-7. A shift of about 18 arc-seconds was noticed in the position of features in the small raster referenced to the borders of the raster. Also, rasters taken of the limb of the sun showed shifts in the limb position. The shift occurs about 6 minutes after dawn and 6 minutes before dusk when the earth limb is about 22 degrees from the center of the sun. It appears to be a step function or at least occurs in less than 1 minute.

At the time this report was written, several points of concern remained about this shift. The magnitude of the shift should be about 9 arc-seconds which is in reasonable agreement with that observed. However, the sensors have a field-of-view of only 12 degrees. At dawn there is no albedo and, therefore, no shift and when the 12 degree field stop is coincident with the limb there should be no shift since the sensor no longer sees any of the earth. Between these angles, the shift should build up and decay in near triangular fashion as the area of earth seen by the sensor increases then decreases.

Also rasters have been found in which no shift appeared or only one of two features shifted. One notable example is orbit revolution 4039 which had two well defined features. At dawn neither of these features shifted and at dusk only one of them showed a shift.

Table 5-4 lists the misalignment of the readout eyes and the pointed instruments relative to the control system null points. The pointed instrument axes were determined by examination of in-orbit data generated by the instrument detectors, as the pointing control scanned features of the sun. Instrument alignment errors were essentially removed by the data reduction process which reconstructs the instrument raster in coordinates referenced to the limb of the sun.

Table 5-4
POINTING ALIGNMENT RASTER

	Control Eyes	Fine Readout Eyes	Raster Readout Eyes	NRL	GSFC
Azimuth	0	+(L)13 arc-sec	-(R)0.9 arc-min		+(R)0.5 arc-min
Elevation	0	-(D)12 arc-sec	-0.1 arc-min		+(U)0.1 arc-min

The spacecraft has been operated in the center point mode very little, and therefore, the offset indexing and raster data reduction has been done principally with respect to the optical axes of the pointed instruments.

5.6 GYRO PERFORMANCE

The gain and drift of the gyro are dependent on the temperature of the gyro. This temperature is automatically controlled by an internal heater with command-selectable threshold levels. The gain of the gyro may be adjusted by ground command to achieve the proper system gain for the overall azimuth control loop.

The initial on-orbit checkout of the gyro system was directed at determining the proper setting for the internal heater and the corresponding gain setting for the gyro to achieve drift-free and accurate control by the gyro. The gyro is also equipped with drift and offset compensation to permit the removal of steady-state bias errors or to buck out the drift components.

The heater set point was determined experimentally during orbit revolution 24 and again in orbit revolutions 135, 142 and 155. This was done by observing the temperature range of the gyro at different set points of the heater. From this data, a gyro temperature was selected for which the performance was predictable and satisfactory.

Initial in-orbit adjustments in the gyro drift and offset compensation were made by observing the readout of the scan readout eyes with the gyro operating during the day. Later, the gyro offset and drift was calculated by comparing the inertial position of the pointed instruments relative to the stars as measured by the azimuth shaft blipper and the star scanner.

Figure 5-17 shows early gyro drift data obtained over a 30 minute period during orbit revolution 225. The drift was about 0.23 degree per hour. Subsequently, command adjustment of the drift compensation reduced drift to less than 0.1 degree per hour.

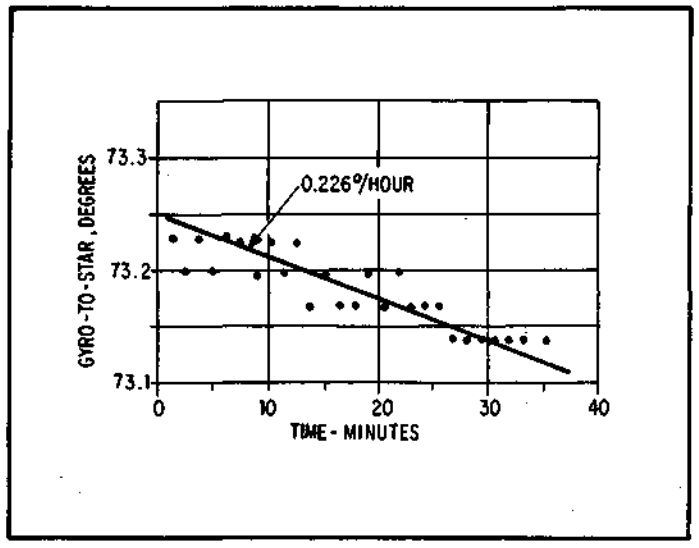

Figure 5-17 Typical Gyro Azimuth Drift (Orbit Revolution 225) Measured Relative to Stars Observed by Star Scanner

5.7 ATTITUDE DETERMINATION-STAR SCANNER PERFORMANCE

The star scanner permits determination of the spacecraft spin axis attitude and the instantaneous look angle of the rotating wheel experiments to within 0.1 degree in inertial space. This is made possible by statistically processing the star scanner intercept data and comparison with a catalog of known star locations.

The principal in-orbit adjustment of the star scanner involved the experimental determination of a gain setting for the star scanner which yielded a sufficient number of intercepts, but was low enough so that false triggering did not occur. Figure 5-18 shows the results of in-orbit operations compared with the predicted values for sensitivity to various star magnitudes.

During the early weeks of operation, various improvements were made in the data reduction program to increase the accuracy and accommodate the data generated by the star scanner in-orbit. Figure 5-19 shows the data processing statistics for a typical orbit. The same data was processed first by the data processing routine developed before launch and again by an improved routine.

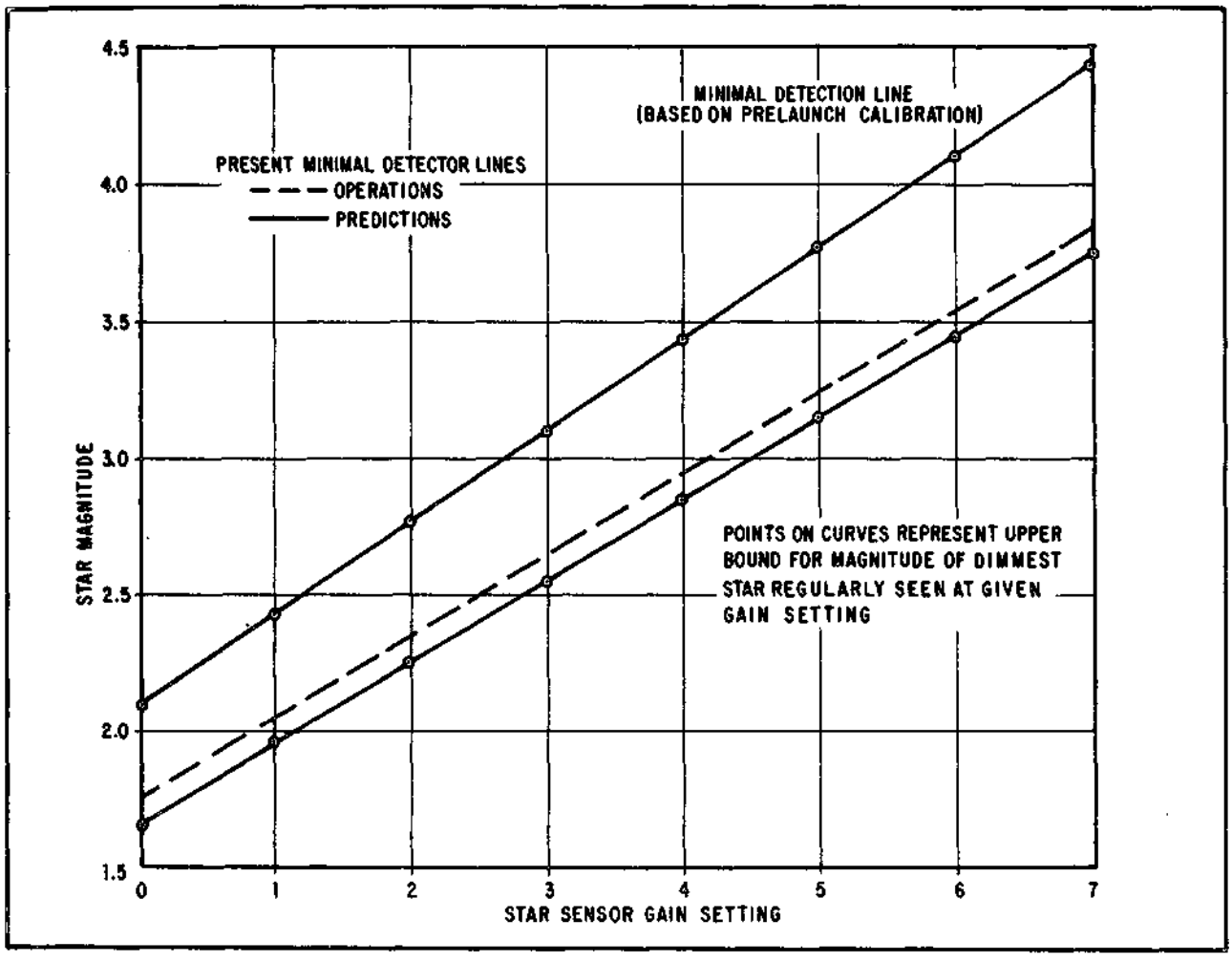

Figure 5-18 Star Scanner Sensitivity

The roll covariance plotted in the bottom chart of Figure 5-19 is indicative of the residual error in the attitude, calculated by matching the star sighting data with the star catalog. This residual error does not include random errors introduced by the hardware or other portions of the data reduction. These may add several hundredths of a degree. The overall accuracy of the attitude determination is better than 0.1 degree.

Other tests were conducted to determine whether the radiation levels present in the South Atlantic anomaly had any serious effect on the star scanner. While the South Atlantic anomaly evidently causes increased hardware errors while the spacecraft is in the region of high radiation, no apparent permanent damage is done and the recovery is quite rapid after leaving the anomaly.

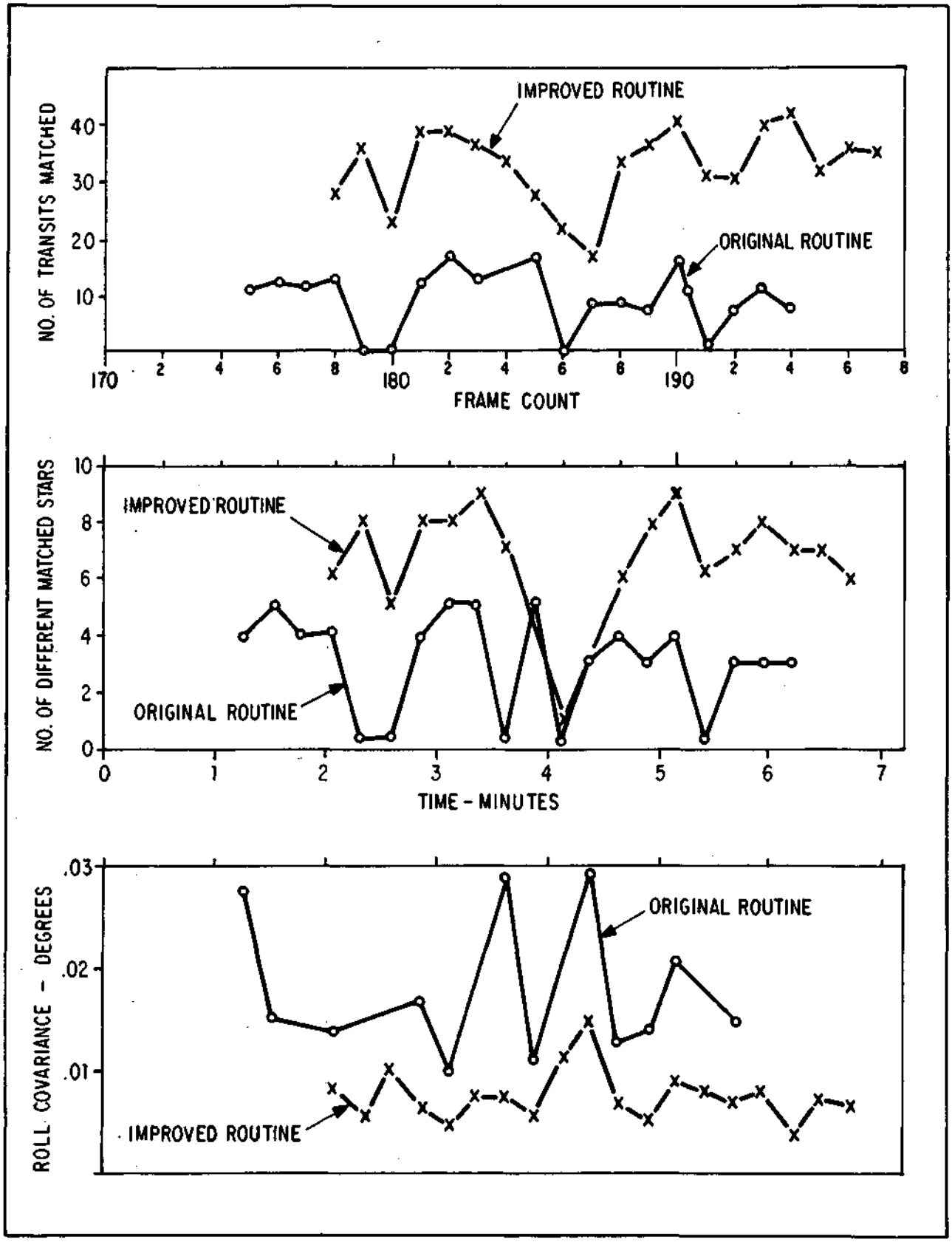

Figure 5-19 Star Sensor Performance During Orbit Revolution No. 271. Comparison of Results Using Original and Improved Data Reduction

The star scanner was also operated during the daylight portion of the orbit. Star crossings were observed and the software was able to calculate the vehicle attitude based on a limited number of sightings of brighter stars in the presence of sunlight. The star scanner was not intended to be used during the daylight portion of the orbit and its discrimination may not be adequate for *routine* operation under these conditions.

5.8 ELECTRICAL POWER SUBSYSTEM PERFORMANCE

During orbital operations, battery charge is controlled by adjusting the dummy loads in the spacecraft or turning off solar array panels by command so that the energy provided to the batteries is just sufficient to enable them to reach full charge at the end of orbit day.

Figure 5-20 shows load current, solar array current, and bus voltage for an early orbit (No. 32) where overcharge occurred and for a subsequent orbit (No. 33) where one panel was disconnected to prevent overcharge.

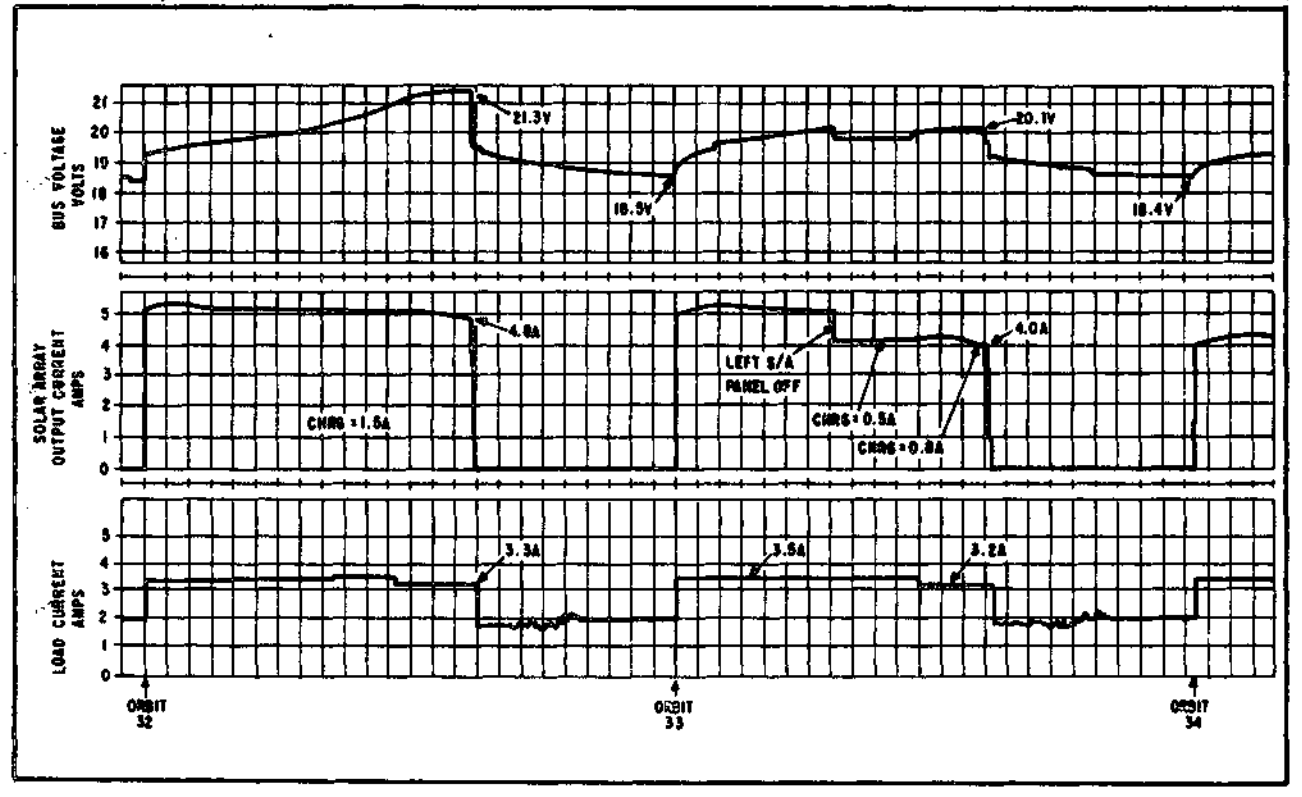

Figure 5-20 Load Current, Solar Array Current, and Bus Voltage for Early Orbit Revolution 32 Where Overcharge Occurred and for Subsequent Orbit Revolution 33 Where One Panel Was Disconnected to Prevent Overcharge

After a few days of orbital operation, methods were developed for trimming the dummy loads so that the bus voltage remained between 17.3 and 19.8 volts. Subsequent operation was satisfactory, as long as major changes in electrical loads were compensated for by adjusting the appropriate dummy loads.

During and after periods of overcharge, the cell balance monitor indicated some unbalance in the strings of battery cells. Usually this effect was not permanent and when the power system was returned to normal operation, the monitors again indicated a balanced condition.

Some unbalance still remained in battery string No. 4. Therefore, this battery string was removed from the system for several weeks, and only reconnected for periodic charging. Subsequently, its unbalance decreased and it was returned to service with no ill effects.

5.9 COMMUNICATION SUBSYSTEM PERFORMANCE

The communication subsystem has been evaluated completely in Sections 4.2 and 4.3.